

Crystallographic Symmetry Generates Phononic Holonomic Gates with Biased-Erasure Channels

El Mustapha Mansouri^{1,*} and Keigo Arai^{1,†}

¹*School of Engineering, Institute of Science Tokyo, Yokohama, Kanagawa, 226-8501, Japan*

(Dated: May 12, 2026)

Fault-tolerant solid-state processors require control layers whose errors are not merely small, but legible to quantum-error-correction decoders. We show that crystallographic symmetry can provide such a layer in strain-active solid-state Λ manifolds. When the projected strain tensor and Λ -transition operators share a multiplicity-one two-dimensional irreducible representation, symmetry fixes the linear strain interaction to a scalar dot product. Driving two phase-locked mechanical modes in quadrature then synthesizes a circular strain field, enabling complex phononic Λ -leg control without local microwave near fields. On this symmetry-generated manifold we construct a superadiabatic echo-lune holonomic gate using Λ -leg control and a resonant double-quantum counterdiabatic tone. Rotating-frame open-system simulations of a nitrogen-vacancy center give 99.88% conditional average fidelity in 1.833 μ s, or 99.40% when leaked population is counted as error; a separate resonant gigahertz high-overtone bulk acoustic resonator analysis translates the same Hamiltonian into Rabi-rate, linewidth, and envelope-tracking requirements. The same bright-state structure organizes the residual noise: A_2 -sector perturbations are parity-filtered into an optically distinguishable auxiliary state, whereas transverse E -sector faults are echo suppressed and retained as an explicit decoder stress axis. The extracted channel has 0.47% erasure probability and 0.168% residual Z error, with transverse error at the extraction floor. In XZZX code-capacity simulations, this biased-erasure model yields a nominal 64% fit-extrapolated reduction in data-qubit count relative to an unstructured Rabi baseline, while repeated-round detector-model diagnostics preserve the nominal distance-9 proxy and identify missed erasures, finite transverse floors, leakage/flag timing, and strong crosstalk as circuit-level validation limits. Extensions to orbital Λ systems, single-shot non-Abelian control, and bright-projector phonon-bus diagnostics identify crystallographic symmetry as a hardware-level principle for co-designing phononic actuation, leakage, noise bias, and quantum decoding.

I. INTRODUCTION

Fault-tolerant quantum processors require more than high-fidelity physical gates. They require control mechanisms whose locality, native error channels, and leakage signatures are compatible with decoding. In most solid-state platforms, these layers are engineered separately: the Hamiltonian is designed at the device level, while erasure structure and error bias are imposed later through encoding, measurement, and decoder choice. Here we show that, in a broad class of strain-active crystalline Λ manifolds, crystallographic symmetry can unify these layers.

The concrete motivation is the microwave delivery problem in dense solid-state registers [5, 6]. State-of-the-art dynamical gates on individually addressed qubits have achieved extraordinary fidelities, including 99.999% for nitrogen-vacancy (NV^-) centers in diamond [1], 99.99%+ for trapped ions [2], and sub- 10^{-4} single-qubit gate error in superconducting circuits [4], alongside continuing superconducting-qubit architecture development [3]; yet local microwave delivery in dense layouts introduces cryogenic heat-load and fan-out constraints in control stacks [8–10], as well as spectral-

crowding and crosstalk concerns for dense spin control [11] and microwave-field delivery/characterization in NV platforms [12]. A phononic control layer replaces local near-field microwave delivery by strain coupling at the qubit site. GHz electronics may still drive the piezoelectric transducer, but the strain field itself is local, frequency-selective, and confined by the acoustic wavelength.

Mechanical control is already an experimental resource: Barfuss *et al.* [13] demonstrated coherent mechanical driving of a single NV spin, MacQuarrie *et al.* [14, 15] and Chen *et al.* [16–18] engineered acoustic control of spin and orbital transitions, Lee *et al.* [19] showed multimode longitudinal strain tuning, and Cornell *et al.* [20] achieved mechanical coherence protection of silicon-vacancy (SiV^-) centers with Rabi frequencies reaching 800 MHz. The missing ingredient for geometric quantum information processing is complex Λ control: a single acoustic mode produces linearly polarized strain and cannot by itself select one arm of a three-level Λ manifold.

We show that this obstacle is removed whenever the defect's point group possesses a two-dimensional irreducible representation Γ_E : group theory *mandates* a dot-product coupling $H = g(\varepsilon_1 \mathcal{O}_1 + \varepsilon_2 \mathcal{O}_2)$, so that quadrature driving of two degenerate modes produces a circularly rotating strain field mathematically identical to a circularly polarized electromagnetic drive (Theorem 1). This *synthetic*

* mansouri.e.2224@m.isct.ac.jp

† arai.k.835f@m.isct.ac.jp

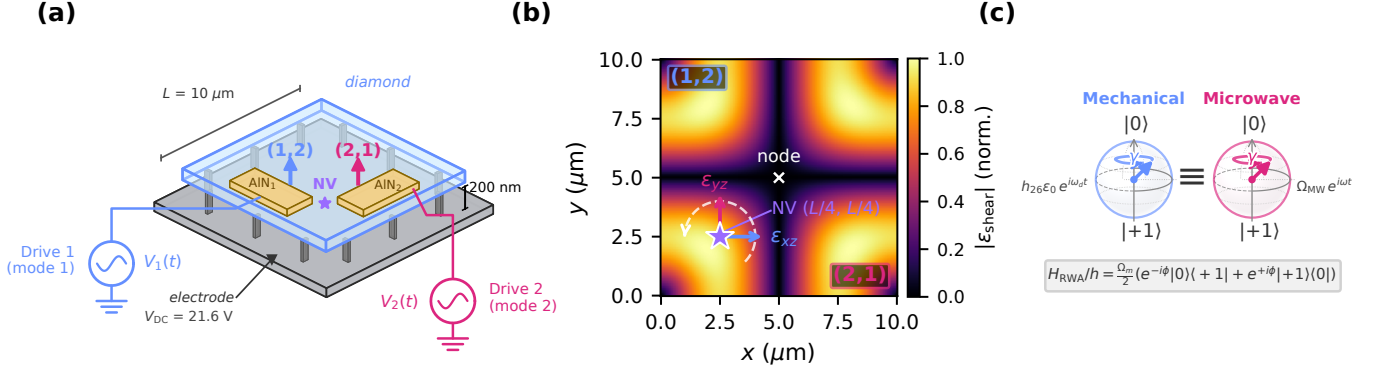


FIG. 1. Synthetic rotation isomorphism and hardware blueprint. (a) Three-dimensional schematic: a simply-supported diamond membrane ($10 \times 10 \times 0.2 \mu\text{m}$) suspended above a full-area electrode with a 200 nm vacuum gap. Two AlN piezoelectric transducers independently excite the degenerate (1,2) and (2,1) flexural modes. (b) Top-down strain topology showing orthogonal shear components ε_{xz} and ε_{yz} combining in quadrature at the NV site ($L/4, L/4$) to produce a circularly rotating strain field. (c) Bloch-sphere comparison: the mechanical rotating strain field drives the NV $|0\rangle \leftrightarrow |1\rangle$ transition identically to a circularly polarized microwave field. The single-quantum transition shown here illustrates the fundamental strain–spin coupling mechanism; the holonomic compilers of Sec. III operate in the $\{|-1\rangle, |1\rangle\}$ computational subspace via Λ -system traversal through $|0\rangle$. The shear strain amplitude plotted in panel (b) corresponds to ε_0 defined in Eq. (1). This figure illustrates one quadrature-mode topology; the resonant gigahertz high-overtone bulk acoustic resonator (GHz-HBAR) implementation is treated separately in Regime B and Appendix H. Regime A is the rotating-frame $\Lambda + \text{DQ-SATD}$ channel benchmark; Regime B is the resonant GHz-HBAR implementation route.

rotation mechanism is a shared-irrep criterion on the effective device symmetry: it applies to any strain-active solid-state Λ manifold whose projected strain pair and transition operators share a common two-dimensional irrep. Defect centers provide the experimentally mature examples, including C_{3v} defects (NV^- , divacancy in SiC) via spin-strain and D_{3d} defects (SiV^- , GeV^- , SnV^-) via orbit-strain; representative platforms are summarized in Sec. II A.

The microwave analogy is deliberately limited. At the rotating-frame Hamiltonian level the strain drive reproduces a circular microwave drive, but its chirality is not imposed by electromagnetic polarization. It is selected by a symmetry-protected strain/operator scalar of the crystal group. The same representation structure that fixes the control Hamiltonian also classifies perturbations into irreducible sectors, linking Hamiltonian design to the effective error channel rather than merely replacing one actuator by another. We test that link explicitly: a sector-injection diagnostic shows that the Λ bright manifold routes A_2 perturbations toward the detectable auxiliary level $|0\rangle$, whereas E -sector perturbations remain in the logical bright direction and are removed to leading order by the echo topology.

The protection statement is local and representation-theoretic: point-group symmetry protects the allowed strain-defect tensor against G_{eff} -preserving perturbations, but the mechanical mode degeneracy, quadrature balance, bath spectral weights, and erasure-detection efficiency remain device-level assumptions. This distinction

lets us separate what is symmetry-protected from what is benchmarked numerically.

The symmetry theorem supplies the essential control resource: a protected complex Λ -system drive generated mechanically from a Γ_E strain doublet. Once this Λ manifold is available, there are two complementary holonomic compilers. The first is the superadiabatic transitionless driving (SATD) echo-lune compiler used below for the Regime-A NV channel benchmark and the quantum error correction (QEC)-channel extraction. The second is a single-shot bright-state compiler in which the two Λ -leg amplitudes and scalar detuning remain proportional to one common envelope, $u(t) = (\Omega_0, \Omega_1, \Delta)^T = \Omega(t)u_0$. The SATD compiler is therefore the channel-engineering route, while the single-shot compiler is the compact universal-control route.

A matched-environment 3C-SiC C_{3v} comparison is reported in Sec. VII B and Appendix N, Sec. 7, as a platform-design check, not as a separate measured-device benchmark.

One NV membrane mode topology that can instantiate the rotating-frame channel benchmark is summarized in Fig. 1. The erasure and decoder analysis below use the extracted $\Lambda + \text{DQ-SATD}$ channel, not the membrane strain model by itself. The resulting symmetry-to-decoder logic and validation hierarchy are summarized in Fig. 2 and Table I.

For the SATD compiler, we trace the fidelity ceiling of the adiabatic Orange Slice holonomic protocol to a geometric singularity at the Bloch-sphere South Pole and

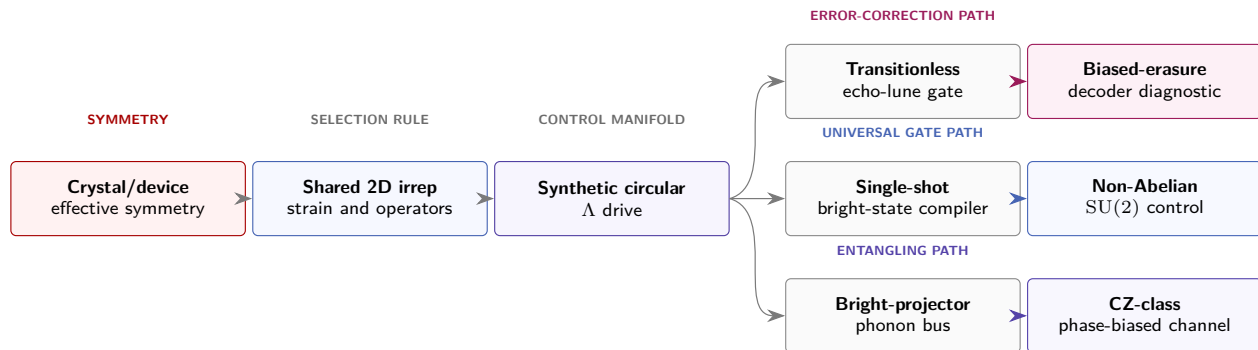


FIG. 2. Symmetry-to-decoder logic of the proposal. A multiplicity-one shared two-dimensional irrep fixes the linear strain interaction to a scalar dot product. Quadrature mechanical driving then realizes a protected complex Λ manifold. On that manifold, the superadiabatic transitionless driving (SATD) echo-lune compiler engineers the biased-erasure channel used for the quantum error correction (QEC) analysis, while the single-shot bright-state compiler supplies compact non-Abelian $SU(2)$ control. The sector-injection diagnostic in Sec. VIF and Appendix G verifies the intermediate sector-to-channel map on the SATD/QEC path. A Regime-F effective bright-projector bus extension, discussed in Sec. VIIC and Appendix Q, tests the corresponding CZ-class entangling-channel diagnostic but is not part of the single-qubit compiler stack.

TABLE I. Validation hierarchy. Each row names the model layer and its role in the paper; numerical performance is reported in the corresponding Results sections.

Regime	Platform / model	Control resources	What this establishes
A	NV rotating-frame channel	Λ legs + DQ-SATD	Biased-erasure channel and sector map
B	NV GHz-HBAR projection	Same protocol at resonant Ω_m	Resonant route and envelope tracking
C	SiV orbital Λ benchmark	D_{3d} orbit-strain Λ legs	Synthetic-rotation transfer
D	Generic/NV single-shot compiler	Λ legs + scalar detuning	Compact non-Abelian $SU(2)$ control
E	SiV single-shot compiler	SiV Λ legs + scalar detuning	Fast orbital universal-control route
F	Bright-projector phonon bus	Bright projectors + phonon loop	CZ-class phase-biased diagnostic

eliminate it with a composite nonadiabatic geometric quantum computation (NGQC) two-loop topology combined with superadiabatic transitionless driving (SATD, $\lambda \equiv 1.0$) [25, 26]. This echo-lune protocol removes the adiabatic speed limit and shapes the residual channel into the biased-erasure form used for the QEC analysis. For the single-shot compiler, the same complex Λ legs are held in a fixed bright-state direction while a common envelope closes one cyclic excursion; this gives a simpler universal gate layer, but its residual channel is not merged with the SATD QEC channel.

We validate the framework through a controlled hierarchy of models. Regime A establishes the symmetry-generated rotating-frame NV channel and decoder-facing biased-erasure noise model; Regime B separately maps the resonant GHz-HBAR implementation route, where Rabi rate, linewidth, and envelope tracking become resonator-design parameters. Regime A is a rotating-frame NV channel benchmark. The membrane mode topology of Fig. 1 supplies an illustrative quadrature strain source, while the benchmark itself tests the complete Λ + DQ-SATD Hamiltonian at $\Omega_m = 2.22$ MHz and supplies the biased-erasure channel used for the decoder analysis. This benchmark reaches conditional $F_{\text{avg}} = 99.88\%$ at $T_{\text{gate}} = 1.833$ μs , with $F_{\text{avg}}^{\text{eff}} = 99.40\%$ after leakage is counted as error. Regime B evaluates

the corresponding resonant GHz-HBAR implementation route at the experimentally projected $\Omega_m = 2.83, 28.3,$ and 141.5 kHz scale. Regime C is a conservative SiV Λ -leg benchmark that tests D_{3d} synthetic-rotation control without an additional lower-doublet SATD channel, giving $F_{\text{avg}} = 96.32\%$ at $T_{\text{gate}} = 46.2$ ns. Regime D is the single-shot universal suite on the same symmetry-generated Λ manifold, using a $T_{\text{gate}} = 0.9009$ μs bright-state pulse with the two Λ legs plus scalar detuning and reaching $F_{\text{eff}} \simeq 99.86\%$ across representative noncommuting single-qubit gates. Regime E applies the same single-shot bright-state compiler directly to the SiV orbital Λ manifold using only the two orbit-strain Λ legs and a synchronized scalar detuning. No lower-doublet SATD matrix element is assumed. At the primary millikelvin point, $\Omega_{\text{peak}} = 300$ MHz gives $T_{\text{gate}} = 6.667$ ns and $F_{\text{eff}} = 99.52\% - 99.67\%$ across the representative four-gate suite. The dominant residual error is orbital- T_1 depolarization during auxiliary occupation, not erasure-convertible leakage. Regime F is an effective Λ -level architecture diagnostic: the same logical bright projectors couple to a detuned phonon loop to test whether a CZ-class two-qubit channel can remain phase-biased and heralded-leakage compatible. Regime F is evaluated at the effective projector-force level and supplies the entangling-channel diagnostic.

The same Γ_E -enabled Λ structure also organizes the leading noise operators into A_1 , A_2 , and E sectors. For weak noise with comparable irrep-sector bath weights, A_1 perturbations are common-mode, A_2 perturbations preferentially leak toward the optically distinguishable auxiliary state, and E -sector bit-flip errors are echo-suppressed. In the Regime-A rotating-frame NV channel this gives a strongly biased extracted model with $p_{\text{era}} = 0.47\%$ and $p_Z = 0.168\%$, while the transverse component lies at the numerical floor of the channel extraction. In a code-capacity model of this extracted Regime-A channel, XZZX and Calderbank-Shor-Steane (CSS) codes lie on opposite sides of the finite-size scaling boundary, yielding a substantial nominal overhead reduction. We treat this number as a logical-channel diagnostic rather than a complete architecture threshold, and promote finite p_{XY} floors and reduced erasure-detection efficiency to explicit decoder stress axes (Appendix O).

This hierarchy also defines the scope of the simulations. Regime A is the rotating-frame NV $\Lambda + \text{DQ-SATD}$ channel extraction, with the membrane mode topology serving as one strain-source realization; Regime B separately evaluates the resonant GHz-HBAR implementation route and its transfer-function constraints. Regime C tests the D_{3d} Λ -control mechanism using only the Λ legs established by the orbit-strain selection rule. Regime D establishes compact universal non-Abelian control on the same symmetry-generated Λ manifold. Regime E establishes the corresponding SiV-compatible single-shot universal-control route, again using only Λ legs plus scalar detuning. Regime F closes the architecture only at the effective projector-force level, as an entangling-channel diagnostic. The primary QEC simulations isolate the code-capacity consequence of the Regime A channel and then sweep finite transverse-error floors as a decoder validation envelope. We additionally run a lightweight scheduled two-sector XZZX detector-model stress diagnostic with repeated syndrome rounds, erasure-aware weights, measurement/reset faults, explicit transverse X/Y faults, leakage persistence, delayed flags, and local crosstalk. This diagnostic preserves the nominal $d = 9$ biased-erasure proxy under the extracted channel assumptions and identifies strong local crosstalk as the dominant architecture-specific validation target. A hardware-calibrated detector-error model remains the next step toward a device-level threshold.

The paper is organised as follows. Section II derives the synthetic rotation selection rule and the platform-independent Λ Hamiltonian. Section III presents the holonomic compilers: the adiabatic baseline and its South Pole limitation, the composite NGQC + SATD channel-engineering route, the single-shot bright-state universal-control route, and the gate-time compression mechanism. Sections IV and V provide full platform-specific models for NV⁻ and SiV⁻, respectively. Section VI reports the simulation results, error budget, biased-erasure noise analysis, decoder estimates, and scheduled stress diagnostic. Section VII discusses the

cross-platform scaling law, universal and entangling extensions, and experimental outlook.

II. SYMMETRY-TO- Λ THEORY

A. Selection rule for strain-mediated Λ -system control

We begin with the central theoretical result: a shared-irrep selection rule that identifies when an effective solid-state manifold supports complex Λ -leg control via mechanical strain.

Theorem 1 (Shared-irrep synthetic circular-strain interface). *Let \mathcal{H}_Λ be a projected low-energy solid-state Λ manifold with effective device symmetry G_{eff} and a real two-dimensional irreducible representation Γ_E . For an ideal point defect, G_{eff} reduces to the defect point group; in a device it is the little group left by crystal symmetry, confinement, static fields, and the acoustic mode basis. For D_{3d} centers, replace E, A_1, A_2 below by E_g, A_{1g}, A_{2g} . Suppose:*

1. *The projected symmetric strain tensor contains a pair $\epsilon = (\epsilon_1, \epsilon_2)$ transforming as Γ_E .*
2. *The transition-operator space of the encoded manifold contains a pair $\mathbf{O} = (O_1, O_2)$, spin or orbital, transforming under the same Γ_E .*
3. *The mechanical resonator supplies two degenerate phase-locked modes whose local strain projections are ϵ_1 and ϵ_2 at the defect site.*
4. *The selected shared-irrep channel is multiplicity-one in the projected linear strain coupling.*

Then:

1. *The only G_{eff} -invariant linear strain-defect coupling in this channel is*

$$H_{\text{int}} = g(\epsilon_1 O_1 + \epsilon_2 O_2).$$

2. *The non-scalar bilinears transform as*

$$B_{A_2} = \epsilon_1 O_2 - \epsilon_2 O_1,$$

and

$$\mathbf{B}_E = (\epsilon_1 O_1 - \epsilon_2 O_2, \epsilon_1 O_2 + \epsilon_2 O_1).$$

Thus they cannot appear in the Hamiltonian unless accompanied by symmetry-breaking spurions transforming as A_2 or E .

3. *A G_{eff} -preserving perturbation can only renormalize the scalar coefficient $g \rightarrow g + \delta g$ or generate A_1 detuning shifts. It cannot generate ellipticity, handedness mixing, or anisotropic strain coupling at first order. In this precise sense, the circular strain selection rule is symmetry-protected.*

4. For quadrature driving,

$$\epsilon_1(t) = \epsilon_0 \cos \omega_d t, \quad \epsilon_2(t) = \epsilon_0 \sin \omega_d t,$$

and circular operators $O_{\pm} = O_1 \pm iO_2$, the interaction becomes

$$H_{\text{int}}(t) = \frac{g\epsilon_0}{2} (O_+ e^{-i\omega_d t} + O_- e^{+i\omega_d t}).$$

Under the rotating-wave approximation, tuning ω_d to one arm of the Λ system retains a single circular component, yielding the single-arm rotating Hamiltonian used below.

Proof sketch. Write the most general linear coupling in the selected doublet channel as $H_{\epsilon} = \epsilon^T C \mathbf{O}$. Invariance under $g \in G_{\text{eff}}$ requires $R_E(g)^T C R_E(g) = C$. Because the shared irrep is irreducible and appears once in the selected channel, Schur's lemma gives $C = g_0 I_2$, yielding the dot product. For the defect point groups used below, the familiar decompositions $\Gamma_E \otimes \Gamma_E = A_1 \oplus A_2 \oplus E$ for C_{3v} and $E_g \otimes E_g = A_{1g} \oplus A_{2g} \oplus E_g$ for D_{3d} give the listed non-scalar bilinears explicitly. They can enter only when multiplied by symmetry-breaking spurions in the corresponding irreps. Substitution of the quadrature drive gives the circular decomposition above, and the RWA selects one component on resonance. A complete projector derivation and spurion classification are given in Appendix G. The representation-theory notation and selection-rule logic follow standard condensed-matter group-theory conventions [21]. \square

Remark 1 (Effective symmetry beyond point defects). Theorem 1 is not a statement about defect chemistry. For a non-defect solid-state subsystem, such as an acceptor, valley-orbital manifold, hole-spin manifold, or gate-defined quantum dot, the relevant group is the effective little group

$$G_{\text{eff}} = G_{\text{crystal}} \cap G_{\text{confinement}} \cap G_{\text{device}} \cap G_{\text{field}}.$$

The criterion is the same: the projected strain tensor and the transition-operator space of the encoded Λ manifold must share a multiplicity-one two-dimensional irrep. Thus the mechanism generalizes to strain-active crystalline Λ manifolds satisfying this shared-irrep criterion. The present work focuses on defect centers because they provide natural high-symmetry realizations and experimentally established strain couplings.

The theorem protects the local strain-defect tensor, not the mechanical device by itself. The resonator must either supply a symmetry-degenerate doublet or be tuned and phase-locked so that residual splitting and quadrature imbalance are perturbative on the gate timescale. Point groups with only one-dimensional irreps, such as C_{2v} , C_{2h} , or C_2 , cannot support this synthetic circular mechanism because no strain pair transforms as a single two-dimensional irrep.

The NV-center platform is reviewed in Refs. [6, 7], while group-IV split-vacancy centers in diamond are reviewed in Ref. [32]; the microscopic group-IV electronic

structure is treated in Ref. [33]. Table II summarizes the verified platforms.

Among C_{3v} platforms, the neutral divacancy in 3C-SiC shares the NV spin-strain tensor structure identically [29, 30], differing only in coupling magnitudes and zero-field splitting; Density-functional theory (DFT) calculations yield $|h_{16}/h_{26}| \approx 0.75$ for 3C-SiC (compared with 6.95 for NV⁻), so the parasitic AC Stark channel that arises in NV (Sec. IV D) is intrinsically weaker in this host. This ratio reappears below as a C_{3v} platform-selection parameter: at fixed Ω_m , the parasitic DQ Stark scale is proportional to $|h_{16}/h_{26}|^2/D$. Among D_{3d} platforms, SiV⁻ (spin-orbit splitting $\Delta_{\text{SO}} = 48$ GHz) is within reach of demonstrated acoustic resonator frequencies [20], while GeV⁻ (170 GHz [31]) and SnV⁻ (850 GHz [34]) require nanophotonic or optomechanical transduction.

B. Synthetic rotation via degenerate mechanical modes

The selection rule guarantees the *form* of the coupling; here we show how a concrete resonator geometry realizes it. Consider a mechanical resonator supporting two degenerate modes whose strain fields project onto orthogonal components ϵ_1 and ϵ_2 at the defect site. Driving these modes in quadrature with equal amplitude produces a circularly rotating strain field:

$$\epsilon_1(t) = \epsilon_0 \cos(\omega_d t), \quad \epsilon_2(t) = \epsilon_0 \sin(\omega_d t), \quad (1)$$

where ϵ_0 is the peak strain amplitude and $\omega_d = 2\pi f_0$ the mechanical drive angular frequency, tuned to the Λ -system splitting. Substituting into the dot-product coupling of Theorem 1 and applying the rotating-wave approximation yields an effective σ_+ -type Hamiltonian

$$\frac{H_{\text{RWA}}}{\hbar} = \frac{\Omega_m}{2} (e^{-i\phi} |0\rangle\langle +1| + e^{+i\phi} |+1\rangle\langle 0|), \quad (2)$$

mathematically identical to a circularly polarized microwave drive, where $\Omega_m = g\epsilon_0$ is the mechanical Rabi frequency. The physical origin of Ω_m differs by platform (spin-strain coupling h_{26} for C_{3v} ; orbit-strain coupling f_{\perp} for D_{3d}), but the rotating-frame Hamiltonian is universal.

TABLE II. Solid-state platforms satisfying the synthetic rotation selection rule (Theorem 1). All entries have a verified $A_1(A_{1g})$ -type dot-product coupling.

Platform	Group	Λ type	Coupling	Splitting
NV ⁻ (diamond)	C_{3v}	Spin	2.8 GHz/str.	2.87 GHz
VV ⁰ (3C-SiC)	C_{3v}	Spin	1.8 GHz/str.	1.33 GHz
SiV ⁻ (diamond)	D_{3d}	Orbital	1.3 PHz/str.	48 GHz
GeV ⁻ (diamond)	D_{3d}	Orbital	~ 1 PHz/str.	170 GHz
SnV ⁻ (diamond)	D_{3d}	Orbital	~ 1 PHz/str.	850 GHz

C. Effective Λ -system Hamiltonian

The holonomic gate protocols of Sec. III require two independently controlled circular drives of opposite chirality: σ_+ near D_+ and σ_- near D_- (where $D_{\pm} \equiv D \pm \gamma_e B_z$ are the Zeeman-split transition frequencies), to simultaneously address both legs of the Λ manifold. The identical spatial mode topology provides the required orthogonal coupling for each chirality with independent amplitude and phase control. The complete control Hamiltonian decomposes as

$$\frac{H_{\Lambda}(t)}{h} = \frac{\Omega_m}{2} \left[\sin \frac{\theta}{2} (|0\rangle\langle -1| + \text{h.c.}) - \cos \frac{\theta}{2} (e^{-i\phi} |0\rangle\langle +1| + \text{h.c.}) \right], \quad (3)$$

where $\theta(t)$ and $\phi(t)$ are the time-dependent mixing angle and azimuthal phase. The zero eigenstate of H_{Λ} is the dark state

$$|D\rangle = \cos \frac{\theta}{2} |-1\rangle + e^{i\phi} \sin \frac{\theta}{2} |+1\rangle,$$

while the coupled bright state is

$$|B\rangle = \sin \frac{\theta}{2} |-1\rangle - e^{i\phi} \cos \frac{\theta}{2} |+1\rangle.$$

With this convention the Hamiltonian reduces to

$$H_{\Lambda}/h = \frac{\Omega_m}{2} (|0\rangle\langle B| + |B\rangle\langle 0|),$$

so that $|D\rangle$ is exactly dark and $|B\rangle$ couples to $|0\rangle$ with strength $\Omega_m/2$. Cyclic traversal of $|D\rangle$ on the Bloch sphere generates the geometric holonomy.

The subsequent gate protocols (Sec. III) operate entirely on this Hamiltonian, parameterised solely by Ω_m , $\theta(t)$, and $\phi(t)$. The physical realization of Ω_m differs by platform (Secs. IV and V), but the gate construction is platform-independent.

III. HOLONOMIC COMPILERS ON THE SYMMETRY-GENERATED Λ MANIFOLD

The symmetry-to- Λ reduction supplies the common control manifold. The remaining choice is the compiler: how the available complex Λ legs, and when needed a scalar detuning or auxiliary counterdiabatic actuator, are turned into a logical gate. We use two compilers with different purposes. The SATD echo-lune compiler is the error-channel engineering route used for the Regime-A NV channel benchmark and the QEC extraction. The single-shot bright-state compiler is the compact universal-control route on the same manifold. This holonomic-control language builds on non-Abelian geometric phases and holonomic quantum computation [22, 23], with the nonadiabatic Λ -system formulation closely related to Ref. [24].

A. Adiabatic baseline and the South Pole singularity

The adiabatic Orange Slice protocol is the useful foil: it sweeps the dark state $|D(\theta, \phi)\rangle$ of Eq. (3) around a two-leg loop, but the path crosses the South-Pole coordinate singularity where the azimuthal phase jumps. In our benchmark this leaves a 99.07% noiseless ceiling even after first-order derivative-removal-by-adiabatic-gate (DRAG)-type correction, showing that the bottleneck is geometric rather than a simple drive-amplitude limit.

The relevant counter-diabatic operator basis is

$$H_{\text{CD}} = -\lambda \frac{\dot{\theta}}{2} [\sin \phi \text{Op}_{\text{re}} + \cos \phi \text{Op}_{\text{im}}], \quad (4)$$

Here λ is the counter-diabatic correction strength, and $\text{Op}_{\text{re}} = |-1\rangle\langle +1| + |+1\rangle\langle -1|$ and $\text{Op}_{\text{im}} = i(|+1\rangle\langle -1| - |-1\rangle\langle +1|)$ are lower-manifold Pauli-like operators. This term suppresses first-order non-adiabatic leakage from the dark state. At $\lambda = 1.0$, it improves the bare Orange-Slice fidelity from 98.67% to 99.07%, but it does not remove the longitudinal phase artifact generated at the pole [35]. This motivates changing the trajectory topology before applying the exact SATD correction.

B. Composite NGQC + SATD protocol

The Zhu–Wang two-loop construction [25] provides the required topological change. The trajectory consists of two symmetric sub-loops (Fig. 3), each tracing a thin orange-slice lune on the parameter sphere, where $T \equiv T_{\text{gate}}$ denotes the total gate time.

Loop 1 ($0 \leq t \leq T/2$, starting azimuth $\phi_1 = 0$):

$$\theta(t) = \theta_{\text{max}} \sin\left(\frac{\pi t}{T/2}\right), \quad (5)$$

evolving from the North Pole through the South Pole ($\theta_{\text{max}} = \pi$) and back. The azimuth shifts by $\delta\phi = \pi/4$ via a narrow tanh step centered at the South Pole ($\theta = \pi$, $\sin \theta = 0$), closing the lune with finite enclosed area.

Loop 2 ($T/2 \leq t \leq T$, starting azimuth $\phi_2 = \pi$): An identical lune displaced to the complementary azimuth, with ϕ sweeping from π to $\pi + \delta\phi$ at the South Pole.

Each lune encloses a solid angle $\Omega_0 = \delta\phi(1 - \cos \theta_{\text{max}}) = \pi/2$. The dark-state Berry phase per lune is $\gamma_D = -\Omega_0/2 = -\pi/4$, while the bright state acquires $\gamma_B = +\Omega_0/2 = +\pi/4$ (their Berry curvatures carry opposite signs). Over the full two-loop path, the dark state accumulates $\gamma_D^{\text{tot}} = -\pi/2$ and the bright state $\gamma_B^{\text{tot}} = +\pi/2$; the relative geometric phase $\gamma_{\text{geo}} = \gamma_D^{\text{tot}} - \gamma_B^{\text{tot}} = -\pi$ implements the target $Z(\pi)$ rotation.

This topology provides three simultaneous advantages:

- Singularity neutralization.** Although each sub-loop traverses the South Pole ($\theta = \pi$), the azimuthal transition is confined to this point where

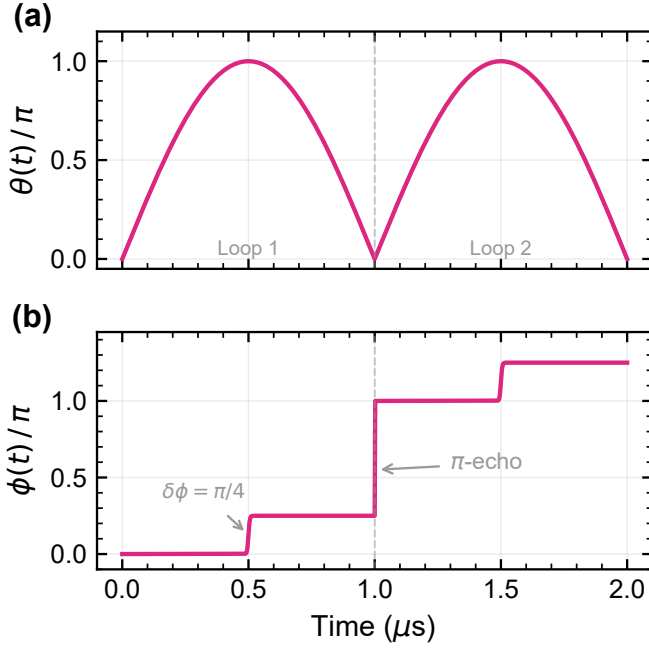


FIG. 3. Composite NGQC trajectory. (a) Mixing angle $\theta(t)$ executes two symmetric sub-loops, each traversing the full $\theta_{\max} = \pi$ (North Pole \rightarrow South Pole \rightarrow North Pole). (b) Azimuthal phase $\phi(t)$: within each sub-loop ϕ shifts by $\delta\phi = \pi/4$ at the South Pole, and the starting azimuth advances by π between loops. All ϕ transitions occur where $\sin\theta = 0$, neutralising the coordinate singularity.

$\sin\theta = 0$. Consequently the $\dot{\phi}$ -induced non-adiabatic coupling $\langle B|\partial_t|D\rangle \propto \dot{\phi}\sin\theta$ vanishes identically at the pole, and the $\dot{\theta}$ -only SATD counter-diabatic Hamiltonian remains exact.

2. **Phase echo.** The π separation between loop starting azimuths causes deterministic dynamical phases to cancel by destructive interference: $+\gamma_d$ in loop 1 and $-\gamma_d$ in loop 2. The same echo symmetry cancels the first- and second-order Berry-connection corrections generated by quasi-static E -sector perturbations. The leading surviving geometric correction from this sector is therefore $O(\sigma_E^3/\Omega_m^3)$, while the A_2 sector is suppressed by the parity filter discussed in Sec. VIF and proved in Appendix G.

3. **Gate-time compression.** When combined with counter-diabatic driving, the adiabatic speed limit is removed, enabling aggressive temporal compression.

C. Superadiabatic transitionless driving (SATD)

Executing two sub-loops within $T_{\text{gate}} \leq 2\mu\text{s}$ demands extreme angular velocities, far exceeding the adiabatic limit. Without counter-diabatic correction, the bare composite protocol yields $F = 22.92\%$, confirming that

the compressed path is not usable without the counter-diabatic generator.

The SATD framework [26–28] constructs an exact counter-diabatic Hamiltonian (Appendix D):

$$H_{\text{CD}} = -\frac{\dot{\theta}}{2} [\sin\phi \text{Op}_{\text{re}} + \cos\phi \text{Op}_{\text{im}}], \quad (6)$$

with operators Op_{re} and Op_{im} as defined in Eq. (4). Equation (6) has the same operator structure as the DRAG Hamiltonian (Eq. (4)), but with the critical distinction that the correction strength $\lambda \equiv 1.0$ is now derived *analytically* from Berry’s theorem [26] rather than determined empirically, requiring no tuning. This exactly cancels all non-adiabatic transitions, enforcing strict parallel transport of the instantaneous eigenstates and completely removing the adiabatic speed limit. For NV^- the operator in Eq. (6) is physically synthesized by a resonant double-quantum strain tone at $2\gamma_e B_z$, with amplitude and phase proportional to $|\dot{\theta}|$ and $\phi + \pi/2$, respectively (Appendix E). In the DQ rotating frame this tone supplies $H_{\text{DQ}}^{\text{res}}/\hbar = [\Omega_{\text{re}}\text{Op}_{\text{re}} + \Omega_{\text{im}}\text{Op}_{\text{im}}]/2$, and the SATD Hamiltonian is obtained by choosing $\Omega_{\text{re}} = -\dot{\theta}\sin\phi$ and $\Omega_{\text{im}} = -\dot{\theta}\cos\phi$.

With SATD active, the noiseless fidelity of the composite protocol reaches $F = 99.76\%$, breaking the 99.07% Orange Slice ceiling. The residual 0.24% error is dominated by higher-order coherent imperfections in the composite loop geometry.

D. Single-shot bright-state compiler and non-Abelian SU(2) gates

The same symmetry-generated Λ manifold also supports a nonadiabatic bright-state compiler that does not use adiabatic following, the SATD counterdiabatic actuator, or direct logical-state coupling. In a rotating frame and using cycle-frequency units $K = H/\hbar$, write

$$K(t) = \Delta(t) |a\rangle \langle a| + \frac{1}{2} [\Omega_0(t) |a\rangle \langle 0_L| + \Omega_1(t) |a\rangle \langle 1_L| + \text{h.c.}]. \quad (7)$$

The single-shot condition is proportional control:

$$\Omega_0(t) = \Omega(t) \cos\alpha \cos\frac{\vartheta}{2}, \quad (8)$$

$$\Omega_1(t) = \Omega(t) \cos\alpha e^{-i\phi} \sin\frac{\vartheta}{2}, \quad (9)$$

$$\Delta(t) = \Omega(t) \sin\alpha. \quad (10)$$

In the Regime-D validation, $\Delta(t)$ is treated as a synchronized rotating-frame detuning command; Stark or DC detuning can be substituted only after calibration as the third waveform channel. Equivalently,

$$u(t) = (\Omega_0, \Omega_1, \Delta)^T = \Omega(t)u_0. \quad (11)$$

TABLE III. Two compilers on the same symmetry-generated Λ manifold. The SATD compiler is the channel-engineering route used for the Regime-A QEC analysis; the single-shot compiler is the compact universal-control route used for Regime D.

Compiler	Controls, role, and output
SATD echo-lune	Λ legs + resonant DQ SATD Error-channel shaping Regime-A biased-erasure channel
Single-shot bright-state	Λ legs + scalar detuning Universal SU(2) gates Regime-D non-Abelian gate suite

Defining

$$\begin{aligned} |b_{\mathbf{n}}\rangle &= \cos \frac{\vartheta}{2} |0_L\rangle + e^{i\phi} \sin \frac{\vartheta}{2} |1_L\rangle, \\ |d_{\mathbf{n}}\rangle &= \sin \frac{\vartheta}{2} |0_L\rangle - e^{i\phi} \cos \frac{\vartheta}{2} |1_L\rangle, \end{aligned}$$

with $\mathbf{n} = (\sin \vartheta \cos \phi, \sin \vartheta \sin \phi, \cos \vartheta)$, the Hamiltonian factorizes as

$$K(t) = \Omega(t)M_{\alpha, \mathbf{n}}, \quad (12)$$

where

$$M_{\alpha, \mathbf{n}} = \sin \alpha |a\rangle \langle a| + \frac{\cos \alpha}{2} (|a\rangle \langle b_{\mathbf{n}}| + |b_{\mathbf{n}}\rangle \langle a|). \quad (13)$$

Thus $[K(t), K(t')] = 0$ and the pulse shape enters only through its area. The cyclic area condition is

$$\int_0^T \Omega(t) dt = 1. \quad (14)$$

It returns the logical subspace to itself and induces

$$U_L(\mathbf{n}, \gamma) = |d_{\mathbf{n}}\rangle \langle d_{\mathbf{n}}| + e^{-i\gamma} |b_{\mathbf{n}}\rangle \langle b_{\mathbf{n}}|, \quad \gamma = \pi(1 + \sin \alpha). \quad (15)$$

Up to a global phase, this is $\exp[-i\gamma \mathbf{n} \cdot \boldsymbol{\sigma}/2]$. The family is non-Abelian because changing \mathbf{n} changes the bright-state projector:

$$[U(\mathbf{n}_1, \gamma_1), U(\mathbf{n}_2, \gamma_2)] \propto (\mathbf{n}_1 \times \mathbf{n}_2) \cdot \boldsymbol{\sigma}. \quad (16)$$

The operational diagnostic used in Regime D is the pair $X_{\pi/2}Z_{\pi/2}$ and $Z_{\pi/2}X_{\pi/2}$: each sequence matches its own target, while the two composed unitaries have average fidelity 0.5 relative to one another. The full proof, transfer-matrix condition $G(\omega)u_0 \simeq g(\omega)u_0$, detuning sensitivity, and protocol-stack comparison are collected in Appendix P.

E. Gate-time compression

Because SATD eliminates coherent leakage to a negligible $\sim 0.003\%$ residual, the error budget is overwhelmingly dominated by dissipative processes that scale linearly with gate time. Compressing T_{gate} from 5.0 μs to

the $\sim 1\mu\text{s}$ scale truncates the system's temporal exposure to all destructive channels (T_1 lattice relaxation, $T_{1\rho}$ rotating-frame depolarization, and quasi-static surface noise), providing the primary engineering lever for maximizing gate fidelity.

The NGQC construction eliminates dark-state dynamical phase by design; the bright-state dynamical phase $\gamma_B \approx \Omega_m T_{\text{gate}}$ persists and produces oscillations in the process-level fidelity F_{avg} . The fidelity peaks sharply at “magic” gate times where $\gamma_B = 2\pi n$ (n integer), and drops as low as 90% between them. The optimal operating point must be selected from these discrete magic-time peaks (Sec. VI A).

The gate-time compression mechanism predicts that performance is governed by the ratio T_1/T_{gate} rather than by absolute T_1 : any platform with sufficient strain coupling to compress T_{gate} well below T_1 should achieve near-unity fidelity. This scaling is illustrated by the NV channel benchmark and the conservative SiV benchmark within their respective modeled control assumptions.

IV. NV⁻ SPIN-QUBIT IMPLEMENTATION AND CHANNEL BENCHMARK

A. Ground-state Hamiltonian and computational encoding

The ground-state spin-1 triplet (3A_2) of the NV center in diamond is described by the static Hamiltonian

$$H_0/h = D S_z^2 + \gamma_e B_z S_z, \quad (17)$$

where all frequencies are ordinary (cycle) frequencies consistent with the H/h convention; $D \approx 2.87$ GHz is the zero-field splitting, S_z is the z -component of the spin-1 angular momentum operator, $\gamma_e \approx 2.80$ MHz G⁻¹ is the electron gyromagnetic ratio, and $B_z = 50$ G lifts the $|\pm 1\rangle$ degeneracy via the electronic Zeeman effect. The architecture encodes the computational qubit within the $\{|-1\rangle, | +1\rangle\}$ doublet, utilizing the $|0\rangle$ state as the necessary auxiliary level to facilitate Λ -system holonomic traversal.

B. C_{3v} spin-strain coupling

Six independent coupling parameters characterize the spin-strain interaction of the NV center, which operates under the constraints of C_{3v} point-group symmetry [36]. The single-quantum ($\Delta m_s = \pm 1$) interaction Hamiltonian, driving transitions between $|0\rangle$ and $|\pm 1\rangle$, is

$$\begin{aligned} \frac{H_{\varepsilon 1}}{h} &= \frac{1}{2} [h_{26} \varepsilon_{xz} - \frac{1}{2} h_{25} (\varepsilon_{xx} - \varepsilon_{yy})] \{S_x, S_z\} \\ &\quad + \frac{1}{2} [h_{26} \varepsilon_{yz} + h_{25} \varepsilon_{xy}] \{S_y, S_z\}, \quad (18) \end{aligned}$$

where the shear coupling h_{26} and in-plane normal coupling h_{25} are summarized with their DFT uncertainties in Table IV.

The same dynamic strain field simultaneously drives the double-quantum ($\Delta m_s = \pm 2$) interaction, directly coupling $|-1\rangle$ and $|+1\rangle$ via the transverse operators ($S_x^2 - S_y^2$) and $\{S_x, S_y\}$:

$$\frac{H_{\varepsilon 2}}{h} = h_{16} [(\varepsilon_{xx} - \varepsilon_{yy})(S_x^2 - S_y^2) + 2\varepsilon_{xy}\{S_x, S_y\}], \quad (19)$$

with $h_{16} = \Xi_{\perp} = 19\,660(90)$ MHz strain $^{-1}$, approximately seven times larger than the primary single-quantum coupling. This large double-quantum interaction produces a parasitic AC Stark shift (Sec. IV D).

C. Mechanical implementation and rotating-frame parametrization

A (100)-oriented single-crystal diamond membrane [37] ($L = 10\ \mu\text{m}$, $h_m = 200\ \text{nm}$) supports nearly degenerate (1,2) and (2,1) flexural modes at $f_0 = 78.8$ MHz. At an off-center NV site ($L/4, L/4$), the ideal thin-plate mode topology gives two orthogonal local strain-channel directions of equal symmetry weight, so that quadrature driving realizes the rotating strain field of Eq. (1). We use this membrane geometry as a hardware blueprint for the synthetic-rotation topology, while treating $\Omega_m = 2.22$ MHz as an effective rotating-frame Rabi-rate target for the Regime-A channel benchmark rather than as a calibrated three-dimensional membrane prediction. Reaching the NV resonance at $D \approx 2.87$ GHz requires a resonant GHz-HBAR implementation, treated separately in Regime B and Appendix H.

The same rotating-frame Hamiltonian applies once Ω_m , drive phases, and envelopes are specified; the achievable Ω_m , bandwidth, heating, phase noise, and multi-tone drive constraints are implementation-specific and are therefore reported separately (Appendix H). Consequently the biased-erasure channel is not claimed as a calibrated prediction of the flexural membrane strain model.

TABLE IV. C_{3v} spin-strain coupling tensor components and their roles in the full open-system model. All values from DFT calculations of Ref. [36].

Component	Magnitude (MHz/strain)	Transition
h_{26} ^a	-2830(70)	$\Delta m_s = \pm 1$
h_{25} ^b	-2600(80)	$\Delta m_s = \pm 1$
h_{16} (Ξ_{\perp}) ^c	19 660(90)	$\Delta m_s = \pm 2$
h_{43} ^d	2300	$\Delta m_s = 0$

^a Mechanical Rabi drive

^b Minor ellipticity ($\eta \lesssim 4.3\%$)

^c AC Stark shift ($S_z|_{\mathcal{Q}} = \sigma_z$): canceled by dynamic compensation; see Theorem 2

^d Longitudinal detuning

It is extracted from the full Regime-A open-system control package, while HBAR transfer-function residuals are treated as explicit transverse-floor stress axes in the decoder analysis.

Under the RWA, the opposite-chirality matrix element oscillates at $\sim 2D$ and is far off-resonant; a single circular drive addresses only one arm of the Λ system. The holonomic protocol requires two independent drives of opposite chirality (σ_+ near $D_+ \equiv D + \gamma_e B_z$ and σ_- near $D_- \equiv D - \gamma_e B_z \approx 2.73$ GHz), realizing the full $H_{\Lambda}(t)$ of Eq. (3).

D. AC Stark shift and dynamic compensation

The macroscopic strain $\varepsilon_0 \approx 7.84 \times 10^{-4}$ required for $\Omega_m = 2.22$ MHz acts simultaneously on the large h_{16} tensor, producing an effective double-quantum coupling

$$\Omega_{\text{DQ}} = \Xi_{\perp} \varepsilon_0 \approx 15.41 \text{ MHz}. \quad (20)$$

Although detuned by $D \approx 2.87$ GHz, this off-resonant drive generates a deterministic AC Stark shift via second-order perturbation theory [38]:

$$\begin{aligned} \delta_{\text{AC}} &= \frac{\Omega_{\text{DQ}}^2}{4D} = \frac{(15.41)^2}{4 \times 2870} \text{ MHz} \\ &\approx 20.72 \text{ kHz}. \end{aligned} \quad (21)$$

More generally, for a C_{3v} spin-1 platform at fixed target single-quantum rate,

$$\varepsilon_0 = \frac{\Omega_m}{|h_{26}|}, \quad \Omega_{\text{DQ}} = |h_{16}| \varepsilon_0 = \left| \frac{h_{16}}{h_{26}} \right| \Omega_m, \quad (22)$$

and therefore

$$\delta_{\text{AC}} = \frac{1}{4D} \left| \frac{h_{16}}{h_{26}} \right|^2 \Omega_m^2. \quad (23)$$

Thus the same C_{3v} symmetry class can have very different uncompensated Stark burden depending on the tensor ratio $|h_{16}/h_{26}|$; this motivates the matched 3C-SiC comparison in Sec. VIIB and Appendix N, Sec. 7.

The double-quantum operators connect only $|+1\rangle \leftrightarrow |-1\rangle$ and have identically zero matrix elements with $|0\rangle$. The shift acts exclusively within the computational manifold:

Theorem 2 (AC Stark structure and cancellation). *The effective DQ AC Stark Hamiltonian in the rotating frame is*

$$H_{\text{Stark}}(t) = -2\pi \delta_{\text{AC}} \left(\cos \theta(t) + \frac{\gamma_e B_z}{D} \right) S_z, \quad (24)$$

where $\theta(t)$ is the polar angle of the Bloch-sphere trajectory and $S_z|_{\{|+1\rangle, |-1\rangle\}} = \sigma_z$. For the sinusoidal NGQC

TABLE V. NV operating regimes used in the simulations.

Implementation / role	Topology or resonant route	Ω_m	Role in paper
Regime A channel package	Membrane topology illustration; rotating-frame Ω_m target	2.22 MHz	Rotating-frame channel extraction
Regime B GHz-HBAR	Resonant near 2.87 GHz NV transition	2.83–141.5 kHz	Resonant route + envelope tracking

trajectory $\theta(t) = \pi \sin(\pi t/\tau)$, the accumulated differential phase over the full gate is

$$\Phi_z = -2\pi \delta_{AC} \left[J_0(\pi) + \frac{\gamma_e B_z}{D} \right] T_{\text{gate}}, \quad (25)$$

where J_0 is the zeroth Bessel function ($J_0(\pi) \approx -0.304$). Because $\theta(t)$ is prescribed by the control protocol, a dynamic compensation field $H_{\text{comp}}(t) = -H_{\text{Stark}}(t)$ cancels this shift at every instant, removing all residual differential phase.

Proof. Part 1 (operator structure).—Each physical strain drive (at frequency $\omega_{\pm} = 2\pi(D \pm \gamma_e B_z)$) simultaneously excites the DQ channel with amplitude $g_{\pm} = (\Omega_{\text{DQ}}/2)\{\cos(\theta/2), \sin(\theta/2)\}$. In the doubly-rotating frame, these DQ couplings oscillate at detunings $\Omega_{\mp} = 2\pi(D \mp \gamma_e B_z)$, respectively. Standard dispersive perturbation theory [38–40] gives the energy shifts

$$\delta E_{\pm 1} = \mp \frac{g_{\pm}^2}{\hbar \Omega_{\mp}} \pm \frac{g_{\mp}^2}{\hbar \Omega_{\pm}}, \quad \delta E_0 = 0, \quad (26)$$

where $\delta E_0 = 0$ follows from the vanishing DQ matrix elements with $|0\rangle$. Since $\delta E_{+1} = -\delta E_{-1}$, the shift is purely antisymmetric, the signature of an S_z operator. Combining over a common denominator and using $\sin^2(\theta/2) - \cos^2(\theta/2) = -\cos\theta$ yields Eq. (24). The complete derivation is given in Appendix J.

Part 2 (trajectory averaging).—The accumulated differential phase is $\Phi_z = -2\pi \delta_{AC} \int_0^{T_{\text{gate}}} [\cos\theta(t') + \gamma_e B_z/D] dt'$. Each NGQC sub-loop uses $\theta(t) = \pi \sin(\pi t/\tau)$ with $\tau = T_{\text{gate}}/2$. Substituting $u = \pi t/\tau$ and applying the integral representation $J_0(z) = \pi^{-1} \int_0^{\pi} \cos(z \sin u) du$ gives $\int_0^{\tau} \cos\theta dt = \tau J_0(\pi)$. Both sub-loops have identical $\theta(t)$ profiles, so they add, yielding Eq. (25).

Part 3 (dynamic compensation).—Since $\theta(t)$ is prescribed by the control protocol, the instantaneous Stark coefficient $\cos\theta(t) + \gamma_e B_z/D$ is analytically known. Applying $H_{\text{comp}}(t) = +2\pi \delta_{AC} [\cos\theta(t) + \gamma_e B_z/D] S_z$ via a DC electrode cancels the shift at every instant. \square

Over a $T_{\text{gate}} = 5.0 \mu\text{s}$ gate, the uncompensated bare Stark scale $\delta_{AC} = 20.72 \text{ kHz}$ could accumulate up to ~ 0.65 rad of differential σ_z phase if $\cos\theta \equiv 1$. Trajectory averaging reduces the effective coupling by $|J_0(\pi)| \approx 0.30$, and partial cancellation between $J_0(\pi) < 0$ and $\gamma_e B_z/D > 0$ further lowers the net coefficient to $|J_0(\pi) +$

$\gamma_e B_z/D| \approx 0.26$, yielding an uncompensated residual of ~ 0.17 rad at $T_{\text{gate}} = 5.0 \mu\text{s}$ and ~ 0.06 rad at the optimal $T_{\text{gate}} = 1.833 \mu\text{s}$. Dynamic compensation eliminates this residual entirely.

a. Eigenstate protection. For computational basis inputs ($|\pm 1\rangle$), a static S_z phase is exactly unobservable: $|\langle \pm 1 | e^{-i\alpha \sigma_z} | \pm 1 \rangle|^2 = 1$ for all α . During driven evolution, however, $[S_z, H_{\text{drive}}(t)] \neq 0$, so the time-dependent AC Stark interaction does not reduce to a pure S_z rotation; fidelity therefore degrades at sufficiently large Stark scales.

Note that this S_z -type AC Stark structure is specific to $S = 1$ defects with $\Delta m_s = \pm 2$ selection rules and does not hold for D_{3d} orbital systems (Sec. V).

Device design constraints including boundary conditions, electrostatic degeneracy tuning, and the voltage budget are detailed in Appendix M.

E. Open-system noise model

The simulations assume a single NV center at depth $d_{\text{NV}} = 20 \text{ nm}$ (standard ion implantation [41]) with $T_1 = 1 \text{ ms}$ [42], $T_{1\rho} = 500 \mu\text{s}$ [43] (isotopically purified ^{12}C , $> 99.9\%$ [44, 46]), and $T_2^* \sim 10 \mu\text{s}$.

a. ME-CCE surface noise. Shallow NV centers at $d_{\text{NV}} = 20 \text{ nm}$ are dominantly decohered by in-sequence hopping of surface electron spins [47–49]. We employ the many-body expanded cluster correlation expansion (ME-CCE) framework (Appendix F), modeling $N = 20$ surface spins with density $\rho_s = 0.004 \text{ nm}^{-2}$ and spatial correlation length $r_c = 5 \text{ nm}$. Pairwise hopping rates follow $\Gamma_{ij} = (1/\tau_c) \exp(-r_{ij}/r_c)$ with $\tau_c = 10 \text{ ns}$ (worst-case fast noise [50]), propagated via a Gillespie kinetic Monte Carlo (KMC) algorithm [47]. The instantaneous noise field at the NV site is the dipolar sum

$$B_z^{\text{surf}}(t) = \frac{\mu_0 \mu_B}{4\pi} \sum_{i=1}^N s_i(t) \frac{3 \cos^2 \alpha_i - 1}{r_i^3}. \quad (27)$$

In the Hamiltonian this field enters as $H_{\text{surf}}/h \propto B_z^{\text{surf}}(t) S_z$. Thus the ME-CCE/KMC bath is not assumed to respect the NV point group as a full environment; it is an explicitly modeled A_2 -sector system-operator perturbation. The extracted leakage is therefore consistent with the A_2 parity-filter mechanism, while its absolute rate is obtained only from the Regime-A

open-system simulation. A sector-projection diagnostic confirms this assignment: Hilbert–Schmidt projection of the simulated surface-noise operator onto equal-norm representatives (S_z^2, S_z, S_x, S_y) gives weights $(0, 1, 0, 0)$, and propagation of 96 ME-CCE/KMC traces through the Regime-A SATD control with the surface term alone gives $L_{\text{surf}} = 0.456\%$ (Appendix G, Sec. 4). In the instantaneous bright manifold, the same diagnostic directs the first-order A_2 response entirely toward $|0\rangle$, whereas an equal-norm counterfactual E -sector injection points toward the logical bright state.

b. Variance normalization. The $N = 20$ discrete bath under-samples the macroscopic surface integral, requiring a finite-size correction. We employ a static per-lattice geometric scaling factor that preserves the critical inter-trajectory DC offsets responsible for inhomogeneous broadening (T_2^*), rather than per-trajectory normalisation which would destroy quasi-static noise structure.

c. Lindbladian dissipation. Three collapse operators are integrated into the master equation: (i) spin-lattice relaxation ($T_1 = 1$ ms) via $|\pm 1\rangle \rightarrow |0\rangle$ decay channels; (ii) rotating-frame depolarization ($T_{1\rho} = 500$ μs), contributing $\sim 0.06\%$ at the optimal gate time; and (iii) pure dephasing from the ME-CCE stochastic field.

F. Numerical implementation

The QuTiP 5.0.4 library [51, 52], leveraging the `mesolve` density-matrix propagator, executes the open-system simulations across a 384-core computing cluster. Each sweep point averages 500 independent Monte Carlo noise trajectories with 2000 time steps and solver tolerances $\text{atol} = 10^{-10}$, $\text{rtol} = 10^{-8}$. The core validation suite contains ten parametric sweeps, spanning 11–121 grid points each and yielding $\sim 100,000$ total trajectory-sweep configurations. The supplemental validation ledger also includes an additional Floquet/lab-frame multitone check, reported separately as Sweep 12, and the Regime-E SiV single-shot benchmark as a separate universal-control model calculation.

Gate fidelity is assessed at the process level using three complementary metrics. The *Uhlmann–Jozsa state fidelity* for a single input $\rho_0 = |-1\rangle\langle -1|$ serves as a legacy baseline:

$$F_{\text{state}} = \left(\text{Tr} \sqrt{\sqrt{\rho_{\text{id}}} \rho_{\text{act}} \sqrt{\rho_{\text{id}}}} \right)^2. \quad (28)$$

We propagate an informationally complete (IC) set of six input states $\{|\pm x\rangle, |\pm y\rangle, |\pm z\rangle\}$ through the same noise realization to reconstruct the 4×4 Choi matrix (the process-level representation of the quantum channel) Λ of the two-dimensional channel. The *entanglement (process) fidelity* is

$$F_e = \langle \Phi_U | \Lambda | \Phi_U \rangle, \quad |\Phi_U\rangle = (U_{\text{target}} \otimes I) |\Phi^+\rangle, \quad (29)$$

where $|\Phi^+\rangle = (|00\rangle + |11\rangle)/\sqrt{d}$ is the maximally entangled state, and the *average gate fidelity* follows from the Horodecki formula [53, 54]:

$$F_{\text{avg}} = \frac{d F_e + 1}{d + 1}, \quad d = 2. \quad (30)$$

a. Post-selection and leakage-aware metrics. Projecting each 3×3 qutrit output onto the computational subspace and renormalizing generates a 2×2 Choi matrix; the derived F_{avg} and F_e are *conditional* gate fidelities. The mean survival probability is $p_{\text{surv}} = 1 - \bar{\mathcal{L}}$ (where $\bar{\mathcal{L}}$ is the trajectory-averaged leakage), and the *effective (unconditional) average gate fidelity* is

$$F_{\text{avg}}^{\text{eff}} = p_{\text{surv}} F_{\text{avg}}^{\text{cond}}, \quad (31)$$

which treats all leaked population as completely erroneous. All ensemble statistics are quoted with 95% bootstrap confidence intervals (2000 resamples).

V. SiV⁻ ORBITAL Λ -CONTROL BENCHMARK

The group-IV vacancy centers in diamond (SiV⁻, GeV⁻, SnV⁻, and PbV⁻) possess D_{3d} point-group symmetry and an *orbital* E_g ground-state doublet split by spin-orbit coupling into two Kramers doublets separated by Δ_{SO} . Because the strain tensor decomposes as $\Gamma_\varepsilon = 2A_{1g} \oplus 2E_g$ and the inter-branch transition operators carry E_g symmetry [55], Theorem 1 applies directly: $E_g \otimes E_g \supset A_{1g}$ with multiplicity 1 guarantees the dot-product coupling $H = f_\perp (\varepsilon_1 L_1 + \varepsilon_2 L_2)$, where $L_{1,2}$ are orbital pseudo-spin operators within the E_g doublet.

A. D_{3d} orbital-strain coupling

The three-level Hilbert space comprises two computational states within the lower Kramers doublet (a time-reversal-protected degenerate pair) ($|+1\rangle \equiv |g_-\downarrow\rangle$, $|-1\rangle \equiv |g_-\uparrow\rangle$) and the auxiliary upper-branch state $|0\rangle \equiv |g_+\rangle$, with splitting $\Delta_{\text{SO}} = 48$ GHz [56]. The transverse orbit–strain coupling constant $f_\perp = 1.3$ PHz strain⁻¹ [55] is approximately 5×10^5 times larger than the NV spin–strain coupling $h_{26} \approx 3$ GHz/strain, reflecting the fundamental difference between direct electrostatic crystal-field modulation (orbital) and relativistic spin-orbit-mediated coupling (spin). This yields mechanical Rabi frequencies $\Omega_m = f_\perp \varepsilon_0$ reaching hundreds of MHz at experimentally demonstrated strain levels [20], enabling gate times in the low-nanosecond regime.

Two critical differences from NV emerge: (i) the AC Stark shift arising from the h_{16} -type double-quantum tensor is absent, since D_{3d} orbital systems lack the $\Delta m_s = \pm 2$ selection rules that generate the NV Stark structure (Sec. IV D), eliminating the need for DC compensation; and (ii) the dominant dissipation channel is reversed: orbital relaxation drives population from the

auxiliary state *into* the computational subspace (depolarization), rather than out of it (erasure).

B. Open-system parameters

The simulations use Lindbladian orbital T_1 decay with $T_1(\text{mK}) = 143 \text{ ns}$ (derived from the projected single-phonon-limited rate at $\Delta_{\text{SO}} = 48 \text{ GHz}$ via the T^5 phonon scaling law [57]) and $T_1(4 \text{ K}) = 40 \text{ ns}$ [57]. Stochastic surface noise is not included: the orbital Λ system is insensitive to the magnetic-noise channels that dominate NV decoherence, and the relevant orbital dephasing mechanisms require separate characterization. The reported fidelities are therefore T_1 -limited upper bounds. The scale $2/\Omega_m$ is the bright-state commensurability time used for the ideal lower-manifold/SATD resource estimate. In the conservative Regime C benchmark used below, the lower-manifold SATD Hamiltonian is removed; the reported T_{gate}^* values are selected by a direct gate-time sweep and are lengthened relative to $2/\Omega_m$ to recover adiabaticity.

For the SiV single-shot benchmark, we use the same orbital Λ manifold but switch from the echo-lune trajectory to the bright-state compiler of Sec. III D. The control resources are the two orbit-strain Λ legs and a synchronized scalar detuning; no lower-doublet SATD actuator is introduced. The orbital relaxation model sends auxiliary-state population equally into the two logical states. Orbital dephasing, charge noise, and actuator transfer-function errors are not included, so the reported fidelities should be interpreted as orbital- T_1 -limited control benchmarks.

a. Control transfer across platforms. The dot-product form, synthetic circular polarization via quadrature drive, and reduction to a single-arm Λ Hamiltonian transfer to all five platforms. The holonomic gate trajectory operates on the abstract H_Λ and is platform-independent. The SATD Hamiltonian requires a physical lower-doublet control: NV supplies it through the resonant DQ strain tone derived in Appendix E, while Regime C uses a conservative SiV Λ -leg-only benchmark and reserves SATD-enhanced SiV performance as a hardware-contingent upper bound. However, the noise environment differs qualitatively: whereas NV T_1 relaxation drives population from the computational subspace into the optically distinguishable $|0\rangle$ (erasure-convertible leakage), SiV orbital relaxation drives the auxiliary state *into* the computational subspace, producing depolarization (in-subspace Pauli errors) rather than erasure (detectable leakage out of the computational subspace).

VI. RESULTS

We label each parametric study as a numbered sweep (Sweeps 1–10) for cross-referencing with the simulation code and the SM.

A. NV gate-time optimization (Sweep 7)

Sweep 7 is the central result: process-level fidelity versus $T_{\text{gate}} = 1.0\text{--}5.0 \mu\text{s}$ [Fig. 6, Table VI]. All six informationally complete input states yield F_{avg} , F_e , leakage, and bootstrap confidence intervals at every grid point.

The legacy (single-state) fidelity F_{leg} , computed from the input $|{-1}\rangle$ alone (Eq. (28)), decreases monotonically:

$$\varepsilon_{\text{leg}}(T) \approx 0.003\% + 0.14\%/ \mu\text{s} \times T, \quad (32)$$

where the near-zero intercept confirms SATD eliminates coherent leakage. In contrast, F_{avg} oscillates with period $\Delta T \approx 0.83 \mu\text{s}$ ($1/\Delta T \approx \Omega_m/2$), peaking at “magic” times when the bright-state dynamical phase is commensurate with $2\pi n$ and dropping as low as 90% between them, a discrepancy of up to 9.5% that underscores why process tomography is essential.

At the optimal Regime A magic time $T_{\text{gate}} = 1.833 \mu\text{s}$:

$$\boxed{F_{\text{avg}} = 99.88\%, \quad F_e = 99.82\% \quad (T_{\text{gate}} = 1.833 \mu\text{s})}, \quad (33)$$

This operating point uses $\Omega_m = 2.22 \text{ MHz}$ and defines the rotating-frame NV channel benchmark; the GHz-HBAR projection is reported separately in Sweep 9. The 95% bootstrap confidence interval (CI) is $F_{\text{avg}} \in [99.882\%, 99.884\%]$, mean leakage $\bar{\mathcal{L}} = 0.484\%$, and

$$F_{\text{avg}}^{\text{eff}} = 0.995158 \times 0.998830 = 99.40\%. \quad (34)$$

The conditional $F_{\text{avg}} = 99.88\%$ corresponds to per-gate depolarizing error $r \approx 0.18\%$. The leakage is entirely detectable and convertible to a heralded erasure because $m_s = 0$ exhibits high photoluminescence (PL) contrast.

B. Control robustness and implementation projections (Sweeps 1–6, 9–10)

a. Geometric robustness (Sweep 2). Figure 4 compares the gate error of the holonomic protocol at full drive

TABLE VI. Gate-time compression results for the composite NGQC + SATD protocol (200 trajectories/point). F_{leg} is the single-state $|{-1}\rangle$ fidelity; F_{avg} and F_e are the process-level average gate and entanglement fidelities from 6-state IC tomography. Rows marked (\star) are “magic” gate times where the bright-state dynamical phase is commensurate with $2\pi n$.

$T_{\text{gate}} (\mu\text{s})$	$F_{\text{leg}} (\%)$	$F_{\text{avg}} (\%)$	$F_e (\%)$	Leak. (%)
1.000 \star	99.89	99.80	99.70	3.07
1.333	99.86	90.22	85.33	0.18
1.833 \star	99.81	99.88	99.82	0.48
2.000	99.79	98.10	97.15	7.21
2.667 \star	99.72	99.83	99.75	0.55
3.500 \star	99.63	99.63	99.45	3.24
4.500 \star	99.53	99.71	99.57	0.27
5.000	99.48	90.46	85.69	1.12

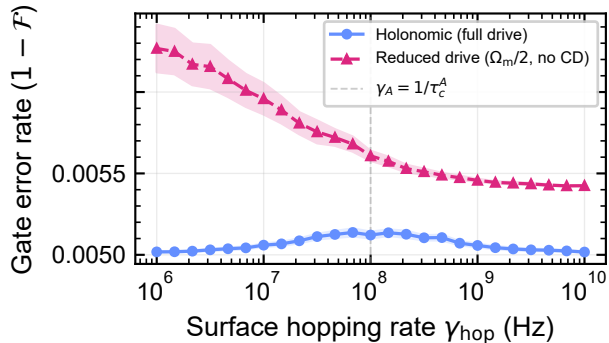


FIG. 4. Geometric robustness of the holonomic gate against surface noise (Sweep 2). Gate error rate ($1 - F_{\text{avg}}$) versus surface hopping rate γ_{hop} for the composite NGQC + SATD holonomic gate at full drive strength (blue circles) and a reduced-drive dynamical baseline ($\Omega_m/2$, no counter-diabatic correction; pink triangles). Shaded bands indicate 2σ bootstrap confidence intervals. The holonomic gate maintains a flat plateau ($\pm 0.006\%$ variation) across four decades of γ_{hop} , whereas the dynamical gate exhibits $7\times$ larger variation and converges only partially under motional narrowing. The dashed vertical line marks $\gamma_A = 1/\tau_c^A$, the crossover between quasi-static and motionally narrowed noise regimes.

against a reduced-drive dynamical baseline ($\Omega_m/2$, no counter-diabatic correction) across four decades of surface hopping rate $\gamma_{\text{hop}} = 10^6\text{--}10^{10}$ Hz. The holonomic gate error forms a noise-immune plateau at $\sim 0.50\%$ (variation $\pm 0.006\%$), consistently below the dynamical gate ($0.54\text{--}0.63\%$, variation $\pm 0.04\%$). The dynamical gate error decreases monotonically with increasing γ_{hop} as motional narrowing sets in beyond the crossover rate $\gamma_A = 1/\tau_c^A$ (dashed line), whereas the holonomic plateau is insensitive to this crossover. This dual advantage, a lower error floor *and* $7\times$ smaller variation, is intrinsic to the geometric phase mechanism: the holonomy depends on the enclosed solid angle, not on the instantaneous noise realization.

b. Counter-diabatic validation (Sweeps 5–6). Sweep 5 scans the DRAG parameter $\lambda = 0\text{--}2.0$ [Fig. 5]: fidelity peaks sharply at $\lambda = 1.0$ ($F_{\text{noisy}} = 99.49\%$), confirming exact cancellation of first-order non-adiabatic coupling. Sweep 6 validates the SATD correction strength $\alpha_{\text{CD}} = 0\text{--}2.0$ [Fig. 5(b)]: a razor-sharp symmetric peak at $\alpha_{\text{CD}} = 1.0$ ($F = 99.76\%$); at $\alpha_{\text{CD}} = 0$ and 2.0 , fidelity collapses to $\sim 26\%$. Achieving $F > 99\%$ requires $|\alpha_{\text{CD}} - 1.0| < 0.01$, confirming that the analytically exact counter-diabatic strength predicted by Berry’s theorem [26] is verified numerically.

c. Extended parametric studies. Additional sweeps confirm robustness against hardware and implementation variations (Appendix N): fidelity versus Rabi frequency Ω_m (Sweep 1, variation $\leq 0.09\%$), frequency detuning tolerance (Sweep 3, $< 0.04\%$ variation over 500 kHz), boundary-condition sensitivity (Sweep 4), GHz

HBAR extension (Sweep 9, $F_{\text{avg}} = 99.50\text{--}99.85\%$ at $T_{\text{gate}} = 2\mu\text{s}$ across the projected HBAR scenarios, assuming the same ideal rotating-frame control Hamiltonian while bounding HBAR-specific phase noise, heating, and transducer filtering separately), and quadrature drive imbalance (Sweep 10, $F_{\text{avg}} \geq 99.5\%$ on the central plateau, e.g. $|r - 1| \lesssim 4\%$ and $|\delta\varphi| \lesssim 4^\circ$; over the broader $6\%\text{--}6^\circ$ box the minimum sampled value is 99.32%). A Floquet multitone validation retaining leading counter-rotating terms from the two Λ tones and the DQ SATD tone gives only 2.4×10^{-5} additional infidelity in the ideal-bandwidth limit and 1.0×10^{-4} for a 200 MHz bandwidth with 0.2° phase noise and 0.2% amplitude imbalance (Appendix N). The same test shows that an unpredistorted $Q = 10^4$ GHz-HBAR transfer function is narrower than the $1.833\mu\text{s}$ Regime-A benchmark envelope. Regime B therefore converts the benchmark into a resonator-design target: predistortion, lower effective Q , or a slower HBAR-specific pulse sets the envelope-tracking strategy.

C. NV error budget

The error budget at the optimal Regime A operating point ($T_{\text{gate}} = 1.833\mu\text{s}$, composite NGQC + SATD) is presented in Table VII (full parameter listing in Appendix I, Table S4). All entries marked “Lindblad,” “ME-CCE,” “coherent,” “AC Stark,” and “South Pole” are *demonstrated in simulation*. Within the conditional process-level error ($\varepsilon = 0.12\%$), the largest contributor is Lindbladian $T_1/T_{1\rho}$ dissipation; however, the overall error budget is dominated by leakage ($\bar{\mathcal{L}} = 0.48\%$), which exceeds the in-subspace error by a factor of 4.

a. Leakage decomposition. SATD eliminates *coherent* leakage to 0.003% . Stochastic surface noise perturbs the instantaneous eigenstates, generating noise-mediated CD mismatch that drives population into $|0\rangle$. A separate sector-projection run using the actual $B_z^{\text{surf}}(t)S_z$ traces but omitting Lindblad relaxation gives $L_{\text{surf}} = 0.456\%$, confirming that the leakage channel is produced by the modeled A_2 surface perturbation rather than by an assumed point-group-symmetric bath. The full noisy Sweep 7 run gives $\bar{\mathcal{L}} = 0.484\%$ using 200 trajectories, whereas the surface-only sector diagnostic gives $L_{\text{surf}} = 0.456\%$ using 96 trajectories with Lindblad relaxation omitted. We therefore use the full-run leakage for the decoder-facing erasure rate and use the surface-only number only to identify the A_2 origin of the leakage channel.

b. Mechanism decomposition. The error reduction (from baseline 1.10% to 0.19% on the same single-input metric, about $6\times$, and 0.12% at the process level; Appendix N) is achieved through three mechanisms acting in concert: (1) singularity neutralization, (2) exact counter-diabatic driving ($\lambda \equiv 1.0$, coherent error $\sim 0.003\%$), and (3) gate-time compression (dissipative error $\sim 0.14\%/ \mu\text{s}$, minimized at the optimal magic time

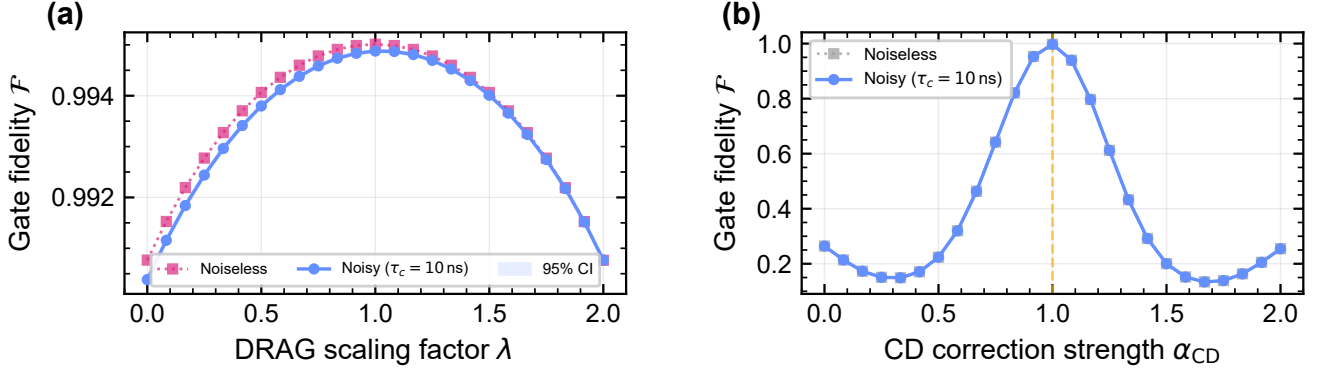


FIG. 5. Counter-diabatic validation. (a) Sweep 5: noiseless (solid) and noisy (dashed) fidelity versus counter-diabatic parameter λ ; the peak at $\lambda = 1.0$ confirms the 99.49% composite ceiling. (b) Sweep 6: SATD correction strength α_{CD} ; the razor-sharp symmetric peak at $\alpha_{CD} = 1.0$ validates exact counter-diabatic correction ($F = 99.76\%$).

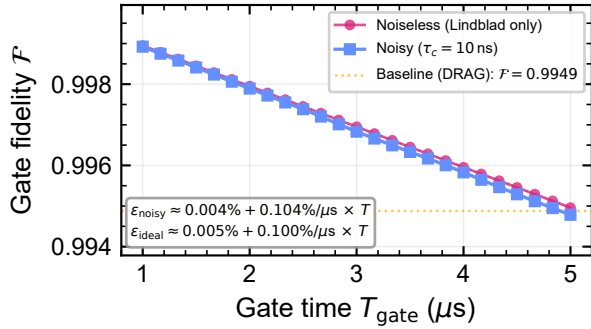


FIG. 6. Gate-time compression for Regime A (Sweep 7, $\Omega_m = 2.22$ MHz): legacy single-state fidelity (ideal: red circles; noisy: blue squares) versus T_{gate} , with the smooth linear envelope (Eq. (32)). Process-level F_{avg} (Table VI) oscillates due to bright-state dynamical phase, peaking at magic gate times; at the optimum $T_{\text{gate}} = 1.833 \mu\text{s}$, $F_{\text{avg}}^{\text{cond}} = 99.88\%$ ($F_{\text{avg}}^{\text{eff}} = 99.40\%$). GHz HBAR extension results are in Appendix N.

$T_{\text{gate}} = 1.833 \mu\text{s}$).

D. SiV orbital Λ -control result

We next apply the same synthetic-rotation Λ -leg control to a physically distinct system whose encoding (orbital vs. spin), symmetry (D_{3d} vs. C_{3v}), timescale (nanoseconds vs. microseconds), and dominant dissipation channel (depolarization vs. erasure) all differ from the NV case. Following the Regime C scope in Table I, the SiV benchmark sets $\alpha_{CD} = 0$ and uses only the physical Λ legs established by the orbit-strain selection rule. Table VIII summarizes the results. The best conservative point reaches $F_{\text{avg}} = 96.32\%$ on the SiV-

TABLE VII. Error budget at the optimal Regime A operating point ($T_{\text{gate}} = 1.833 \mu\text{s}$, composite NGQC + SATD, $d_{\text{NV}} = 20$ nm, $T_{1\rho} = 500 \mu\text{s}$). The upper rows decompose the conditional process-level error ($\epsilon = 0.12\%$); the lower rows show the impact of dissipative leakage on the unconditional (effective) fidelity.

Error source	Contribution
Lindblad $T_1/T_{1\rho}$ ^a	$\sim 0.12\%$
of which $T_{1\rho}$ ^b	$\sim 0.06\%$
of which T_1 ^c	$\sim 0.06\%$
ME-CCE surface noise ^d	$\sim 0.02\%$
Coherent (SATD residual) ^e	$\sim 0.003\%$
AC Stark shift ^f	$\lesssim 0.01\%$ (comp.)
South Pole singularity ^g	0.000%
<i>Unconditional (effective) fidelity</i>	
Legacy envelope^h	$\sim 0.19\%$
Process-level (F_{avg}, cond.)ⁱ	$\sim 0.12\%$
Leakage (\mathcal{L}) ^j	0.484%
Effective ($F_{\text{avg}}^{\text{eff}}$, uncond.)^k	$\sim 0.60\%$

^a Reduced by isotopic enrichment

^b $5\times$ lower than at $T_{1\rho} = 200 \mu\text{s}$

^c Sub-dominant

^d Reduced by deeper implant (20 vs. 10 nm)

^e Near-zero intercept

^f S_z on \mathcal{Q} ; NGQC-suppressed, DC-compensated

^g Neutralised ($\sin \theta = 0$ at pole)

^h $F_{\text{leg}} = 99.81\%$ at the optimal sampled point

ⁱ Magic-time refocusing; $F_{\text{avg}} = 99.88\%$

^j Full noisy Sweep 7 run; the separate surface-only sector diagnostic gives $L_{\text{surf}} = 0.456\%$

^k $F_{\text{avg}}^{\text{eff}} = 99.40\%$

orbital Λ system at millikelvin temperatures. The ideal lower-manifold SATD simulation gives $F_{\text{avg}} = 99.56\%$ at $T_{\text{gate}} = 6.5$ ns, but this number is treated as a control-resource upper bound pending a hardware-level SiV SATD channel.

The benchmark shows that synthetic-rotation Λ control remains quantitatively useful in the orbital platform.

TABLE VIII. Conservative SiV⁻ holonomic $Z(\pi)$ gate benchmark with the lower-manifold SATD Hamiltonian removed ($\alpha_{\text{CD}} = 0$). F_{avg} and F_e are computed from the Choi matrix over the computational subspace at the best millikelvin point found in the gate-time sweep.

Ω_m (MHz)	T_{gate}^* (ns)	F_{avg} (mK)	F_e (mK)	Leak. (mK)
100	99.2	91.18%	86.78%	7.96%
300	46.2	96.32%	94.48%	3.85%
500	123.3	90.14%	85.21%	8.64%

In this conservative regime, the gate time must be lengthened to recover adiabaticity, so orbital T_1 relaxation becomes the dominant limitation.

E. Single-shot universal control: generic and SiV implementations

1. Generic / NV-compatible single-shot suite (Regime D)

Regime D validates the second compiler rather than a second QEC channel. The simulation uses the same symmetry-generated complex Λ legs as Regime A, adds the scalar detuning required by Eq. (10), and applies a smooth \sin^2 common envelope with $\Omega_{\text{max}} = 2.220$ MHz and $T_{\text{gate}} = 0.9009$ μs . The nominal broadband surface-acoustic-wave in-phase/quadrature (SAW/IQ) implementation gives $F_{\text{eff}} \simeq 99.86\%$ across a representative universal gate set, where F_{eff} counts leakage as error (Table IX).

TABLE IX. Regime D single-shot universal-gate suite for the nominal 200 MHz SAW/IQ waveform channel. The compiler is not used in the XZZX overhead estimate.

Gate	F_{eff}	F_{cond}	Leakage
Z_π	99.8703%	99.9358%	0.0655%
X_π	99.8675%	99.9433%	0.0758%
$X_{\pi/2}$	99.8601%	99.9377%	0.0776%
Generic 0.73π	99.8657%	99.9405%	0.0749%

The non-Abelian diagnostic is performed independently at the unitary compiler level: $X_{\pi/2}Z_{\pi/2}$ and $Z_{\pi/2}X_{\pi/2}$ each match their intended target, but the two composed unitaries have average fidelity 0.5 relative to one another, as expected from Eq. (16). The residual single-shot channels are only moderately biased and gate-dependent, so they are not used for architecture-level fault-tolerance claims.

2. SiV orbital single-shot suite (Regime E)

We next apply the same bright-state compiler to the SiV orbital Λ manifold. This test is motivated by the

absence of an identified SiV lower-doublet SATD actuator: unlike the SATD echo-lune protocol, the single-shot compiler requires only proportional Λ -leg control and scalar detuning. The primary millikelvin benchmark uses $\Omega_{\text{peak}} = 300$ MHz, $T_{\text{gate}} = 2/\Omega_{\text{peak}} = 6.667$ ns, $T_{1,\text{orb}} = 142.7$ ns, and peak strain $\epsilon_{\text{peak}} = 2.308 \times 10^{-7}$. The resulting four-gate suite is summarized in Table X. The 100 MHz, 300 MHz, and 500 MHz millikelvin points, together with a 4 K temperature-stress test, are reported in Appendix P, Sec. 5.

The SiV single-shot result changes the SiV narrative. In Regime C, removing the lower-doublet SATD Hamiltonian forces a slower Λ -leg-only echo-lune trajectory and leaves the best millikelvin point at $F_{\text{avg}} = 96.32\%$. In Regime E, the bright-state compiler supplies a shortcut that remains expressible through the SiV-available Λ legs plus scalar detuning. The residual channel is qualitatively different from the NV biased-erasure channel: orbital relaxation returns auxiliary population to the logical manifold, so the dominant error is in-subspace depolarization rather than detectable leakage. Consequently, Regime E supports a high-fidelity SiV universal-control layer, but it is not a QEC-channel-engineering result.

F. Conditional symmetry selection of the biased-erasure channel

The Λ -system traversal through $|0\rangle$, which introduces leakage that a direct Rabi π -pulse avoids, becomes a structural advantage under quantum error correction: the leaked population is optically distinguishable and therefore convertible to a heralded erasure error, whereas the Rabi gate's in-subspace Pauli rotations are not. This erasure-conversion route is available to Λ -system gate topologies whenever leakage to the auxiliary state is efficiently distinguishable [60].

However, erasure conversion alone underestimates the code-capacity decoder advantage. The same Γ_E irrep that enables synthetic rotation (Theorem 1) also classifies the noise protection of the holonomic gate: the Λ Hamiltonian has bright eigenstates $|B_\pm\rangle = (|B\rangle \pm |0\rangle)/\sqrt{2}$ at energies $\pm\Omega_m/2$, and a quasi-static perturbation $V = \sigma \hat{V}$ couples the dark state to these bright states via two channels whose interference pattern depends on the irrep of \hat{V} .

The symmetry argument has two logically distinct parts. First, point-group symmetry fixes the allowed operator sectors of the strain-defect coupling and of weak system-operator perturbations. Second, the Λ -manifold dynamics maps those sectors into different geometric-error and leakage channels. Representation theory fixes the sector hierarchy, but not the scalar rates. In the Regime-A simulation, the ME-CCE/KMC surface bath enters specifically through $B_z^{\text{surf}}(t)S_z$, an A_2 -sector perturbation; the resulting erasure rate is therefore a numerical output of the open-system model, not a group-theoretic prediction. A direct sector-projection diagnos-

TABLE X. Regime E SiV single-shot bright-state universal-control suite. The benchmark uses only the two orbit-strain Λ legs and synchronized scalar detuning; no lower-doublet SATD actuator is assumed. The dominant error is orbital- T_1 depolarization during auxiliary occupation. The result is not used in the biased-erasure or XZZX-channel analysis.

Gate	T_{gate}	ϵ_{peak}	F_{eff}	F_{cond}	Leakage
Z_π	6.667 ns	2.308×10^{-7}	99.5221%	99.7488%	2.275×10^{-3}
X_π	6.667 ns	2.308×10^{-7}	99.5221%	99.7488%	2.275×10^{-3}
$X_{\pi/2}$	6.667 ns	2.308×10^{-7}	99.6699%	99.7979%	1.283×10^{-3}
Arbitrary axis 0.73π	6.667 ns	2.308×10^{-7}	99.5671%	99.7621%	1.957×10^{-3}

tic gives unit weight in the A_2 operator sector and zero numerical weight in the A_1 or E representatives (Appendix G, Sec. 4). The following proposition proves the sector hierarchy; the corollary gives the effective biased-erasure channel under weak noise and efficient detection of leakage to $|0\rangle$.

Proposition 1 (Noise-sector classification). *Let \hat{V} transform as irrep Γ_V of the defect point group, with RMS amplitude σ . The geometric-phase error of the composite two-loop holonomic gate satisfies:*

(a) A_1 **sector** (S_z^2): $\delta\gamma_{\text{geo}} = 0$ ($S_z^2 = I$ on \mathcal{Q}).

(b) A_2 **sector** (S_z): $\delta\gamma_{\text{geo}} = O(\sigma^2/\Omega_m^2)$. *Destructive interference between the $|B_+\rangle$ and $|B_-\rangle$ channels (“parity filter”) directs the first-order correction into $|0\rangle \perp \mathcal{Q}$, leaving the Berry connection invariant at $O(\sigma)$.*

(c) E **sector** (S_x, S_y): $\delta\gamma_{\text{geo}} = O(\sigma^3/\Omega_m^3)$. *The parity filter reinforces the in-subspace $|B\rangle$ component, modifying the Berry connection at $O(\sigma)$; however, the π -echo between the two NGQC lunes cancels the first- and second-order corrections, with the leading surviving Fourier mode appearing at third order.*

The proof is given in Appendix G. All geometric-phase errors are at least second order in σ/Ω_m (Table XI), so the conditional process error at the optimal magic time is decoherence-dominated. This classification is a general consequence of the Λ -system structure and applies to any platform in Table II.

Remark 2 (Parity-filter duality). In the A_2 sector, the parity filter has a dual role. The same bright-manifold interference that directs $|D^{(1)}\rangle \propto |0\rangle \perp \mathcal{Q}$ (protecting the Berry connection at first order, Face 1) also means that the leading perturbative population transfer exits the computational subspace into the optically distinguishable auxiliary level (Face 2). Explicitly, the first-order dark-state correction under $V = \sigma S_z$ evaluates to $|D^{(1)}\rangle = -[\sigma\langle B|S_z|D\rangle/(\Omega_m/2)]|0\rangle$, which lies entirely outside \mathcal{Q} and therefore points toward the optically distinguishable auxiliary level, providing a microscopic explanation for why A_2 -type mismatch preferentially exits the computational subspace. For E -sector perturbations (S_x, S_y), the interference reverses: $|D^{(1)}\rangle \propto |B\rangle \in \mathcal{Q}$, and suppression relies instead on the π -echo. Thus the geometric-phase

protection and the erasure-dominant noise structure of Corollary 1 are not independent observations but dual consequences of the A_2 -sector parity filter.

TABLE XI. Noise-sector suppression hierarchy from Proposition 1 and the sector-injection diagnostic of Appendix G, Sec. 4. The direction column gives the first-order response fraction projected onto the auxiliary state $|0\rangle$ and logical bright state $|B\rangle$. The scaling column gives the measured perturbative response or phase-error slope; for the E sector, $1 \rightarrow 3$ denotes the change from a single open lune to the π -shifted two-lune echo.

Irrep	Mechanism	First-order direction	Diagnostic scaling
A_1	common mode	none	numerical floor
A_2	parity filter	$f_0 = 1, f_B = 0$	weight slope 2.000
E	bright-directed + π echo	$f_0 = 0, f_B = 1$	phase slope $1 \rightarrow 3$

a. *Numerical sector-injection verification.* To verify that the biased-erasure structure is not merely inferred from the final open-system channel, we performed a sector-injection diagnostic on the ideal three-level Λ Hamiltonian. Equal-norm representatives S_z^2, S_z, S_x , and S_y were injected and the first-order dark-state correction was projected onto the auxiliary direction $|0\rangle$ and the logical bright direction $|B\rangle$. The A_2 perturbation S_z gives $f_{|0\rangle} = 1$ and $f_{|B\rangle} = 0$, while the transverse E -sector perturbations S_x, S_y give $f_{|0\rangle} = 0$ and $f_{|B\rangle} = 1$. The response weights scale quadratically in σ/Ω_m , and the E -sector geometric phase changes from approximately first order without echo to approximately cubic with the two-lune echo. Thus the sector-to-channel map used in Corollary 1 is directly verified at the Λ -manifold level (Appendix G, Sec. 4). The full four-panel diagnostic, including the surface-sector projection, is shown in Fig. S1. The A_2 result does not mean that A_2 noise vanishes; it means that its leading perturbative population is redirected outside \mathcal{Q} , where efficient $|0\rangle$ readout converts it into erasure structure.

The sector-injection response defines an irrep-to-syndrome polarimetry protocol. For a weak perturbation V_Γ , define $\mathcal{R}_{\Gamma \rightarrow c} = \lim_{\sigma \rightarrow 0} p_c[V_\Gamma]/(\sigma/\Omega_m)^2$, where c labels a measured response port. In the equal-Hilbert-Schmidt-norm convention, the clean Λ manifold gives a block-diagonal port response: A_1 is common mode, A_2 routes population response to the auxiliary port, and E routes population response to the logical bright port. For a mixed perturbation $V = \sigma[\cos\alpha S_z + \sin\alpha(\cos\beta S_x +$

$\sin \beta S_y]$, the routing fractions obey $f_0 = \cos^2 \alpha$ and $f_B = \sin^2 \alpha$, independent of β (Appendix G, Sec. 4). Thus the symmetry-generated Λ manifold acts as a crystalline irrep polarimeter: symmetry fixes the sector-to-port map, while the device model fixes the absolute rates.

Corollary 1 (Conditional biased-erasure channel). *Under the assumptions stated above, an A_2 -sector perturbation is parity-filtered preferentially toward auxiliary-state leakage, while the E sector is echo-suppressed. For comparable perturbation strengths, the no-erasure residual is then Z -biased, with*

$$\eta \equiv \frac{p_Z}{p_{XY}} \sim \frac{\Omega_m}{\sigma}. \quad (35)$$

Leakage to the optically distinguishable auxiliary state is converted into a known-location erasure with probability $p_{\text{era}} = \eta_{\text{det}} L$. Thus the simulated gate realizes a biased-erasure channel because the symmetry-enforced Λ hierarchy, the holonomic encoding, and the $|0\rangle$ detection mechanism [45] act together.

Specifically, the extracted Regime-A per-gate noise decomposes into four channels:

1. *Erasure: $p_{\text{era}} = \eta_{\text{det}} L = 0.47\%$, using $\eta_{\text{det}} \geq 97.5\%$. The dominant simulated leakage is produced by the explicit $B_z^{\text{surf}}(t)S_z$ ME-CCE/KMC perturbation and is consistent with the A_2 parity filter; a surface-only sector diagnostic gives $L_{\text{surf}} = 0.456\%$.*
2. *Z dephasing: $p_Z = 0.168\%$, from $T_{1\rho}$ depolarization and residual A_2 -sector geometric-phase error $O(\sigma_{A_2}^2/\Omega_m^2)$.*
3. *Residual depolarizing error: $p_{\text{dep}} = 0.012\%$, from imperfect erasure detection.*
4. *X/Y bit-flip error: at the numerical floor of the extracted Regime-A rotating-frame NV channel, associated with the echo-suppressed E sector and additional thermal suppression of $\Delta m_S = 2$ spin-flip processes at $B_z = 50$ G.*

These probabilities are not group-theoretic constants. Symmetry fixes the allowed system-operator sectors and their perturbative hierarchy; the Regime-A device model fixes the rates.

The nominal noise bias ratio $\eta \equiv p_Z/p_{XY}$ therefore lies far beyond the $\eta \sim 100$ saturation point of the XZZX advantage [72, 73]; finite transverse floors are treated explicitly below as a decoder stress axis, and missed erasures are tracked as a separate validation limit [76]. The resulting channel is a *biased-erasure* channel: dominant erasure errors at known locations, plus a strongly Z -biased non-erasure residual. This places the extracted channel in the biased-erasure-noise setting studied for XZZX-type decoding [75]. This structure arises from the crystallographic hierarchy together with the holonomic encoding,

the modeled bath weights, and erasure detection, rather than from engineered hardware asymmetry alone.

As a conservative baseline, treating the non-erasure error as isotropic depolarizing ($p_{\text{undet}} = p_Z + p_{\text{dep}} = 0.18\%$) and using the code-capacity thresholds $p_{\text{dep}}^{\text{th}} = 10.3\%$ [59] and $p_{\text{era}}^{\text{th}} = 50\%$ [58] yields a Pauli-equivalent effective error rate

$$p_{\text{eff}}^{(\text{iso})} = p_{\text{undet}} + \frac{p_{\text{dep}}^{\text{th}}}{p_{\text{era}}^{\text{th}}} p_{\text{era}} = 0.28\%, \quad (36)$$

requiring fit-extrapolated code distance $d = 11$ (121 data qubits) for $p_L = 10^{-10}$, a 46% code-capacity overhead estimate versus the Rabi gate ($d = 15$, 225 qubits). This estimate, however, discards the Z -bias entirely. The bias-aware analysis of Sec. VI G shows that substantially larger overhead reductions are possible within the same code-capacity model.

G. Biased-erasure decoder estimates and scheduled stress diagnostic

Having verified the microscopic sector-to-channel map, we next ask how the extracted Regime-A biased-erasure channel is seen by a code-capacity decoder. We perform Monte Carlo QEC simulations comparing CSS and XZZX surface codes [72] on the same toric lattice under the extracted noise model of Sec. VI F (5000 trials per data point, minimum-weight perfect matching via Py-Matching; full methodology in Appendix O). This QEC analysis uses the extracted Regime-A rotating-frame NV channel from Table VII. The decoder estimates should be read as model-channel diagnostics of the symmetry-generated biased-erasure mechanism, not as calibrated thresholds for the specific flexural membrane geometry of Fig. 1 or for a particular HBAR transfer function. The SATD Regime-A channel is used for the biased-erasure and XZZX overhead estimates; the single-shot Regime-D suite is used only to establish compact universal non-Abelian control on the same symmetry-generated Λ manifold. The code-capacity layer intentionally isolates decoder response to the extracted biased-erasure channel; below we add a scheduled two-sector detector-model stress diagnostic for the first circuit layer. All physical error rates are uniformly scaled by a common factor $s \in [1, 100]$ to probe behavior near and above threshold.

On the same toric lattice and under the same extracted biased-erasure noise model, CSS and XZZX exhibit opposite finite-size scaling: CSS logical error p_L increases with code distance d for $s \gtrsim 2-5$, indicating near-threshold or above-threshold operation, whereas XZZX p_L decreases monotonically with d at every tested scale including $s = 100$, indicating deeply sub-threshold operation (Fig. 8, Table XII). At $s = 50$ and $d = 11$, the XZZX logical error rate is $197\times$ lower than CSS ($p_L = 0.0034$ versus 0.671). This advantage grows with distance, the hallmark of the two codes residing on opposite sides of

a threshold boundary. No threshold crossing is observed for XZZX up to $100\times$ the physical noise. This opposite scaling behavior is qualitatively significant: it indicates that the extracted biased-erasure noise model places the two codes on opposite sides of the threshold boundary, so that the holonomic gate does not merely lower the physical error rate but changes the *class* of logical noise seen by the code-capacity decoder.

The square-code overhead estimate is obtained from the fitted finite-distance code-capacity scaling: for extrapolated $p_L = 10^{-10}$, the XZZX code under the nominal extracted biased-erasure model requires $d = 9$ ($d^2 = 81$ data qubits), versus $d = 11$ (121 qubits) for the conservative erasure-only CSS baseline and $d = 15$ (225 qubits) for the Rabi gate without erasure conversion, a 64% benchmark code-capacity overhead estimate relative to the Rabi baseline (Table XII). This 64% value is therefore a nominal model-channel estimate, not an architecture-level fault-tolerance overhead. The nominal Regime-A channel lies at the numerically resolved transverse floor. Since this floor is not a group-theoretic constant, we treat p_{XY} as an explicit stress parameter (Fig. 7 and Appendix O, Sec. 6). At $\eta_{\text{det}} = 97.5\%$, the nominal floor gives the $d = 9 / 64\%$ code-capacity saving proxy; finite transverse floors $p_{XY} = 10^{-6}$ – 10^{-4} move the estimate to $d = 11 / 46.2\%$, and $p_{XY} = 10^{-3}$ moves it to $d = 13 / 24.9\%$. Thus transverse faults reduce the decoder advantage continuously rather than invalidating it abruptly.

To connect this decoder axis to physical controls, we also construct a perturbative map from transverse strain noise, quadrature imbalance, SATD calibration errors, hyperfine transverse components, transverse-field misalignment, and HBAR filtering residuals to an effective p_{XY} (Appendix O, Sec. 6). This map defines calibration targets for keeping the channel in the $d = 9$, $d = 11$, or $d = 13$ decoder envelope.

We next embedded the same extracted channel into a scheduled two-sector XZZX detector-model stress diagnostic. The diagnostic uses repeated syndrome rounds, dynamic erasure-aware weights, measurement/reset faults, explicit Z - and X/Y -sector matching graphs, leakage persistence, delayed erasure flags, finite erasure-detection efficiency, and local crosstalk. We use “validation envelope” to mean stress cases that preserve, reduce, or break the nominal $d = 9$ proxy without interpreting the nonmonotonic adversarial slices as calibrated thresholds. In the 50k-shot nominal cleanup, the erasure-aware decoder remains at the 10^{-3} logical-failure proxy scale at $d = 9$, $p_L = 1.00 \times 10^{-3}$ with 95% CI $[0.759, 1.318] \times 10^{-3}$, while the no-flag decoder gives 2.2×10^{-3} . An explicit $p_{XY} = 10^{-3}$ floor moves the proxy from $d = 9$ to $d = 11$, and combined $\eta_{\text{det}} = 0.9$ plus finite- p_{XY} stress remains in the $d = 11/d = 13$ regime. The only stress case that is not recovered by $d = 15$ is $2\times$ local crosstalk, $p_L = 2.6 \times 10^{-3}$ with 95% CI $[1.77, 3.81] \times 10^{-3}$, identifying crosstalk as the leading hardware-specific validation target rather than a weak-

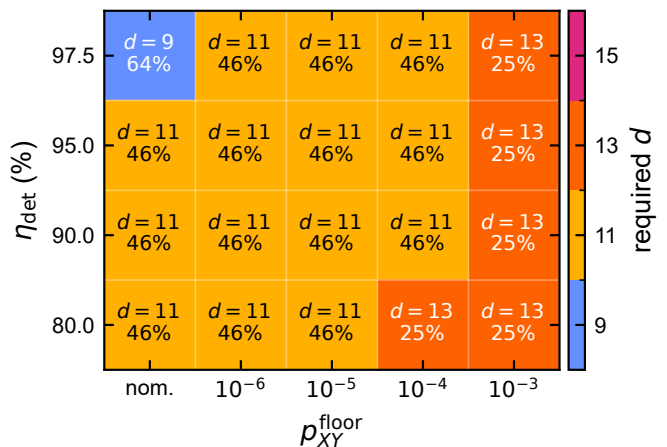


FIG. 7. Transverse-floor validation envelope for the extracted Regime-A biased-erasure channel. Required XZZX distance and corresponding data-qubit saving relative to the $d = 15$ Rabi/CSS baseline are shown as functions of an imposed transverse floor p_{XY}^{floor} and erasure-detection efficiency η_{det} . The nominal extracted channel gives the $d = 9 / 64\%$ proxy, finite floors through 10^{-4} remain in the $d = 11 / 46.2\%$ envelope, and the 10^{-3} stress case moves to $d = 13 / 24.9\%$.

ness of the extracted biased-erasure channel.

Rectangular XZZX planar codes, which exploit the extreme Z -bias by using a short row distance d_r (protecting the rare X -error direction) and a long column distance d_c (protecting the dominant Z -error direction), show no observed failures in 5000 code-capacity trials for all tested $d_r < d_c$ configurations (including the 3×7 code with 21 data qubits) up to $100\times$ the physical noise ($p_L < 7.7 \times 10^{-4}$ at 95% CL; Appendix O). This zero-failure observation only bounds p_L at the 10^{-4} scale and is not extrapolated to 10^{-10} . Because these are finite-statistics code-capacity results, we present the rectangular codes as a promising extension rather than the primary overhead estimate.

VII. DISCUSSION

A. Cross-platform T_1/T_{gate} scaling

The NV spin-qubit ($T_1 = 1$ ms, $T_{\text{gate}} = 1.833 \mu\text{s}$, $T_1/T_{\text{gate}} \approx 546$) validates the full SATD architecture, because the required lower-manifold correction is supplied by the resonant DQ strain channel. The SiV orbital-qubit benchmark ($T_1 = 143$ ns, $T_{\text{gate}} = 46.2$ ns, $T_1/T_{\text{gate}} \approx 3.1$) is the Regime C lower-doublet-free Λ -control benchmark.

Within their respective control assumptions, both platforms follow the scaling $\varepsilon_{\text{dissipative}} \propto T_{\text{gate}}/T_1$ from the $T_1/T_{1\rho}$ Lindbladian error channel (Sec. VIC), whereby the fidelity ceiling is determined entirely by the T_1/T_{gate} ratio, not by the absolute timescale. For Regime A this scaling appears after NGQC + SATD remove the non-adiabatic and singularity errors; for Regime C it appears

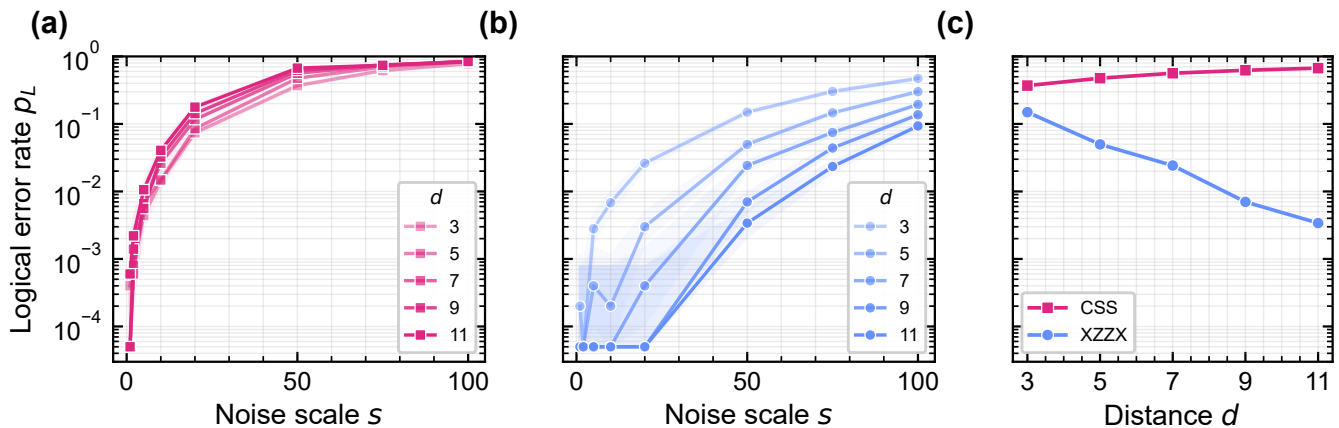


FIG. 8. Decoder-level threshold separation under the extracted biased-erasure noise model. (a) Logical error rate p_L versus noise scale s for CSS toric codes at distances $d = 3$ –11. Lines fan upward with increasing d for $s \gtrsim 2$, indicating above-threshold operation: larger codes perform *worse*. (b) Same plot for XZZX toric codes. Lines fan downward with increasing d at every tested scale including $s = 100$, indicating deeply sub-threshold operation: larger codes provide exponential error suppression. (c) p_L versus d at fixed $s = 50$. CSS (squares) increases with d while XZZX (circles) decreases, yielding a 197 \times advantage at $d = 11$. All data points: 5000 Monte Carlo trials with minimum-weight perfect matching (MWPM) decoding (Appendix O). The conservative erasure-only baseline in Appendix O is superseded by this bias-aware analysis.

TABLE XII. Noise channel decomposition and code-capacity overhead estimate for four gate/code configurations. Physical error rates are from the simulated results of this work (Table VII and Sweep 2). The XZZX bias-aware analysis resolves the non-erasure channel into its Z and depolarizing components, exploiting the symmetry-resolved noise hierarchy of Proposition 1.

	Rabi CSS	Hol. era-CSS	Hol. XZZX square	Hol. XZZX rect. ^a
p_{era}	0	0.47%	0.47%	0.47%
p_Z	—	—	0.168%	0.168%
p_{dep}	0.63%	0.18% ^b	0.012%	0.012%
Code	CSS	CSS	XZZX	XZZX
Distance	15	11	9	3×7
Data qubits	225	121	81	21
Saving vs. Rabi	—	46%	64%	— ^c

^a No failures observed in 5000 code-capacity trials up to 100 \times noise, which bounds p_L only at the 10^{-4} scale; presented as an extension, not an overhead claim.

^b Unresolved p_{undet} ; treated as isotropic depolarizing.

^c Consistent with $\sim 91\%$ reduction in the finite-statistics code-capacity data, but not extrapolated or used as a headline overhead estimate.

after the Λ -leg-only gate time is lengthened enough to recover adiabaticity.

Within a fixed control family and selected commensurability branch, T_{gate} scales approximately as $1/\Omega_m$, and $\varepsilon_{\text{process}} \approx \varepsilon_{\text{coh}} + cT_{\text{gate}}/T_1$ (Eq. (32)), where $\varepsilon_{\text{coh}} \approx 0.003\%$ is the coherent floor. The mechanical Rabi frequency entering this ratio scales linearly with the strain coupling constant ($\Omega_m = g\varepsilon_0$) and thus with the material-specific parameter $g \in \{h_{26}^{\text{NV}}, f_{\perp}^{\text{SiV}}\}$. Any plat-

form satisfying the Theorem 1 selection rule gains immediate access to this scaling via synthetic rotation, provided that at least two degenerate strain modes are simultaneously driven in quadrature.

The SiV single-shot benchmark realizes the second route: a shortcut construction using only the two orbit-strain Λ legs and scalar detuning. At $\Omega_{\text{peak}} = 300$ MHz, it reaches $F_{\text{eff}} > 99.5\%$ across the four-gate suite at $T_{\text{gate}} = 6.667$ ns, with the remaining error set by orbital- T_1 depolarization during auxiliary occupation. Thus SiV is not the preferred platform for the biased-erasure SATD channel, but it is a natural platform for fast non-Abelian single-shot control.

B. C_{3v} platform-selection rule

The same C_{3v} spin-strain tensor structure also suggests a platform-selection rule. At fixed target Ω_m , the off-resonant DQ Stark scale obeys $\delta_{\text{AC}} \propto |h_{16}/h_{26}|^2 \Omega_m^2/D$ [Eq. (23)]. For the assumed 3C-SiC neutral divacancy parameters, this reduces the Stark scale from 20.718 kHz in NV to 0.521 kHz, a factor of 39.76. In a controlled Regime-A comparison using the same SATD echo-lune trajectory, surface-bath traces, T_1 , $T_{1\rho}$, and erasure bookkeeping as the NV channel benchmark, uncompensated 3C-SiC lies essentially on the compensated baseline, while uncompensated NV incurs a visible Stark penalty. This supports the design rule that C_{3v} hosts with small $|h_{16}/h_{26}|$ can preserve the Λ -sector symmetry-to-channel mechanism while suppressing the parasitic DQ Stark channel before active compensation.

This comparison is a controlled Hamiltonian comparison, not a measured 3C-SiC device forecast. A deployable

claim requires platform-specific surface noise, relaxation, strain limits, mechanical mode shapes, optomechanical coupling, and auxiliary-state detection.

C. Toward universal SU(2) control

The merged architecture separates universal control from QEC channel engineering. The SATD echo-lune compiler is optimized for the Regime-A biased-erasure channel, while the single-shot compiler gives the simpler universal layer. In the latter, the rotation axis \mathbf{n} is set by the relative amplitude and phase of the two Λ legs, and the rotation angle $\gamma = \pi(1 + \sin \alpha)$ is set by the detuning ratio. Thus a single cyclic bright-state pulse implements $U_L(\mathbf{n}, \gamma) \doteq \exp[-i\gamma \mathbf{n} \cdot \boldsymbol{\sigma}/2]$. Changing \mathbf{n} changes the bright-state projector, so nonparallel pulses generate noncommuting holonomies natively rather than through a compiled sequence of adiabatic loops.

Optical [61] and microwave [62] holonomic-gate demonstrations on NV centers have established the viability of geometric-phase control; the present architecture replaces the photonic/MW drive with the symmetry-generated strain Λ manifold and supplies two compilers on that manifold.

This universal SU(2) control is currently restricted to a single subsystem per mode pair. Multi-qubit entangling gates require phonon-mediated coupling between distinct defect centers, which is beyond the present single-qubit framework. The same bright-state projector also gives a compact entangling extension at the effective Λ level. Consider two Λ manifolds coupled to one detuned mechanical mode through their logical bright projectors,

$$K_I(t) = (f_1 P_{b1} + f_2 P_{b2}) (ae^{-i2\pi\delta t} + a^\dagger e^{i2\pi\delta t}), \quad (37)$$

where $K = H/h$. After one closed bus loop, $T = 1/\delta$, the displacement vanishes and the remaining geometric phase is

$$U(T) = \exp\left[i\frac{2\pi}{\delta^2} (f_1 P_{b1} + f_2 P_{b2})^2\right]. \quad (38)$$

Since $P_b^2 = P_b$, the nonlocal phase is

$$U_{\text{ent}} = \exp\left[i\frac{4\pi f_1 f_2}{\delta^2} P_{b1} P_{b2}\right]. \quad (39)$$

For $f_1 = f_2 = \delta/2$, this gives a π phase on the joint bright state. Choosing the bright axes along logical Z makes the gate locally equivalent to CZ, up to single-qubit Z phases. This is an effective projector-force identity, not yet a microscopic actuator-level theorem. The corresponding validation is therefore treated as Regime F and reported as an architecture diagnostic.

Regime F tests this extension in a two-qutrit Λ model coupled to a truncated oscillator. At $f = 2.0$ MHz, $\delta = 4.0$ MHz, $Q = 10^7$, $T = 0.25$ μ s, and $n_{\text{Fock}} = 16$, the extracted CZ-class channel gives conditional $F_{\text{avg}} =$

99.8096%, $p_{\text{era}} = 0.04874\%$, $p_Z = 0.23775\%$, $p_{ZZ} = 0.000229\%$, and no measurable XY component. The result is bias-preserving and biased-erasure compatible, but not erasure-dominated, since $p_Z/p_{\text{era}} = 4.88$. A repeated-syndrome XZZX proxy using the combined one- and two-qubit channels gives no logical failures at the base scale for distances 3, 5, 7 over 400 shots; full data and cross-checks are in Appendix Q.

D. Symmetry-to-decoder design principle

The results of this work reveal a design principle: crystallographic symmetry can be promoted from a control-enabling constraint to a symmetry-to-decoder design principle whose influence propagates from the microscopic Hamiltonian to code-capacity logical-code overhead estimates.

The chain has four links, each shaped by the two-dimensional irreducible representation Γ_E :

1. **Gate mechanism.** The dot-product coupling mandated by $\Gamma_E \otimes \Gamma_E \supset \Gamma_{A_1}$ (Theorem 1) enables synthetic rotation and thereby holonomic control.
2. **Noise classification.** The Λ -system bright manifold created by the same coupling produces a parity filter that classifies noise errors by irrep: $A_1 \rightarrow 0$, $A_2 \rightarrow O(\sigma^2)$, $E \rightarrow O(\sigma^3)$ (Proposition 1).
3. **Conditional biased-erasure channel.** The parity-filter duality (Remark 2) directs A_2 -sector perturbations toward the heraldable auxiliary level, while the π -echo suppresses E -sector errors. For weak noise with comparable irrep-sector bath weights and efficient $|0\rangle$ detection, this yields the biased-erasure channel (Corollary 1).
4. **Decoder estimates and stress diagnostic.** In code-capacity simulations of the nominal extracted channel, the resulting biased-erasure noise model places CSS and XZZX codes on opposite sides of the threshold boundary, producing a 64% fit-extrapolated benchmark overhead estimate whose finite-transverse-floor and erasure-detection sensitivity is quantified in Fig. 7 and Appendix O, Sec. 6; a scheduled two-sector detector-model stress diagnostic then tests the first circuit layer and identifies strong local crosstalk as the leading architecture-specific validation target (Sec. VI G).

A common Γ_E symmetry provides the control structure (link 1) and the noise hierarchy (links 2–3); the full estimated overhead advantage then emerges from co-design of encoding, leakage-detection mechanism, holonomic control, and decoder (link 4), and its numerical value remains tied to the simulated channel parameters and validation level used here. In this chain, links 2–4 refer specifically to the SATD Regime-A NV channel. Regime D establishes universal control on

the same Λ manifold, but it is not the source of the XXXX overhead number. This perspective suggests a broader principle: for solid-state platforms with sufficiently rich point-group symmetry, co-design across the encoding, gate, and decoder layers may extract decoder advantages that are inaccessible to any single layer optimized in isolation; establishing the quantitative overhead in a hardware-calibrated architecture-level detector-error model remains future work.

An important aspect of this chain is the role of encoding. Under Rabi driving in the $\{|0\rangle, |+1\rangle\}$ subspace, T_1 relaxation is an in-subspace error (non-heralded), whereas in the holonomic $\{|-1\rangle, |+1\rangle\}$ encoding, the same T_1 decay populates $|0\rangle$ outside the computational subspace, converting it to a heralded erasure. Combined with the parity-filter noise shaping and the π -echo, the joint choice of encoding and gate protocol reshapes the effective noise class on the *same physical hardware* from a conservatively treated unstructured dynamical-gate baseline to an extracted biased-erasure channel. For the nominal extracted channel this gives the 64% code-capacity overhead estimate of Table XII; finite bit-flip floors and imperfect erasure detection reduce this advantage as quantified in the supplement.

E. Beyond defect centers

The defect platforms considered here are experimentally mature realizations of a more general symmetry criterion. The synthetic-rotation construction requires neither a vacancy nor an impurity in an essential way; it requires a strain-active Λ manifold whose projected strain and transition operators share a two-dimensional irrep of the effective device symmetry. For point defects this is the crystallographic defect point group, whereas for acceptor, valley-orbital, hole-spin, or gate-defined manifolds it is the little group left after crystal symmetry, confinement, device geometry, static fields, and strain-mode symmetry are all imposed. The generalization is conditional: platforms with only one-dimensional irreps, strong symmetry breaking, or no phase-locked degenerate strain-mode pair may still allow engineered two-axis mechanical control, but they do not inherit the symmetry-protected circular-strain selection rule.

F. Minimal experimental tests

A decisive first demonstration need not implement the full fault-tolerance stack. The minimal experimental program is:

1. demonstrate two phase-locked mechanical modes with calibrated quadrature phase at the defect site;
2. measure circular-strain selectivity between the two Λ legs, including handedness reversal;

3. verify that symmetry-preserving perturbations primarily renormalize the scalar coupling rather than mixing handedness;
4. implement one holonomic loop and compare it with a linearly driven mechanical baseline;
5. detect leakage into the auxiliary state as a heralded erasure channel.

Passing these tests would establish the central quantum-information claim: crystallographic symmetry has generated not only a control field, but a Λ -control resource with observable gate and error-channel consequences.

G. Experimental outlook

The NV membrane variant requires a (100)-oriented diamond plate ($L \sim 10 \mu\text{m}$, $h_m \sim 200 \text{nm}$), two piezoelectric transducers for quadrature driving, and DC electrodes for electrostatic degeneracy tuning [63]; all components have been individually demonstrated [13, 37]. The GHz HBAR variant retains the same quadrature topology (Appendix H), but its finite acoustic bandwidth means that the fast Regime-A envelope cannot be assumed without predistortion, reduced effective Q , or a slower HBAR-specific waveform. The SiV orbital platform requires $\Omega_m \geq 300 \text{MHz}$ at millikelvin temperatures, which is within reach of recent SiV-resonator demonstrations [20]. In situ calibration of Ω_m is achievable via strain-modulation spectroscopy [13, 14], with the ideal bright-state spacing $\Delta T = 1/\Omega_m$ providing a secondary calibration signature. A step-by-step experimental protocol is given in Appendix K. The 3C-SiC neutral-divacancy comparison in Sec. VII B identifies a complementary platform-design direction within the same C_{3v} class.

VIII. CONCLUSION

We have introduced crystallographic symmetry as a quantum-information resource for phononic solid-state processors. The central result is a shared-irrep selection rule: when the projected strain tensor and transition operators of a strain-active Λ manifold share a multiplicity-one two-dimensional irrep, symmetry fixes the linear strain interaction to a scalar dot product. Two degenerate mechanical modes driven in quadrature then synthesize a complex circular Λ drive. Defect centers with C_{3v} and D_{3d} symmetry provide experimentally developed realizations, but the criterion itself is representation-theoretic and applies to any effective device manifold satisfying the same shared-irrep condition.

For NV centers, the full composite NGQC + SATD protocol is modeled in Regime A with a resonant double-quantum strain tone realizing the exact counter-diabatic operators. Open-system simulations give a Regime A

conditional $F_{\text{avg}} = 99.88\%$ at $T_{\text{gate}} = 1.833\ \mu\text{s}$, with $F_{\text{avg}}^{\text{eff}} = 99.40\%$ after leakage is counted as error. Regime B gives the corresponding GHz-HBAR projection at resonant-drive Rabi frequencies and treats envelope filtering as an implementation constraint rather than as part of the Regime-A erasure extraction. For SiV centers, Regime C gives a conservative Λ -leg-only orbital-control benchmark with $F_{\text{avg}} = 96.32\%$ at $46.2\ \text{ns}$. On the same symmetry-generated Λ manifold, Regime D validates a single-shot bright-state compiler for compact universal non-Abelian $\text{SU}(2)$ control, with $F_{\text{eff}} \simeq 99.86\%$ across a representative gate suite at $T_{\text{gate}} = 0.9009\ \mu\text{s}$. Regime E applies that compiler directly to the SiV orbital Λ manifold using only orbit-strain Λ legs and scalar detuning, reaching $F_{\text{eff}} = 99.52\%$ – 99.67% across the four-gate suite at $T_{\text{gate}} = 6.667\ \text{ns}$ without assuming a lower-doublet SATD actuator.

The same symmetry that enables synthetic rotation also organizes the noise response. In the Regime-A NV channel benchmark, the Γ_E -enabled Λ manifold produces a perturbative hierarchy in which A_1 perturbations are common-mode, A_2 perturbations preferentially generate auxiliary-state leakage, and E -sector bit-flip errors are echo-suppressed. Sector-injection diagnostics verify this map directly: A_2 perturbations point toward $|0\rangle$, whereas E perturbations point toward the logical bright state and require the two-lune echo. Combined with erasure detection, this yields an extracted biased-erasure channel. Code-capacity simulations of the nominal extracted channel give a substantial XZZX overhead reduction relative to an unstructured dynamical-gate baseline, with supplemental sensitivity tests showing how finite p_{XY} floors and imperfect erasure detection reduce that estimate. This overhead estimate is tied to the SATD Regime-A channel; the single-shot suite is the universal-gate validation rather than a second architecture-level QEC claim. Likewise, the membrane and HBAR calculations are implementation routes for the same control Hamiltonian: the membrane topology does not by itself validate the erasure advantage, and HBAR-specific residuals enter through the explicit transverse-floor and missed-flag stress envelopes.

These results support a broader design principle: crystallographic symmetry can be used not only to enable control, but to co-design the encoding, gate, noise bias, and decoder. The matched-environment 3C-SiC comparison turns the same principle into a platform-selection rule: smaller $|h_{16}/h_{26}|$ within the C_{3v} class suppresses the parasitic DQ Stark burden while preserving the Λ -sector mechanism. Finally, the decoder analysis now spans both the nominal code-capacity model and a scheduled two-sector detector-model stress diagnostic, complementing broader erasure-qubit architecture analyses [77]. The former gives the 64% model-channel saving; the latter shows that the nominal biased-erasure advantage survives the first circuit layer and isolates strong local crosstalk as the dominant hardware-specific validation target for a calibrated architecture-level detector-error

model. The bright-state-projector structure also points toward phonon-bus entangling gates; the effective-model analysis in the Supplement suggests a CZ-class phase-biased extension, but a hardware-level two-qubit gate requires a separate Λ -actuator validation.

IX. AUTHOR CONTRIBUTIONS

E.M.M. conceived the project, developed the theoretical model, performed the numerical simulations, and wrote the manuscript. K.A. reviewed the manuscript, provided logistical support, and supervised the project. All authors contributed to the interpretation of the results and the finalization of the manuscript.

ACKNOWLEDGMENTS

We thank Eikichi Kimura and Masato Koga for insightful discussions and valuable feedback that helped improve this work. This research was supported by JSPS KAKENHI Grant Number 24K21730.

DATA AVAILABILITY

All simulation code (Python modules), raw sweep data (JSON), and figure-generation scripts are deposited in a public repository at <https://github.com/E-zClap/PhononQ>. The repository includes software requirements in `requirements.txt` and execution instructions for reproducing the ten core parametric sweeps (Sweeps 1–10).

SUPPLEMENTAL MATERIAL

Appendix A: Biharmonic mode analysis

The flexural dynamics of a thin isotropic plate are governed by the Kirchhoff–Love equation $D_{\text{bend}} \nabla^4 w + \rho h_m \ddot{w} = 0$ with flexural rigidity

$$D_{\text{bend}} = \frac{Y h_m^3}{12(1 - \nu^2)} \approx 7.08 \times 10^{-10} \text{ J}, \quad (\text{A1})$$

where all parameters are as defined in Sec. IV C of the main text and main-text Fig. 1. Simply-supported eigenmodes $w_{nm} \propto \sin(n\pi x/L) \sin(m\pi y/L)$ have eigenfrequencies $f_{nm} = (\pi/2L^2) \sqrt{D_{\text{bend}}/\rho h_m} (n^2 + m^2)$. For (1,2)/(2,1): $n^2 + m^2 = 5 \Rightarrow f_0 = 78.8 \text{ MHz}$.

The lumped parameters are: $m_{\text{eff}} = \rho L^2 h_m/4 = 17.6 \text{ pg}$, $k_{\text{mech}}^{\text{SS}} = m_{\text{eff}} \omega_0^2 = 4310 \text{ N m}^{-1}$, $k_{\text{mech}}^{\text{clamp}} \approx 9530 \text{ N m}^{-1}$ (stiffness ratio 2.21 from Leissa’s tabulated eigenvalues).

Appendix B: Strain topology at candidate NV sites

At the off-center site ($L/4, L/4$):

$$\left. \frac{\partial w_{12}}{\partial x} \right|_{L/4} = +\frac{\pi}{\sqrt{2}L}, \quad \left. \frac{\partial w_{12}}{\partial y} \right|_{L/4} = 0, \quad (\text{B1})$$

$$\left. \frac{\partial w_{21}}{\partial x} \right|_{L/4} = 0, \quad \left. \frac{\partial w_{21}}{\partial y} \right|_{L/4} = +\frac{\pi}{\sqrt{2}L}. \quad (\text{B2})$$

Each mode selects one orthogonal strain-channel direction in the topology model, with equal magnitude. The in-plane correction introduces a minor ellipticity $\eta = (3/2)(|h_{25}|/|h_{26}|)(\pi|z|/\kappa_s L) \approx 4.3\%$, contributing $\mathcal{O}(\eta^2) \lesssim 2 \times 10^{-3}$ to the fidelity error. This thin-plate result is used as a strain-topology guide; the actual local Rabi rate must be calibrated experimentally or supplied by the resonant HBAR route.

Appendix C: Electrostatic tuning law

For an asymmetric membrane with $L_y = L_0(1 + \delta)$, Taylor expansion of the biharmonic eigenvalues gives

$$\frac{\Delta f}{f_0} = 0.6 \delta. \quad (\text{C1})$$

For $\delta = 1\%$: $\Delta f = 0.47 \text{ MHz}$.

The electrostatic spring-softening stiffness is $k_{\text{el}} = -\varepsilon_0 A_{\text{eff}} V^2/d^3$ (here ε_0 denotes the vacuum permittivity). The required voltage evaluates to $V_{\text{req}} = 21.6 \text{ V}$ for a full-area electrode, safely below $V_{\text{bd}} = 35 \text{ V}$, a conservative design voltage rather than a geometry-calibrated breakdown threshold; it is informed by nanoscale vacuum-gap breakdown and MEMS field-emission studies [70, 71]. A 50%-coverage electrode requires 30.5 V, eliminating

safety margin; full-area coverage is therefore mandatory. For gigahertz high-overtone bulk acoustic resonator (GHz-HBAR) devices (Appendix H), residual frequency mismatch between the mechanical overtone and the NV zero-field splitting D can be fine-tuned in situ via the known temperature dependence $dD/dT \approx -74 \text{ kHz K}^{-1}$, providing sub-kHz resolution at millikelvin stability, complementary to the coarse RIE adjustment of the HBAR thickness.

Appendix D: Derivative-removal-by-adiabatic-gate (DRAG) and superadiabatic transitionless driving (SATD) Hamiltonian derivation

The adiabatic dark and bright eigenstates of the RWA Hamiltonian are

$$|D\rangle = \cos(\theta/2)|-1\rangle + \sin(\theta/2)e^{i\phi}|+1\rangle, \quad (\text{D1})$$

$$|B\rangle = \sin(\theta/2)|-1\rangle - \cos(\theta/2)e^{i\phi}|+1\rangle. \quad (\text{D2})$$

The non-adiabatic coupling $\langle B|\partial_t|D\rangle = -\dot{\theta}/2$ drives leakage. The exact counter-diabatic Hamiltonian canceling this coupling is [26]

$$H_{\text{CD}} = i\lambda \frac{\dot{\theta}}{2} (|D\rangle\langle B| - |B\rangle\langle D|), \quad (\text{D3})$$

which in the bare basis gives the counter-diabatic operator used in Eqs. (4) and (6) of the main text. For $\lambda = 1$ (exact SATD), this perfectly cancels leakage at all speeds; for the heuristic DRAG variant, λ is scanned empirically.

Appendix E: Hardware decomposition of the SATD correction

The counter-diabatic Hamiltonian used in the simulations is not a third abstract control axis. For the NV implementation it is realized by a resonant double-quantum (DQ) strain tone on the $|-1\rangle \leftrightarrow |+1\rangle$ transition. This section gives the laboratory decomposition and separates this resonant SATD use of the DQ tensor from the off-resonant DQ Stark shift derived in Appendix J.

In angular-frequency units the SATD term is

$$\frac{H_{\text{CD}}}{\hbar} = -\frac{\dot{\theta}}{2} [\sin \phi \text{Op}_{\text{re}} + \cos \phi \text{Op}_{\text{im}}], \quad (\text{E1})$$

with $\text{Op}_{\text{re}} = |-1\rangle\langle+1| + |+1\rangle\langle-1|$ and $\text{Op}_{\text{im}} = i(|+1\rangle\langle-1| - |-1\rangle\langle+1|)$. In the rotating frame of the resonant DQ transition, a phase-controlled DQ strain tone has the form

$$\frac{H_{\text{DQ}}^{\text{res}}}{\hbar} = \frac{1}{2} [\Omega_{\text{re}}(t) \text{Op}_{\text{re}} + \Omega_{\text{im}}(t) \text{Op}_{\text{im}}], \quad (\text{E2})$$

where Ω_{re} and Ω_{im} are angular Rabi rates set by the two quadratures of the resonant DQ drive. Exact Hamiltonian matching to Eq. (E1) is therefore obtained with

$$\Omega_{\text{re}}(t) = -\dot{\theta}(t) \sin \phi(t), \quad \Omega_{\text{im}}(t) = -\dot{\theta}(t) \cos \phi(t). \quad (\text{E3})$$

Equivalently, the lower-manifold matrix element is

$$\frac{H_{\text{CD}}}{\hbar} = \frac{i\dot{\theta}}{2} e^{i\phi} |-1\rangle\langle +1| + \text{h.c.} \quad (\text{E4})$$

Thus a resonant DQ drive with angular Rabi frequency

$$\Omega_{\text{DQ,CD}}(t) = |\dot{\theta}(t)|, \quad \varphi_{\text{DQ}}(t) = \phi(t) + \frac{\pi}{2} + \pi \Theta[-\dot{\theta}(t)] \quad (\text{E5})$$

implements exactly the two operators included in the numerical Hamiltonian. In ordinary frequency units, $\Omega_{\text{DQ,CD}}/(2\pi) = |\dot{\theta}|/(2\pi)$. Equivalently, the coefficient multiplying each Pauli-like operator in Eq. (E2) is smaller by a factor of two; this is the origin of the two common quoted cycle-frequency scales for the same drive.

For NV^- the carrier frequency is the energy splitting within the computational doublet,

$$f_{\text{DQ}} = 2\gamma_e B_z \simeq 280 \text{ MHz} \quad (B_z = 50 \text{ G}), \quad (\text{E6})$$

not the single-quantum frequencies $D_{\pm} = D \pm \gamma_e B_z$ used for the two Λ legs. The same C_{3v} DQ spin-strain tensor $h_{16}(S_x^2 - S_y^2, 2\{S_x, S_y\})$ therefore supplies the SATD control when driven resonantly at f_{DQ} . For the optimal NV gate time $T_{\text{gate}} = 1.833 \mu\text{s}$ and the two-loop trajectory $\theta(t) = \pi \sin(\pi t/\tau)$ with $\tau = T_{\text{gate}}/2$,

$$\max |\dot{\theta}| = \frac{2\pi^2}{T_{\text{gate}}}, \quad \frac{\Omega_{\text{DQ,CD}}^{\text{max}}}{2\pi} = \frac{\pi}{T_{\text{gate}}} \simeq 1.71 \text{ MHz}. \quad (\text{E7})$$

Thus the full resonant DQ Rabi rate is 1.71 MHz, while the Hamiltonian coefficient in Eq. (E2) is $\Omega_{\text{DQ,CD}}^{\text{max}}/(4\pi) \simeq 0.86 \text{ MHz}$ in cycle-frequency units. Using $h_{16} = 19.66 \text{ GHz strain}^{-1}$, the corresponding peak additional DQ strain required for the SATD tone is

$$\varepsilon_{\text{DQ,CD}}^{\text{max}} = \frac{\Omega_{\text{DQ,CD}}^{\text{max}}/2\pi}{|h_{16}|} \simeq 8.7 \times 10^{-5}, \quad (\text{E8})$$

or 4.4×10^{-5} if one quotes the half-rate Hamiltonian coefficient rather than the full DQ Rabi rate. Both conventions are well below the main single-quantum strain amplitude used for the NV benchmark.

For the assumed 3C-SiC neutral-divacancy parameters used in the matched C_{3v} comparison, the same SATD condition requires

$$\varepsilon_{\text{DQ,CD}}^{\text{max}}(3\text{C-SiC}) = \frac{\pi/T_{\text{gate}}}{|h_{16}^{3\text{C-SiC}}|} \simeq 1.27 \times 10^{-3}. \quad (\text{E9})$$

Thus 3C-SiC suppresses the parasitic off-resonant Stark channel but requires a larger intentional resonant SATD strain than NV. This is still below a percent-level strain scale in the parameter check, but it requires a dedicated SiC mechanical actuator design.

The bandwidth requirement is set by the SATD envelope, not by mechanical ring-down. The smooth part of the DQ envelope varies on the sub-loop timescale $\tau = T_{\text{gate}}/2$, giving an envelope bandwidth of order

$1/\tau \simeq 1.1 \text{ MHz}$. The programmed phase step at the South Pole occurs where $\dot{\theta} = 0$, so it does not require a large-amplitude broadband burst; experimentally it can be implemented as a phase update through the zero of the DQ envelope or by standard RF pre-distortion of the transducer response.

This resonant DQ SATD tone is distinct from the off-resonant DQ Stark shift. The Stark term arises because the two single-quantum Λ -leg drives at D_{\pm} also couple to the DQ tensor but are detuned from the $|-1\rangle \leftrightarrow |+1\rangle$ transition by approximately D . Its effect is therefore second-order and dispersive. In contrast, the SATD tone is a deliberate first-order resonant drive at $2\gamma_e B_z$ with a prescribed amplitude and phase; its Hamiltonian is exactly the operator pair used in the simulations.

For SiV^- we do not assume such a lower-doublet SATD control in the revised benchmark. The orbit-strain selection rule establishes the two Λ legs between the lower and upper orbital branches, but the manuscript does not identify a measured strain matrix element that resonantly couples the two lower-doublet computational states with the phase and bandwidth required by Eq. (E5). We therefore use the conservative SiV benchmark with $\alpha_{\text{CD}} = 0$, keeping the same open-system model but removing the lower-manifold SATD Hamiltonian. The best millikelvin benchmark points are

Ω_m (MHz)	T_{gate} (ns)	F_{avg}	Leakage
100	99.23	91.18%	7.96%
300	46.24	96.32%	3.85%
500	123.31	90.14%	8.64%

The previously quoted SiV SATD numbers should therefore be read only as an ideal lower-manifold-control upper bound unless a physical SiV lower-doublet SATD channel is supplied.

Appendix F: Decoherence channel inventory

Table S1 summarizes the complete decoherence environment.

Appendix G: Symmetry protection and noise-sector proof

This appendix proves the two formal claims used in the main text and then records the sector-injection validation of the resulting sector-to-channel map. Section G.1 proves Theorem 1: the Γ_E strain-defect coupling is a unique scalar invariant, and non-scalar bilinears require explicit symmetry-breaking spurions. Section G.2 proves Proposition 1 and Corollary 1: once the protected coupling generates the ideal Λ manifold, weak perturbations are filtered into distinct A_1 , A_2 , and E error channels. Sections G.4–G.5 give the numerical sector-injection and compact robustness diagnostics.

TABLE S1. Decoherence channel inventory. Channels included in the model (top), and channels excluded with justification (bottom).

Channel	Mechanism	Status	Note
Surface spin hopping	ME-CCE KMC	Included	Dominant for shallow NV
Dipolar field fluctuation	B_z^{surf} sum	Included	Direct coupling to qubit
Quasi-static T_2^*	Inter-trajectory DC offsets	Included	Restored by removing variance normalization
T_1 relaxation	Lindbladian collapse	Included	$T_1 = 1$ ms
$T_{1\rho}$ depolarization	Lindbladian collapse	Included	$T_{1\rho} = 500$ μ s; reduced by enrichment
AC Stark shift (S_z)	Double-quantum tensor	Included	Suppressed by NGQC (Theorem 2 of the main text)
^{13}C nuclear bath	Flip-flop dynamics	Excluded	Slow ($T_{\text{gate}} \ll T_2^{\text{C}^{13}}$)
Charge noise	Electric field	Excluded	< 1 kHz dephasing
Mechanical damping	$1/Q$ loss	Excluded	$Q > 10^4$; stable over T_{gate}

1. Group-theoretic protection of the synthetic-rotation selection rule

Let $\epsilon = (\epsilon_1, \epsilon_2)$ and $\mathbf{O} = (O_1, O_2)$ transform under the same real two-dimensional irreducible representation Γ_E of the defect point group G . For D_{3d} centers, the same statements hold with E, A_1, A_2 replaced by E_g, A_{1g}, A_{2g} .

The most general linear strain-defect coupling can be written

$$H_\epsilon = \epsilon^T C \mathbf{O} = \sum_{i,j=1}^2 \epsilon_i C_{ij} O_j.$$

Under a point-group operation $g \in G$,

$$\epsilon \mapsto R_E(g)\epsilon, \quad \mathbf{O} \mapsto R_E(g)\mathbf{O}.$$

Invariance of H_ϵ requires

$$R_E(g)^T C R_E(g) = C \quad \forall g \in G.$$

Because Γ_E is irreducible, Schur's lemma gives $C = g_0 I_2$. Therefore the only G -invariant linear coupling is

$$H_\epsilon = g_0(\epsilon_1 O_1 + \epsilon_2 O_2).$$

Equivalently, the character formula

$$n_\lambda = \frac{1}{|G|} \sum_{g \in G} \chi_E(g)^2 \chi_\lambda^*(g)$$

gives

$$E \otimes E = A_1 \oplus A_2 \oplus E$$

for C_{3v} and

$$E_g \otimes E_g = A_{1g} \oplus A_{2g} \oplus E_g$$

for D_{3d} . A convenient bilinear basis is

$$B_{A_1} = \epsilon_1 O_1 + \epsilon_2 O_2,$$

$$B_{A_2} = \epsilon_1 O_2 - \epsilon_2 O_1,$$

and

$$\mathbf{B}_E = (\epsilon_1 O_1 - \epsilon_2 O_2, \epsilon_1 O_2 + \epsilon_2 O_1).$$

Only B_{A_1} is a scalar. The A_2 and E bilinears can enter the Hamiltonian only if the device or environment supplies spurions χ_{A_2} or χ_E transforming in the corresponding irreps:

$$H_\epsilon = g_0 B_{A_1} + \chi_{A_2} B_{A_2} + \chi_E \cdot \mathbf{B}_E.$$

Thus a G -preserving perturbation can renormalize g_0 but cannot generate ellipticity, handedness mixing, or anisotropic strain coupling at first order.

For a quadrature drive,

$$\epsilon_1(t) = \epsilon_0 \cos \omega_d t, \quad \epsilon_2(t) = \epsilon_0 \sin \omega_d t,$$

define $O_\pm = O_1 \pm i O_2$. Substitution gives

$$H_\epsilon(t) = \frac{g_0 \epsilon_0}{2} (O_+ e^{-i\omega_d t} + O_- e^{+i\omega_d t}).$$

When ω_d is resonant with one arm of the Λ system and the opposite circular component is detuned by Δ_{off} , the rotating-wave approximation is valid for

$$\Omega_m, |\dot{\theta}|, |\dot{\phi}|, \sigma, |\Delta_m| \ll \Delta_{\text{off}}, \omega_d.$$

The resonant component then gives the single-arm circular Hamiltonian used in the main text. This completes the proof of Theorem 1.

2. Scope of the noise-sector statement

The point-group argument above determines the allowed operator sectors and the protection of the circular strain selection rule. The following noise-sector argument determines the perturbative scaling of geometric errors once the ideal Λ manifold has been generated. It does not determine scalar Lindblad rates. We assume: (i) $\sigma/\Omega_m \ll 1$; (ii) the system operators appearing in the system-bath coupling decompose into A_1, A_2 , and E irreducible tensor sectors; (iii) the bath spectral weights are

not parametrically concentrated in the E sector; (iv) device asymmetries do not introduce leading symmetry-breaking Lindblad operators; and (v) population in $|0\rangle$ is detected as an erasure with efficiency η_{det} . Under these assumptions, the symmetry-derived hierarchy implies the biased-erasure channel used in the main text. The ME-CCE/KMC bath used in the Regime-A simulation is a more specific case: it is injected through the system operator $B_z^{\text{surf}}(t)S_z$, i.e. the A_2 sector. Its erasure rate is therefore a numerical simulation result, not a prediction of representation theory alone.

Supplemental Theorem G1 (Conditional symmetry selection of the biased-erasure channel). Let the controlled Λ system be generated by the same two-dimensional irrep Γ_E that appears in the strain tensor, with bright states $|B_{\pm}\rangle = (|B\rangle \pm |0\rangle)/\sqrt{2}$ and energies $\pm\Omega_m/2$. Under the assumptions above, the effective per-gate channel can be written as

$$\mathcal{E}(\rho) = (1 - p_{\text{era}})\mathcal{E}_{\mathcal{Q}}(\rho) + p_{\text{era}}\mathcal{E}_{\text{flag}}(\rho), \quad (\text{G1})$$

where $\mathcal{E}_{\text{flag}}$ is a known-location erasure channel. The no-erasure conditional channel has a strongly Z -biased perturbative hierarchy,

$$p_Z = O(\sigma_{A_2}^2/\Omega_m^2) + p_{T_1\rho} + p_{\text{det}}, \quad (\text{G2})$$

$$p_{XY} \lesssim C_E(\sigma_E/\Omega_m)^3 + p_{\text{therm}} + p_{\text{ctrl}}, \quad (\text{G3})$$

so that comparable system-operator sector strengths give $p_Z/p_{XY} \sim \Omega_m/\sigma \gg 1$. Here p_{therm} denotes thermally activated spin-flip processes and p_{ctrl} denotes residual control imperfections. The group theory fixes the perturbative hierarchy, while the numerical model fixes the coefficients and additive device-dependent contributions.

Proof of Proposition 1. (a) A_1 sector ($\hat{V} = S_z^2$, etc.).— Because $S_z^2 = I$ on $\mathcal{Q} = \text{span}\{|-1\rangle, |1\rangle\}$, \hat{V} acts as a common-mode shift and produces no $|D\rangle\text{--}|B\rangle$ coupling at any order: $\delta\gamma_{\text{geo}} = 0$.

*(b) A_2 sector ($\hat{V} = S_z$).—*The matrix elements $\langle B_{\pm}|S_z|D\rangle$ have the *same* sign, while the energy denominators $E_D - E_{B_{\pm}} = \mp\Omega_m/2$ have opposite sign. The perturbative weights therefore cancel in the $|B\rangle$ component, yielding $|D^{(1)}\rangle \propto |0\rangle \perp \mathcal{Q}$. Since $\partial_{\mu}|D\rangle \in \mathcal{Q}$ and $\langle 0|\partial_{\mu}D\rangle = 0$, the Berry connection is invariant: $\delta\mathcal{A}_{\mu}^{(D)} = 0$ at $O(\sigma)$, and $\delta\gamma_{\text{geo}} = O(\sigma^2/\Omega_m^2)$.

*(c) E sector ($\hat{V} = S_x, S_y$).—*The matrix elements $\langle B_{\pm}|S_x|D\rangle$ have *opposite* sign, so the weights reinforce in the $|B\rangle$ component: $|D^{(1)}\rangle \propto |B\rangle \in \mathcal{Q}$. The Berry connection is modified at $O(\sigma)$. However, the first-order correction $\delta\mathcal{A}_{\theta} \propto \sin(\theta/2)\sin\phi$ is odd under the π -echo ($\phi_0 \rightarrow \phi_0 + \pi$), so the line integrals from the two NGQC lunes cancel: $\oint \delta\mathcal{A} dl = 0$ at $O(\sigma)$. At second order the relevant Berry-connection correction $\delta\mathcal{A}_{\theta}^{(2)} \propto c^*\partial_{\theta}c$ contains exclusively $n = \pm 1$ Fourier modes in ϕ (no $n = 0$ component), because $c^*\partial_{\theta}c = \frac{1}{4}[\cos^2\frac{\theta}{2}e^{i\phi} - \sin^2\frac{\theta}{2}e^{-i\phi}]$. These $n = \pm 1$ modes are odd under $\phi_0 \rightarrow \phi_0 + \pi$ and cancel under the echo. Although $|c|^2 = (1 + \sin\theta \cos\phi)/2$

does carry an $n = 0$ mode, it enters only through \mathcal{A}_{ϕ} , where the lune line-integral structure $[f(\phi_0) - f(\phi_0 + \delta\phi)]$ annihilates the ϕ -independent component before the echo acts. The leading surviving mode $n = \pm 2$ first appears at $O(\sigma^3)$ from cubic products $|c|^2c$, giving $\delta\gamma_{\text{geo}} = O(\sigma^3/\Omega_m^3)$. \square

Supplemental Theorem G1 follows by combining this sector hierarchy with the assumed erasure detection of $|0\rangle$ population and the usual conditional/no-erasure decomposition of the gate channel. The underlying mechanism (destructive interference between the $|B_+\rangle$ and $|B_-\rangle$ perturbative channels, which we call the *parity filter*) follows directly from the symmetric $\pm\Omega_m/2$ bright-state splitting of the Λ Hamiltonian. Corollary 1 of the main text follows immediately: under comparable system-operator sector strengths, the A_2 -sector error ($O(\sigma^2)$) dominates the echo-suppressed E -sector error ($O(\sigma^3)$), so the Pauli-bias ratio $\eta \equiv p_Z/p_{XY}$ grows as (Ω_m/σ) . Together with $|0\rangle$ erasure detection, the resulting conditional biased-erasure channel is exploitable by XZZX-type surface codes [72], which achieve qualitatively higher thresholds than Calderbank-Shor-Steane (CSS) codes under biased noise [73, 74]. The code-capacity quantum error correction (QEC) advantage estimate for the high-strain benchmark error budget is reported in Sec. O.

3. Dual interpretation of the A_2 parity filter

The proof of Proposition 1(b) establishes that $|D^{(1)}\rangle \propto |0\rangle \perp \mathcal{Q}$ for A_2 -sector perturbations. Here we spell out the two consequences of this single equation.

Under a quasi-static perturbation $V = \sigma S_z$ (A_2 irrep), the first-order dark-state correction is

$$|D^{(1)}\rangle = \frac{\sigma}{\sqrt{2}} \left[\frac{\langle B_+|S_z|D\rangle}{-\Omega_m/2} |B_+\rangle + \frac{\langle B_-|S_z|D\rangle}{+\Omega_m/2} |B_-\rangle \right]. \quad (\text{G4})$$

The matrix elements $\langle B_{\pm}|S_z|D\rangle$ have the same sign (since $\langle 0|S_z|D\rangle = 0$ for spin-1), so

$$|D^{(1)}\rangle = \frac{\sigma\langle B|S_z|D\rangle}{\sqrt{2} \cdot \Omega_m/2} [-|B_+\rangle + |B_-\rangle]. \quad (\text{G5})$$

Substituting $|B_{\pm}\rangle = (|B\rangle \pm |0\rangle)/\sqrt{2}$:

$$-|B_+\rangle + |B_-\rangle = -\frac{|B\rangle + |0\rangle}{\sqrt{2}} + \frac{|B\rangle - |0\rangle}{\sqrt{2}} = -\sqrt{2}|0\rangle. \quad (\text{G6})$$

Therefore

$$|D^{(1)}\rangle = -\frac{\sigma\langle B|S_z|D\rangle}{\Omega_m/2} |0\rangle. \quad (\text{G7})$$

Fact 1 (Berry-connection invariance). Because $|D^{(1)}\rangle \propto |0\rangle$ and $\partial_{\mu}|D\rangle \in \mathcal{Q}$ for all control parameters μ , and $\langle 0|\partial_{\mu}D\rangle = 0$, the first-order Berry-connection correction vanishes:

$$\delta\mathcal{A}_{\mu}^{(1)} = i\langle D^{(1)}|\partial_{\mu}D\rangle + i\langle D|\partial_{\mu}D^{(1)}\rangle = 0. \quad (\text{G8})$$

This is Proposition 1(b): the geometric phase is protected at $O(\sigma)$, with the leading correction appearing at $O(\sigma^2/\Omega_m^2)$.

Face 2 (Leakage direction). The same equation shows that the perturbed dark state $|D\rangle + |D^{(1)}\rangle$ acquires a component in $|0\rangle$ with probability $p_{\text{leak}} \propto \sigma^2 |\langle B|S_z|D\rangle|^2 / (\Omega_m/2)^2$. This population lies outside the computational subspace \mathcal{Q} and points toward the optically distinguishable auxiliary level, providing a microscopic explanation for why A_2 -type noise preferentially produces leakage directed at $|0\rangle$ rather than at $|B\rangle$.

Inseparability. The two faces are mathematically inseparable. The parity filter causes destructive interference in the $|B\rangle$ direction (the $|B\rangle$ components of $|B_+\rangle$ and $|B_-\rangle$ cancel), which is *simultaneously* the reason the Berry connection is invariant (Face 1) and the reason the leakage points toward $|0\rangle$ (Face 2).

E -sector contrast. For E -sector perturbations ($V = \sigma S_x$), the matrix elements $\langle B_\pm|S_x|D\rangle$ have *opposite* sign (since $\langle B|S_x|D\rangle = 0$ but $\langle 0|S_x|D\rangle \neq 0$ for spin-1), giving

$$+|B_+\rangle + |B_-\rangle = +\sqrt{2}|B\rangle. \quad (\text{G9})$$

The first-order correction is $|D^{(1)}\rangle \propto |B\rangle \in \mathcal{Q}$: it remains in the computational subspace as an in-subspace error, not leakage to $|0\rangle$. Suppression in this sector relies on the π -echo between the two NGQC lunes, not on the parity filter's leakage direction.

4. Sector-injection diagnostic

The ideal proof above classifies possible system-operator sectors; it does not assume that the fabricated surface-spin environment itself respects the NV point group. To connect the proof to the actual Regime-A noise model and to verify the parity filter directly, we ran a sector-injection diagnostic on the ideal three-level Λ Hamiltonian

$$H_0/\Omega_m = \frac{1}{2}(|0\rangle\langle B| + |B\rangle\langle 0|). \quad (\text{G10})$$

Equal-Hilbert–Schmidt-norm sector representatives

$$\{S_z^2, S_z, S_x, S_y\}$$

were injected with strength σ , and the first-order dark-state correction was projected onto the auxiliary direction $|0\rangle$ and the logical bright direction $|B\rangle$:

$$f_{|0\rangle} = \frac{W_0}{W_0 + W_B}, \quad f_{|B\rangle} = \frac{W_B}{W_0 + W_B}. \quad (\text{G11})$$

The resulting sector directions and scaling laws are summarized in Fig. S1.

The first-order directions are:

Sector	Operator	$f_{ 0\rangle}$	$f_{ B\rangle}$
A_1	S_z^2	0	0
A_2	S_z	1.000000	0.000000
E_x	S_x	0.000000	1.000000
E_y	S_y	0.000000	1.000000

The A_1 row has zero first-order coupling because S_z^2 is the identity on \mathcal{Q} ; its fractions are therefore reported as zero rather than interpreted as a direction.

The nonzero response weights have log-log slopes

$$A_2 \rightarrow |0\rangle : 2.000, \quad E_x, E_y \rightarrow |B\rangle : 2.000.$$

This confirms perturbative scaling: the first-order correction is an amplitude, while the plotted response is a probability/weight. For the open-lune geometric phase, the E -sector slopes are

$$E_x : 0.986 \rightarrow 2.986, \quad E_y : 0.968 \rightarrow 2.984,$$

where the arrow denotes adding the π -shifted second lune. Thus the two-lune echo removes the leading E -sector geometric term.

The same calculation can be written as an irrep-to-channel response matrix. For a weak sector representative V_Γ , define

$$\mathcal{R}_{\Gamma \rightarrow c} = \lim_{\sigma \rightarrow 0} \frac{p_c[V_\Gamma]}{(\sigma/\Omega_m)^2}, \quad (\text{G12})$$

where c denotes a measured port. Table S2 reports the finite- $\sigma/\Omega_m = 10^{-3}$ estimate of this response in the same equal-Hilbert–Schmidt-norm convention. The two decisive entries are $\mathcal{R}_{A_2 \rightarrow P_0} = 2$ and $\mathcal{R}_{E \rightarrow W_B} = 2$, with crossed population responses at the numerical floor.

Therefore, the clean Λ manifold acts as a crystalline irrep polarimeter. In the syndrome-port response, A_2 routes its first-order population weight to the auxiliary port, whereas the transverse E sector routes it to the logical bright port. Separately, S_z is also a static longitudinal splitting of the logical doublet, so the polarimetry result should not be read as the absence of all Z -like calibration shifts.

A useful continuous check is obtained by injecting

$$V(\alpha, \beta) = \sigma[\cos \alpha S_z + \sin \alpha(\cos \beta S_x + \sin \beta S_y)]. \quad (\text{G13})$$

The measured routing fractions obey

$$f_0(\alpha) = \cos^2 \alpha, \quad f_B(\alpha) = \sin^2 \alpha,$$

independent of the transverse angle β . Numerically, the maximum absolute deviations from the two laws are 6.661×10^{-15} , and the maximum β -standard deviations are 7.474×10^{-16} for f_0 and 7.549×10^{-16} for f_B . Figure S2 summarizes the response matrix and the continuous interpolation.

The same diagnostic also projects the operator multiplying the stochastic surface field used in the Regime-A simulation. For

$$H_{\text{surf}}(t)/h = \gamma_e B_z^{\text{surf}}(t) S_z,$$

the Hilbert–Schmidt sector weights are

$$(w_{A_1}, w_{A_2}, w_{E_x}, w_{E_y}) = (0, 1, 0, 0),$$

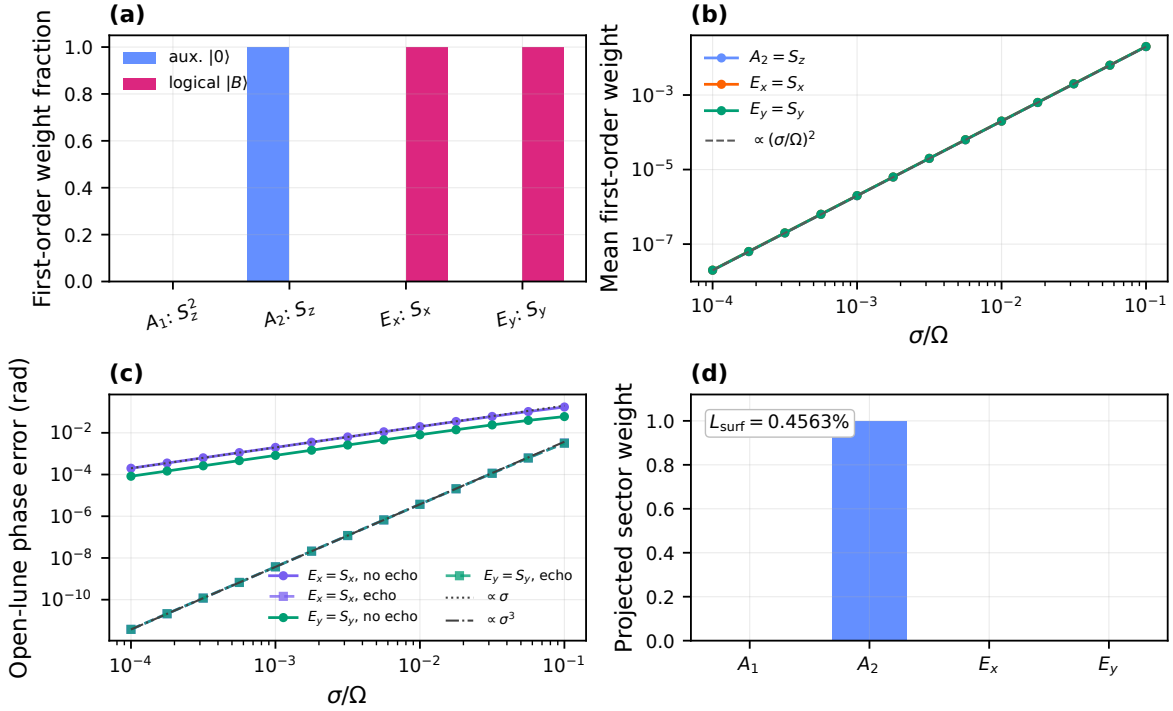


FIG. S1. Sector-injection verification of the Λ -manifold symmetry-to-channel map. (a) First-order response direction: $A_2 = S_z$ points entirely toward $|0\rangle$, while $E = S_x, S_y$ points entirely toward $|B\rangle$. (b) Nonzero response weights scale quadratically in σ/Ω_m , as expected for probabilities from first-order amplitudes. (c) The E -sector geometric phase is approximately linear without echo and approximately cubic with the π -shifted two-lune echo. (d) The actual Regime-A surface-noise operator projects as $(w_{A_1}, w_{A_2}, w_{E_x}, w_{E_y}) = (0, 1, 0, 0)$ and gives $L_{\text{surf}} = 0.4563\%$ in the surface-only diagnostic.

TABLE S2. Irrep-to-channel response matrix of the ideal Λ manifold. Probability-like columns are normalized by $(\sigma/\Omega_m)^2$ at $\sigma/\Omega_m = 10^{-3}$. The A_2 row also carries a static longitudinal calibration component, shown separately as “static Z/σ ”; the polarimetry statement concerns population-port routing between P_0 and W_B .

Sector	R_{P_0}	R_{W_B}	R_{XY}	$R_Z^{(1)}$	$R_Z^{(\text{echo})}$	common/ σ	static Z/σ
$A_1 : S_z^2$	9.447×10^{-33}	0	0	0	0	1.000000	0
$A_2 : S_z$	2.000000	0	0	0	0	0	1.000000
$E_x : S_x$	0	2.000000	2.000000	0.997774	3.546×10^{-12}	0	0
$E_y : S_y$	0	2.000000	2.000000	0.170654	3.550×10^{-12}	0	0

to numerical precision. Propagating 96 ME-CCE/KMC traces through the Regime-A SATD control with only this surface-noise term present gives

$$L_{\text{surf}} = 0.4563\%.$$

This provides a direct numerical bridge between the actual surface noise used in the simulation and the A_2 parity-filter mechanism: the operator sector is fixed by the modeled coupling $B_z^{\text{surf}}(t)S_z$, while the absolute erasure probability is fixed by the Regime-A device simulation.

5. Effective-spurion robustness diagnostic

We also ran a compact robustness diagnostic that perturbs the ideal $A_2 \rightarrow |0\rangle$ map at the effective Λ -

Hamiltonian level. This is not a full actuator-transfer-function simulation. It asks whether the parity-filter fractions degrade continuously under detuning, arm-amplitude, and arm-phase spurions.

For a dressed-state detuning Δ/Ω_m , the analytic leakage of the first-order direction into $|B\rangle$ is

$$f_{|B}^{(\Delta)} = \frac{4(\Delta/\Omega_m)^2}{1 + 4(\Delta/\Omega_m)^2}. \quad (\text{G14})$$

For fractional arm-amplitude skew a and phase skew $\delta\phi$, the small-error scalings are

$$f_{|B}^{(a)} \approx a^2, \quad f_{|B}^{(\delta\phi)} \approx \sin^2 \delta\phi. \quad (\text{G15})$$

The numerical robustness scan is shown in Fig. S3.

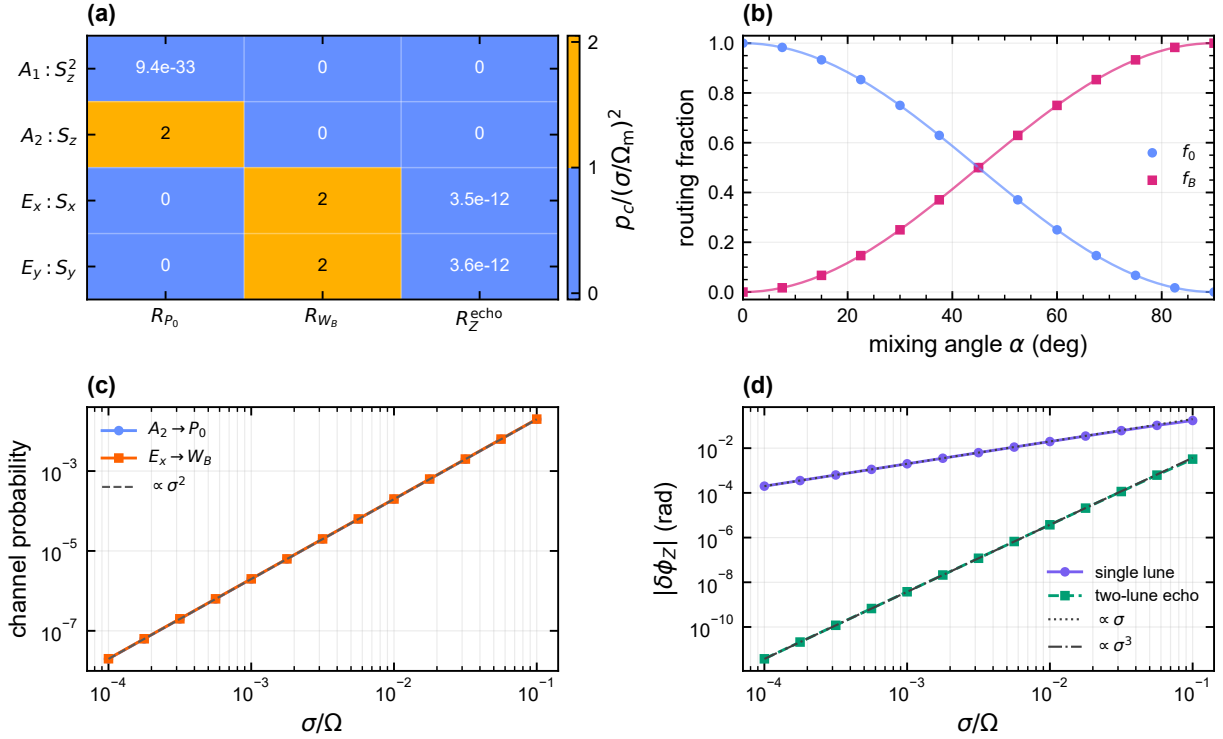


FIG. S2. Irrep-to-syndrome polarimetry of the ideal Λ manifold. (a) Response matrix $\mathcal{R}_{\Gamma \rightarrow c}$ for equal-norm representatives S_z^2 , S_z , S_x , and S_y . The A_2 row is routed to the auxiliary port P_0 , while the transverse E rows are routed to the logical bright port W_B . (b) Mixed A_2 - E perturbations obey $f_0 = \cos^2 \alpha$ and $f_B = \sin^2 \alpha$, independent of the transverse angle β . (c) The nonzero population-response ports scale as $(\sigma/\Omega_m)^2$. (d) For an E -sector perturbation, the single-lune geometric phase is approximately first order in σ/Ω_m , while the two-lune echo leaves an approximately cubic residual.

Imperfection	$f_{ 0\rangle}$	$f_{ B\rangle}$
$\Delta/\Omega_m = 0.10$	0.961538	0.038462
$a = 10\%$	0.989968	0.010032
$\delta\phi = 10^\circ$	0.970413	0.029587
combined worst point	0.905407	0.094593

The combined point uses $\Delta/\Omega_m = 0.10$, $a = 10\%$, and $\delta\phi = 10^\circ$. Even under simultaneous moderate imperfections in this compact model, the nominal A_2 perturbation remains dominantly auxiliary-directed. The correct conclusion is graceful degradation of the sector map, not a hardware-tolerance claim for a specific transducer.

6. What symmetry does not determine

The numerical probabilities p_{era} , p_Z , p_{dep} , and p_{XY} are not fixed by representation theory. They depend on T_1 , $T_{1\rho}$, surface-spin spectral density, control imperfections, mechanical mode splitting, quadrature calibration, and erasure-detection efficiency. In particular, the ME-CCE/KMC bath in the Regime-A simulation is not assumed to be a point-group-symmetric environment: it enters as the explicit A_2 perturbation $B_z^{\text{surf}}(t)S_z$. The dominance of detected leakage in the extracted channel is consistent with the A_2 parity filter, but the absolute

erasure probability is set by the simulated bath realization and device parameters. A bath with parametrically enhanced E -sector system-operator strength, a detector with $\eta_{\text{det}} \approx 0$, or a device whose mechanical doublet is not tuned within the RWA bandwidth would not yield the same biased-erasure channel even though the operator classification remains valid. Thus symmetry protects the local circular selection rule and fixes the perturbative hierarchy of allowed system operators; the simulated device model fixes the rates.

Appendix H: Regime-B resonant HBAR transfer-function map

Regime B translates the Regime-A rotating-frame control Hamiltonian into a resonant GHz-HBAR setting. The shared Λ Hamiltonian is unchanged; the resonator implementation sets the attainable Ω_m , linewidth, drive bandwidth, and envelope-tracking strategy. The membrane mode-topology benchmark of Sec. IV C of the main text and Appendices A and B operates at $f_0 = 78.8$ MHz, far below the NV zero-field splitting $D \approx 2.87$ GHz required for resonant driving. Here we present a concrete GHz resonator design and quantify the achievable Rabi frequency. The high-strain $\Omega_m = 2.22$ MHz result in the

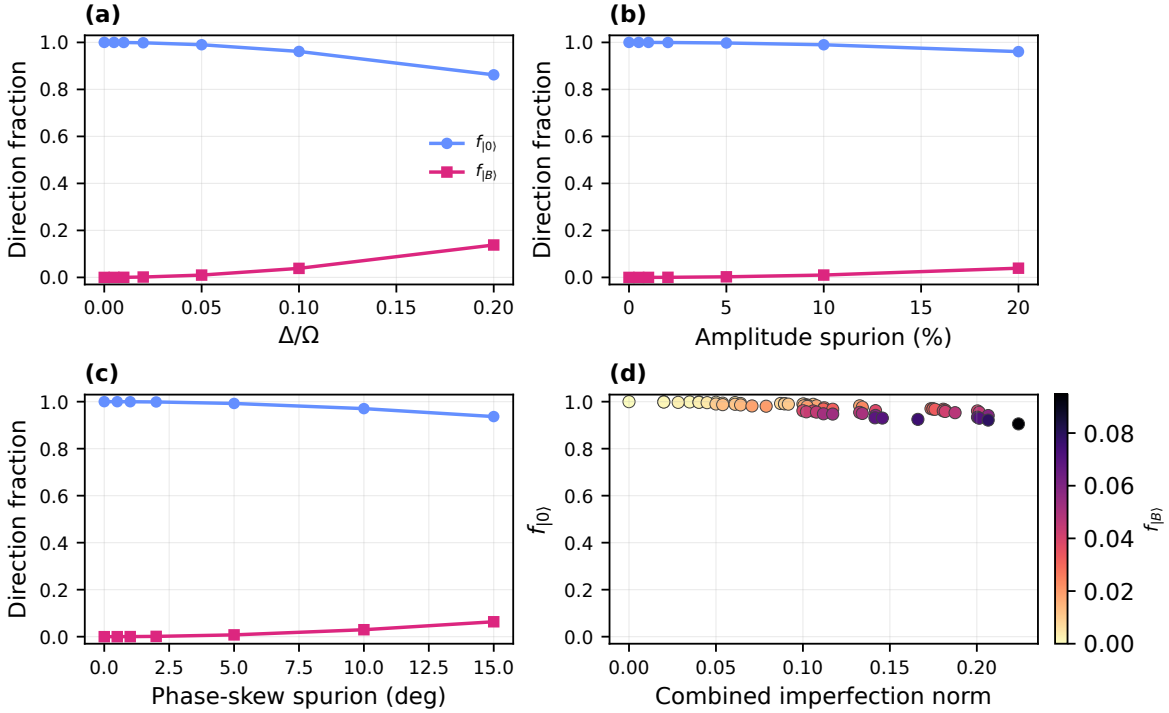


FIG. S3. Effective-spurion robustness of the $A_2 \rightarrow |0\rangle$ parity filter. (a) Auxiliary and logical-bright direction fractions $f_{|0\rangle}$ and $f_{|B\rangle}$ versus detuning Δ/Ω . (b) Direction fractions under quadrature amplitude imbalance, shown as an amplitude-spurion percentage. (c) Direction fractions under quadrature phase skew. (d) Combined-spurion scan showing $f_{|0\rangle}$ versus the combined imperfection norm, with point color indicating $f_{|B\rangle}$. Across these scans the A_2 response degrades continuously into the logical-bright direction rather than showing a sharp failure of the sector map.

main text establishes the rotating-frame channel benchmark; the HBAR-realistic prediction is reported separately below using the smaller Rabi frequencies accessible in the GHz design.

a. Consistent Regime-B HBAR design. The Regime-B implementation used for Sweep 9 is a (100) diamond disk with $h_d = 23.4 \mu\text{m}$, $R = 25 \mu\text{m}$, and a $1 \mu\text{m}$ AlN transducer. This thickness gives an HBAR free spectral range matching the NV Zeeman splitting at $B_z \simeq 49 \text{ G}$, so adjacent thickness-shear overtones address the two Λ legs. The overtone frequencies are

$$f_n = \frac{n v_T}{2 h_d}, \quad v_T = 12822 \text{ m s}^{-1}, \quad (\text{H1})$$

so $n = 10$ and $n = 11$ lie near $D_- \approx 2.733 \text{ GHz}$ and $D_+ \approx 3.007 \text{ GHz}$. Residual detunings can be trimmed by RIE thickness control, uniaxial stress, or radius tuning near an avoided crossing [18]. AlN/single-crystal-diamond HBAR stacks have been demonstrated as high-overtone bulk acoustic resonators [65].

b. Degenerate mode pair for quadrature shear. For [100] propagation in cubic diamond, the two transverse shear branches are degenerate by four-fold symmetry, with $v_T = \sqrt{C_{44}/\rho} = 12822 \text{ m s}^{-1}$ using $C_{44} = 578 \text{ GPa}$ [64] and $\rho = 3515 \text{ kg m}^{-3}$. They generate the orthogonal shear components ε_{xz} and ε_{yz} . Electrode loading and fabrication asymmetry can split the doublet, but the residual splitting is assumed to be tuned below the

envelope bandwidth by the DC spring-softening method of Appendix C.

The n -th shear overtone has $\varepsilon_{xz}(z) = \varepsilon_0 \cos(n\pi z/h_d)$. For $n = 10$, the surface is an antinode and a shallow $d_{\text{NV}} \sim 20 \text{ nm}$ NV samples $\cos(n\pi d_{\text{NV}}/h_d) > 0.9999$, so the strain is effectively uniform over the implanted layer. Ensemble operation should place NVs within an acoustic-antinode window.

Two orthogonal AlN electrodes, or one electrode pair with a 90° rotated pattern, drive the shear polarizations in quadrature and reproduce the circular strain field of Eq. (1) of the main text.

c. Dual-overtone tuning for Λ -system control. The Λ -system gate couples both $|0\rangle \leftrightarrow |+1\rangle$ (at D_+) and $|0\rangle \leftrightarrow |-1\rangle$ (at D_-) simultaneously (Sec. IIC of the main text). Because one GHz overtone has only $\Delta f_{3\text{dB}} \sim 300 \text{ kHz}$, the two arms are driven by adjacent overtones whose free spectral range equals the Zeeman splitting:

$$\frac{v_T}{2h_d} = 2\gamma_e B_z. \quad (\text{H2})$$

The Regime-B values above give $\text{FSR} \approx 274 \text{ MHz}$, placing $n = 10$ and $n = 11$ at D_- and D_+ . Each overtone carries its own shear doublet, providing independent σ_- and σ_+ circular drives.

d. Achievable strain amplitude. The AlN layer produces a direct piezoelectric strain $\varepsilon_{\text{direct}} \simeq d_{33} V_{\text{RF}}/h_{\text{AlN}}$,

where $d_{33} = 5.5 \text{ pm V}^{-1}$ (AlN) and $h_{\text{AlN}} = 1 \mu\text{m}$. The local shear strain relevant for NV driving is not obtained from this longitudinal AlN strain with unit efficiency. We therefore write the target shear amplitude as

$$\varepsilon_0 \simeq \eta_{\text{sh}} Q_L \frac{d_{33} V_{\text{RF}}}{h_{\text{AlN}}}. \quad (\text{H3})$$

Here Q_L is the loaded acoustic quality factor and η_{sh} is the effective AlN-to-diamond target shear-strain transduction factor, incorporating AlN/diamond acoustic loading, longitudinal-to-shear conversion, electrode participation, finite mode overlap, and local strain participation at the NV. The unit-efficiency expression ($\eta_{\text{sh}} = 1$) is an upper bound. The voltage values in Table S3 use $Q_L = 10^4$ and $\eta_{\text{sh}} = 10^{-3}$, equivalently $\eta_{\text{sh}} Q_L \simeq 10$. This gives $V_{\text{RF}} \simeq 0.018 \text{ V}, 0.18 \text{ V}, 0.91 \text{ V}$ for $\varepsilon_0 = 10^{-6}, 10^{-5}, 5 \times 10^{-5}$, respectively. Diamond HBAR resonators routinely achieve $Q \gtrsim 10^4$ at GHz frequencies: MacQuarrie *et al.* demonstrated mechanically driven NV spin transitions with a diamond resonator at $Q > 10^4$ [14, 15], and Chen *et al.* achieved $Q \approx 1.2 \times 10^4$ in a semiconfocal diamond acoustic resonator at $\sim 3 \text{ GHz}$ [18], with single-quantum NV spin driving confirmed at $Q = 10^4$ in a subsequent experiment [16]. These demonstrations establish $Q \geq 10^4$ as an experimentally validated baseline for GHz diamond nanomechanics.

e. Cryogenic quality-factor prospects. Demonstrated GHz diamond devices already reach $Q \simeq 10^4$ [16]; higher- Q cryogenic phononic platforms reach 10^6 – 10^{10} in related materials and geometries [66–68]. Reaching $Q \geq 10^5$ in AlN-on-diamond would likely require improved transducer growth, hybrid phononic confinement, or a separate optomechanical phonon bus.

Table S3 summarizes the single HBAR implementation assumed in Regime B, together with the conservative, moderate, and optimistic strain scenarios used in Sweep 9.

The optimistic scenario ($\varepsilon_0 = 5 \times 10^{-5}$, $V_{\text{RF}} \simeq 0.91 \text{ V}$) is conditional on achieving $\eta_{\text{sh}} Q_L \simeq 10$, or $\eta_{\text{sh}} \simeq 10^{-3}$ for $Q_L = 10^4$. It remains well within diamond’s elastic limit ($\varepsilon_{\text{yield}} \sim 1\%$) and compatible with cryogenic operation.

f. Heating and power dissipation. At $f = 2.87 \text{ GHz}$, the RF drive power is $P = V_{\text{RF}}^2 / (2R_{\text{mot}})$, where the motional resistance $R_{\text{mot}} \sim 50 \Omega$ for a well-matched HBAR (typical for AlN-on-diamond composite resonators [69]). For $V_{\text{RF}} = 0.91 \text{ V}$: $P \simeq 0.91^2 / 100 \simeq 8.3 \text{ mW}$. With diamond’s room-temperature bulk thermal conductivity $\kappa = 2200 \text{ W m}^{-1} \text{ K}^{-1}$, a one-dimensional steady-state estimate gives $\Delta T \approx Ph_d / (\kappa \pi R^2) \ll 1 \text{ K}$. This upper bound neglects lateral heat spreading (which further reduces ΔT) and thermal boundary resistance (which could locally increase it); a finite-element thermal analysis is warranted for the cryogenic operating regime, where the cooling power budget is tighter.

g. Acoustic bandwidth constraint. The resonator is continuously driven at resonance throughout the gate, so free ring-down does not occur. The operative constraint

is the acoustic modulation bandwidth: the resonator must track the amplitude envelope of the control protocol, whose modulation bandwidth is $\Delta f_{\text{env}} \approx 2/T_{\text{gate}}$. Requiring the resonator’s 3 dB bandwidth f_0/Q to exceed Δf_{env} yields

$$Q < \frac{f_0 T_{\text{gate}}}{2}. \quad (\text{H4})$$

For $T_{\text{gate}} \geq 7 \mu\text{s}$, $Q = 10^4$ satisfies this constraint directly. At shorter gate times, one may reduce Q and compensate with modestly higher V_{RF} , or apply RF pre-distortion (inverse filtering of the resonator transfer function), a standard technique in resonator-coupled superconducting-qubit control. The pre-ring time to reach steady-state strain is $t_{\text{pre}} \approx 3Q/(\pi f_0) \approx 3.3 \mu\text{s}$ for $Q = 10^4$.

h. Gate-time landscape at reduced Ω_{m} . The SATD counter-diabatic protocol removes the adiabatic-speed constraint ($\lambda = 1$ cancels leakage exactly), so the gate time is no longer limited by the adiabatic ratio η . The dominant fidelity limit shifts to $T_{1\rho}$ decoherence: $F_{\text{limit}} \approx e^{-T_{\text{gate}}/T_{1\rho}}$. For $T_{1\rho} = 500 \mu\text{s}$, a gate time $T_{\text{gate}} = 10 \mu\text{s}$ yields $F_{\text{limit}} \approx 0.980$, while $T_{\text{gate}} = 5 \mu\text{s}$ yields $F_{\text{limit}} \approx 0.990$. The optimal gate time balances the rising decoherence cost against the diminishing SATD fidelity gain at longer durations.

Sweep 9 maps this trade-off numerically for all three HBAR scenarios. At $T_{\text{gate}} = 2 \mu\text{s}$, the projected HBAR cases give $F_{\text{avg}} = 99.50$ – 99.85% ; the optimistic design reaches $F_{\text{avg}} = 99.05\%$ at the first Rabi-refocusing magic time ($T_{\text{gate}} \approx 14 \mu\text{s}$). These Sweep 9 values assume the same ideal rotating-frame control Hamiltonian used in the benchmark simulations, including the resonant DQ SATD tone. HBAR-specific phase noise, heating, and transducer filtering are bounded separately rather than included as Lindblad channels; the Floquet validation in Appendix N, Sec. 6, shows that a bare $Q = 10^4$ HBAR transfer function is narrower than the $1.833 \mu\text{s}$ Regime-A benchmark envelope. The resonant route therefore requires predistortion, reduced effective Q , or a slower HBAR-specific pulse, converting the benchmark into a concrete resonator-design target. The biased-erasure estimates in the main text therefore remain tied to the extracted Regime-A channel. In the HBAR route, residual envelope filtering, phase skew, and quadrature imbalance are promoted to the transverse-floor sensitivity parameters used in Appendix O, Sec. 6, rather than folded into a new headline erasure-overhead number. As a control-optimality check, a GRAPE (gradient ascent pulse engineering) optimization of the piecewise-constant drive amplitudes at the optimistic Rabi frequency ($\Omega_{\text{m}} = 141.5 \text{ kHz}$, $T_{\text{gate}} = 2 \mu\text{s}$) achieves a noiseless process fidelity of 99.9997% , confirming that the analytical SATD pulse shape is near-optimal and that the $\sim 0.4\%$ infidelity in Sweep 9 is entirely decoherence-limited.

i. Noise-channel transferability. The three simulation noise channels (T_1 , $T_{1\rho}$, ME-CCE surface noise) can be evaluated at any specified Ω_{m} and do not de-

TABLE S3. Compact Regime-B GHz-HBAR implementation table. The Λ -leg coupling is $\Omega_m = |h_{26}|\varepsilon_0$ with $|h_{26}| = 2830$ MHz/strain.

Item	Value	Purpose	Comment
Geometry	$h_d = 23.4 \mu\text{m}$, $R = 25 \mu\text{m}$, $h_{\text{AIN}} = 1 \mu\text{m}$	Sets HBAR spectrum	(100) diamond disk
Dual overtones	$n = 10, 11$; $f_{10} \simeq D_-$, $f_{11} \simeq D_+$	Λ legs	$B_z \simeq 49$ G, FSR $\simeq 274$ MHz
Mode pair	Two shear polarizations/overtone	Circular strain	Residual splitting tuned out
Bandwidth	$f/Q_L \simeq 0.27$ MHz for $Q_L = 10^4$	Envelope tracking	Predistortion or lower Q_L if needed
Strain cases	$10^{-6}, 10^{-5}, 5 \times 10^{-5}$	$\Omega_m = 2.83, 28.3, 141.5$ kHz	$V_{\text{RF}} \simeq 0.02, 0.18, 0.91$ V
DQ-SATD	$f_{\text{DQ}} \simeq 274$ MHz	CD tone	Separate phase-locked DQ strain drive

pend directly on the acoustic carrier frequency f_0 in the rotating-frame Hamiltonian. Implementation-dependent channels (resonator amplitude noise, drive-induced heating, transducer bandwidth) are not integrated into the master equation but are bounded by the engineering estimates above. As a stress test, enhancing the effective surface-noise coupling by $5\times$ adds only $\sim 0.08\%$ to the total error budget (surface noise contributes $\sim 0.02\%$ at the high-strain benchmark), bringing F_{avg} from 99.88% to $\sim 99.80\%$, still well within the high-fidelity regime.

Appendix I: Complete parameter table

Table S4 collects all physical and design parameters used throughout this work.

TABLE S4. Complete parameter table.

Parameter	Symbol	Value	Units	Source
Zero-field splitting	D	2.87	GHz	Ref. [36]
Gyromagnetic ratio	γ_e	2.80	MHz/G	CODATA
Static magnetic field	B_z	50	G	Design
Shear coupling	h_{26}	-2830	MHz/strain	Ref. [36]
In-plane coupling	h_{25}	-2600	MHz/strain	Ref. [36]
Transverse DQ coupling	h_{16}	19660	MHz/strain	Ref. [36]
Young's modulus	$Y_{[100]}$	1050	GPa	Ref. [64]
Poisson's ratio	$\nu_{[100]}$	0.104	—	Ref. [64]
Diamond density	ρ	3515	kg/m ³	Ref. [64]
Membrane side	L	10	μm	Design
Membrane thickness	h_m	200	nm	Design
SS spring constant	k_{SS}	4310	N/m	Computed
Clamped spring constant	$k_{\text{mech}}^{\text{clamp}}$	9530	N/m	Computed
Fundamental frequency	f_0	78.8	MHz	Computed
Vacuum gap	d	200	nm	Design
Breakdown voltage	V_{bd}	35	V	Empirical
Max. displacement	x_0	5	nm	Linear limit
Benchmark Rabi frequency	Ω_m	2.22	MHz	$0.444 \times x_0$
T_1 relaxation	—	1.0	ms	Ref. [47]
$T_{1\rho}$ relaxation	—	0.5	ms	Enriched
NV depth	d_{NV}	20	nm	Design
Surface density	ρ_s	0.004	nm ⁻²	Ref. [48]
Corr. length (tested)	r_c	5	nm	Ref. [47]
Hopping time (tested)	τ_c	10^{-8} - 2×10^{-5}	s	—
MC trajectories	—	500	per point	Convergence
NGQC θ_{max}	—	π	rad	Full N \rightarrow S \rightarrow N
SATD strength	λ	1.0	—	Exact
Optimal gate time	T_{gate}	1.833	μs	Sweep 7

Appendix J: Derivation of the DQ AC Stark Hamiltonian

This appendix derives the effective double-quantum (DQ) AC Stark Hamiltonian stated in Theorem 2 of the main text from first principles. The calculation closely follows the dispersive (light-shift) formalism of Refs. [38–40], adapted to the spin-1 NV Hamiltonian and two-drive gate architecture.

1. DQ operator structure

In the $\{|+1\rangle, |0\rangle, |-1\rangle\}$ eigenbasis of S_z the DQ operators take the matrix form

$$S_x^2 - S_y^2 = \begin{pmatrix} 0 & 0 & 1 \\ 0 & 0 & 0 \\ 1 & 0 & 0 \end{pmatrix}, \quad \{S_x, S_y\} = \begin{pmatrix} 0 & 0 & -i \\ 0 & 0 & 0 \\ i & 0 & 0 \end{pmatrix}, \quad (\text{J1})$$

so that the raising/lowering combinations are

$$(S_x^2 - S_y^2) \pm i\{S_x, S_y\} = 2|\mp 1\rangle\langle \pm 1|. \quad (\text{J2})$$

Crucially, both operators have *identically zero* matrix elements involving $|0\rangle$. Consequently, any second-order energy shift generated by the DQ channel shifts $|\pm 1\rangle$ only relative to each other, never relative to $|0\rangle$.

2. DQ coupling from a circularly polarized strain drive

The DQ part of the Udvarhelyi spin-strain Hamiltonian [36] is

$$\frac{H_{\varepsilon 2}}{h} = \frac{h_{16}}{2} [\varepsilon_{xz} (S_y^2 - S_x^2) + \varepsilon_{yz} \{S_x, S_y\}]. \quad (\text{J3})$$

For a σ_+ circularly polarized shear drive at frequency ω , $\varepsilon_{xz} = \varepsilon_0 \cos \omega t$ and $\varepsilon_{yz} = \varepsilon_0 \sin \omega t$. Inserting Eq. (J1) and defining $\Omega_{\text{DQ}} \equiv h_{16} \varepsilon_0$ gives

$$H_{\text{DQ}}^{(\sigma_+)} = -\frac{h \Omega_{\text{DQ}}}{2} [e^{i\omega t} | +1\rangle\langle -1| + e^{-i\omega t} | -1\rangle\langle +1|]. \quad (\text{J4})$$

For the opposite helicity (σ_- ; same ε_{xz} but $\varepsilon_{yz} \rightarrow -\varepsilon_{yz}$) the exponential signs swap:

$$H_{\text{DQ}}^{(\sigma_-)} = -\frac{h \Omega_{\text{DQ}}}{2} [e^{-i\omega t} | +1\rangle\langle -1| + e^{+i\omega t} | -1\rangle\langle +1|]. \quad (\text{J5})$$

This sign asymmetry between helicities is the physical origin of the S_z (rather than S_z^2) structure of the effective Hamiltonian.

3. Two-drive architecture and rotating frame

The gate protocol uses two strain drives:

$$\text{Drive 1: } \omega_+ = 2\pi(D + \gamma_e B_z), \quad g_+ = \frac{\Omega_{\text{DQ}}}{2} \cos(\theta/2), \quad (\text{J6})$$

$$\text{Drive 2: } \omega_- = 2\pi(D - \gamma_e B_z), \quad g_- = \frac{\Omega_{\text{DQ}}}{2} \sin(\theta/2), \quad (\text{J7})$$

where $\theta(t)$ is the polar angle of the Bloch-sphere trajectory. The simulation operates in the doubly-rotating frame defined by

$$|+1\rangle \rightarrow e^{-i\omega_+ t} |+1\rangle, \quad |-1\rangle \rightarrow e^{-i\omega_- t} |-1\rangle, \quad |0\rangle \rightarrow |0\rangle. \quad (\text{J8})$$

Under this transformation the DQ coupling from Drive 1 (σ_+ at ω_+) oscillates at the residual detuning

$$\Omega_- \equiv \omega_+ - (\omega_+ - \omega_-) = \omega_- = 2\pi(D - \gamma_e B_z), \quad (\text{J9})$$

while the coupling from Drive 2 (σ_- at ω_-) oscillates at

$$\Omega_+ \equiv \omega_- + (\omega_+ - \omega_-) = \omega_+ = 2\pi(D + \gamma_e B_z). \quad (\text{J10})$$

Both detunings are of order $D \sim 2.87$ GHz, three orders of magnitude larger than the couplings $g_{\pm} \sim$ MHz.

4. Second-order energy shifts

For a monochromatic off-resonant perturbation $V(t) = Ae^{i\omega t} + A^\dagger e^{-i\omega t}$ acting on states that are degenerate in the rotating frame, the standard AC Stark (light-shift) formula [38, 40] gives the second-order energy shift of state $|n\rangle$:

$$\delta E_n^{(2)} = \sum_{m \neq n} \left[\frac{|\langle m|A|n\rangle|^2}{\hbar\omega} + \frac{|\langle m|A^\dagger|n\rangle|^2}{-\hbar\omega} \right]. \quad (\text{J11})$$

This is the dispersive limit of the driven two-level system [39]: the two terms correspond to virtual absorption and emission with energy denominators $+\hbar\omega$ and $-\hbar\omega$, respectively.

a. Drive 1 ($A^{(1)} = -g_+ |+1\rangle\langle -1|$, oscillating at Ω_-):

$$\delta E_{-1}^{(1)} = +\frac{g_+^2}{\hbar\Omega_-} > 0, \quad (\text{J12})$$

$$\delta E_{+1}^{(1)} = -\frac{g_+^2}{\hbar\Omega_-} < 0, \quad (\text{J13})$$

$$\delta E_0^{(1)} = 0. \quad (\text{J14})$$

b. Drive 2 ($A^{(2)} = -g_- |-1\rangle\langle +1|$, oscillating at Ω_+):

$$\delta E_{+1}^{(2)} = +\frac{g_-^2}{\hbar\Omega_+} > 0, \quad (\text{J15})$$

$$\delta E_{-1}^{(2)} = -\frac{g_-^2}{\hbar\Omega_+} < 0, \quad (\text{J16})$$

$$\delta E_0^{(2)} = 0. \quad (\text{J17})$$

In both cases $\delta E_0 = 0$ because the DQ operators have no matrix elements with $|0\rangle$ [Eq. (J1)].

5. Total effective Hamiltonian

Summing the contributions:

$$\begin{aligned} \delta E_{+1} &= -\frac{g_+^2}{\hbar\Omega_-} + \frac{g_-^2}{\hbar\Omega_+}, \\ \delta E_{-1} &= +\frac{g_+^2}{\hbar\Omega_-} - \frac{g_-^2}{\hbar\Omega_+}, \\ \delta E_0 &= 0. \end{aligned} \quad (\text{J18})$$

The common-mode shift vanishes identically: $(\delta E_{+1} + \delta E_{-1})/2 = 0$. The effective Hamiltonian restricted to \mathcal{Q} is therefore

$$\begin{aligned} H_{\text{eff}}^{DQ} &= \delta E_{+1} |+1\rangle\langle +1| + \delta E_{-1} |-1\rangle\langle -1| \\ &= \left(\frac{g_+^2}{\Omega_+} - \frac{g_-^2}{\Omega_-} \right) S_z. \end{aligned} \quad (\text{J19})$$

Substituting

$$g_+ = \frac{\Omega_{\text{DQ}}}{2} \cos \frac{\theta}{2}, \quad g_- = \frac{\Omega_{\text{DQ}}}{2} \sin \frac{\theta}{2},$$

and combining over the common denominator $D^2 - \gamma_e^2 B_z^2$:

$$H_{\text{eff}}^{DQ} = -\frac{\Omega_{\text{DQ}}^2}{4D} \left(\cos \theta + \frac{\gamma_e B_z}{D} \right) S_z + \mathcal{O} \left(\frac{\gamma_e^2 B_z^2}{D^2} \right), \quad (\text{J20})$$

where we used $\sin^2(\theta/2) - \cos^2(\theta/2) = -\cos \theta$ and expanded to leading order in $\gamma_e B_z/D \approx 0.049$. This reproduces the AC Stark theorem of the main text, specifically the S_z Hamiltonian structure in Eq. (24) and the residual scale in Eq. (25). The S_z (not S_z^2) structure arises because the DQ channel couples only $|+1\rangle \leftrightarrow |-1\rangle$ and cannot produce virtual transitions through $|0\rangle$, yielding an antisymmetric shift analogous to the dispersive qubit-cavity pull [39].

6. C3v Stark-scaling substitution for 3C-SiC

For any C_{3v} spin-1 platform using the same single-quantum Λ -leg mechanism, the strain required to reach the target mechanical Rabi rate is

$$\varepsilon_0 = \frac{\Omega_m}{|h_{26}|}, \quad (\text{J21})$$

and the off-resonant DQ coupling generated by the same strain is

$$\Omega_{\text{DQ}} = |h_{16}| \varepsilon_0 = \left| \frac{h_{16}}{h_{26}} \right| \Omega_m. \quad (\text{J22})$$

Thus

$$\delta_{\text{AC}} = \frac{1}{4D} \left| \frac{h_{16}}{h_{26}} \right|^2 \Omega_m^2. \quad (\text{J23})$$

At the fixed target $\Omega_m = 2.22$ MHz used in the Regime-A benchmark, the substitution gives

Platform	D (GHz)	h_{26}	h_{16}	$ h_{16}/h_{26} $	δ_{AC} (kHz)
NV	2.870	2.830	19.660	6.947	20.718
3C-SiC	1.330	1.800	1.350	0.750	0.521

The reduction factor is

$$\delta_{AC}^{NV}/\delta_{AC}^{3C-SiC} = 39.76.$$

This is the Hamiltonian-level input to the matched-environment 3C-SiC benchmark in Appendix N, Sec. 7.

Appendix K: Step-by-step experimental protocol

The following protocol separates the two NV implementation layers used in the paper. Path A characterizes the membrane mode-pair topology and calibrates the rotating-frame channel benchmark. Path B translates the same Λ -control protocol to a resonant GHz-HBAR implementation, where Rabi rate and envelope tracking are set by the acoustic transfer function. Because the rotating-frame dynamics depend only on Ω_m (Sec. II C of the main text), the calibration and verification steps (4–7) apply identically to both implementation paths described below once their attainable Ω_m and transfer function are specified.

a. Path A: Membrane mode-topology calibration path.

This path implements the mode-pair geometry that tests the holonomic strain topology. Appendix B gives the thin-plate strain-topology guide, but the local Rabi rate is not calibrated by that topology alone; this path must therefore measure the actual Rabi rate and use the Regime-A value as an effective rotating-frame channel target.

1. Membrane fabrication and characterization.

Fabricate a simply-supported diamond membrane ($L \approx 10 \mu\text{m}$, $h_m \approx 200 \text{nm}$) via reactive-ion etching (RIE) and undercut release. Target EBL alignment $\delta < 0.1\%$ to minimize (1,2)/(2,1) frequency splitting. Verify the boundary condition (SS vs. clamped) via mechanical spectroscopy.

2. Mode frequency measurement and electrostatic tuning.

Measure f_{12} and f_{21} using laser interferometry or electrical impedance spectroscopy. Apply DC voltage to the full-area electrode ($V \leq V_{bd} = 35 \text{V}$) to close any residual splitting Δf via differential spring softening (Appendix C).

3. NV localization and depth estimation.

Confocally locate a single NV center near $(L/4, L/4)$ where the shear strain components ε_{xz} , ε_{yz} form a circularly rotating pair. Estimate the NV depth d_{NV} via spin-echo T_2 measurements (shallower NVs exhibit shorter T_2 from surface noise [48]).

4. SATD calibration via Rabi characterization.

Drive a single mode at calibrated amplitude and measure the Rabi frequency Ω_m . Perform a λ -scan of the counter-diabatic drive amplitude (cf.

Sweep 6): measure process fidelity at several λ values bracketing $\lambda = 1$. The SATD resonance should be recoverable to $\pm 1\%$ precision within ~ 10 calibration points (Sec. VIB, Sweep 6, of the main text).

5. **Magic gate-time identification.** With calibrated Ω_m and $\lambda = 1$, sweep the gate time T_{gate} and measure F_{avg} via quantum process tomography (QPT). Identify the first magic time where bright-state dynamical phase refocuses (expected near $T_{\text{gate}} \approx 4/\Omega_m \approx 1.8 \mu\text{s}$ for $\Omega_m = 2.22 \text{MHz}$).
6. **DC Stark compensation.** With both modes driven in quadrature, measure the equatorial-input process fidelity with and without a DC compensation voltage V_{DC} ; adjust until the 0.2% process-level Stark degradation is nulled. The required compensation is deterministic ($V_{\text{DC}} \propto \delta_{AC}$) and need not be recalibrated dynamically.
7. **Process-tomography verification.** At the optimized operating point ($T_{\text{gate}}, \lambda, V_{\text{DC}}$), perform full single-qubit QPT. Extract F_{avg} , F_e , and \bar{L} . Verify that eigenstate fidelity matches process fidelity within the Stark-immunity prediction (Theorem 2 of the main text).

b. *Path B: GHz-HBAR resonant implementation route.* For resonant driving at $f_0 \approx D \approx 2.87 \text{GHz}$, replace steps (1–3) above with:

- 1'. **HBAR disk fabrication.** Pattern the Regime-B diamond micro-disk ($R \approx 25 \mu\text{m}$, $t_d \approx 23.4 \mu\text{m}$) capped with an AlN piezoelectric transducer for electrical actuation of adjacent thickness-shear overtones near D_{\pm} .
- 2'. **Overtone selection and dual-mode splitting.** Identify the $n = 10$ and $n = 11$ shear-overtone doublets, and close residual polarization splitting electrostatically or via slight disk tilt. Confirm that the Rabi frequency lies within $\Omega_m \approx 2.83\text{--}141.5 \text{kHz}$ (Sweep 9, Table S3).
- 3'. **NV-overtone coupling verification.** Drive one overtone and measure Ω_m via spin-echo Rabi oscillations. Steps (4–7) then proceed as above.

Appendix L: AC Stark injection test (Sweep 8)

Sweep 8 tests the S_z structure of the AC Stark shift (Theorem 2 of the main text) by amplifying $\delta_{AC} \rightarrow \alpha_S \delta_{AC}$ with $\alpha_S \in \{0, \dots, 200\}$ while disabling DC compensation (Table S5). Because the injected term acts dynamically during the gate rather than as a static post-gate phase, both legacy and process-level metrics become sensitive to large uncompensated Stark shifts. At the physical scale $\alpha_S = 1$ the legacy metric remains

high (99.78%), but the process fidelity is already phase-sensitive (99.04%). Larger α_S values produce nonmonotonic coherent wrapping and leakage, confirming the need for DC compensation/calibration and ruling out an S_z^2 common-mode mechanism. With dynamic compensation enabled, the full process fidelity is recovered. The dashed 3C-SiC overlay in Fig. S4 is a separate matched-environment rerun with 50 trajectories per point. At the physical scale $\alpha_S = 1$ it gives $F_{\text{avg}} = 99.8846\%$, statistically indistinguishable from the no-Stark point $F_{\text{avg}} = 99.8830\%$, with leakage 0.476%. Even at $\alpha_S = 10$ the 3C-SiC process fidelity remains 99.848%, illustrating the $39.76\times$ reduction of the bare Stark scale derived in Appendix J, Sec. 6.

TABLE S5. NV AC Stark injection test results at $T_{\text{gate}} = 1.833 \mu\text{s}$, composite NGQC + SATD, DC compensation OFF, 200 trajectories. F_{leg} is the single-state dark eigenstate fidelity. The matched 3C-SiC overlay shown in Fig. S4 is from the separate 50-trajectory rerun described in the text.

α_S	$\delta_{\text{AC}}^{\text{eff}}$ (kHz)	F_{leg} (%)	F_{avg} (%)	Leakage
0	0	99.81	99.88	0.48%
1	20.7	99.78	99.04	0.50%
5	103.6	98.37	79.49	0.64%
10	207	94.47	43.11	0.91%
20	414	94.67	66.08	1.06%
50	1036	25.32	51.33	35.25%
100	2072	58.48	41.68	48.35%
200	4144	48.95	35.87	25.76%

The table gives the NV point values; Fig. S4 plots the same Sweep 8 data and overlays the matched-environment 3C-SiC neutral-divacancy rerun so that the separation between the single-state metric, the process metric, leakage, and platform Stark scale is visible. The coherent, nonmonotonic response is the important feature: the Stark term does not behave like a simple monotone penalty, and the process metric is the diagnostic that exposes the residual phase sensitivity.

Appendix M: Device design constraints

1. Boundary conditions and displacement limit

The simply-supported (SS) membrane has an effective spring constant $k_{\text{mech}}^{\text{SS}} = 4310 \text{ N m}^{-1}$ (Sec. A). In the original slope-scale estimate this would permit access to the full $\Omega_m = 2.22 \text{ MHz}$ at $x_0 = 5 \text{ nm}$. Appendix B uses the membrane modes as a strain-topology guide rather than as a calibrated transverse-shear prediction; the value is used in the channel simulations as an effective Rabi-rate target that must be supplied by direct strain/Rabi calibration or by an implementation such as the HBAR route. Clamping the edges increases the stiffness by a factor of 2.21 ($k_{\text{mech}}^{\text{clamp}} \approx 9530 \text{ N m}^{-1}$), reducing Ω_m from 2.22 MHz (SS) to 1.004 MHz (clamped)

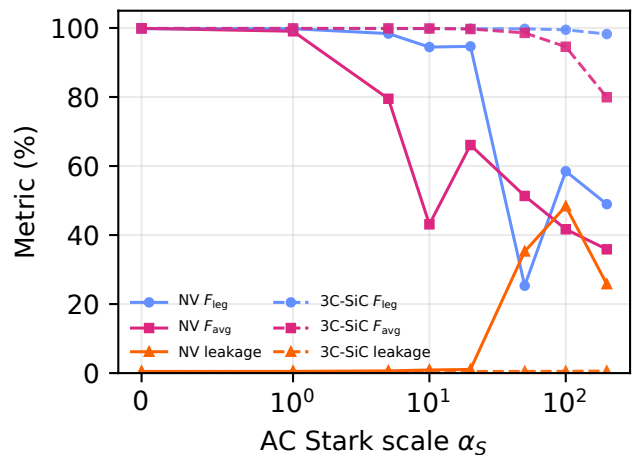


FIG. S4. AC Stark injection response for Sweep 8. Solid curves show the NV channel benchmark and dashed curves show the matched-environment 3C-SiC neutral-divacancy rerun. Amplifying the uncompensated dynamic S_z Stark term separates the single-state metric, process metric, and leakage. At the physical scale $\alpha_S = 1$, the 3C-SiC curve remains essentially on the no-Stark baseline, whereas the NV process metric is phase-sensitive; larger shifts show coherent wrapping and leakage, motivating DC compensation and distinguishing the channel from an S_z^2 common-mode mechanism.

at $x_0 = 5 \text{ nm}$. With DRAG active, the clamped sweep remains high (99.43%–99.47%) but sits below the simply-supported optimum ($\sim 99.49\%$) by about 0.02–0.06 percentage points; simply-supported boundaries remain preferred because higher Ω_m enables greater gate-time compression.

2. Electrostatic degeneracy tuning

Standard electron-beam lithography introduces dimensional asymmetries ($\delta \sim 1\%$) that break the (1,2)/(2,1) modal degeneracy by $\approx 0.47 \text{ MHz}$ (Sec. C). Degeneracy is restored via electrostatic spring-softening: a DC bias $V_{\text{DC}} = 21.6 \text{ V}$ across the $d = 200 \text{ nm}$ vacuum gap selectively softens the stiffer mode [63], with a robust 13.4 V safety margin below the conservative design voltage $V_{\text{bd}} = 35 \text{ V}$ informed by nanoscale vacuum-gap breakdown and MEMS field-emission studies [70, 71]:

$$\omega(V_{\text{DC}}) = \omega_0 \sqrt{1 - \frac{\varepsilon_0 A_{\text{eff}} V_{\text{DC}}^2}{k_{\text{mech}} d^3}}, \quad (\text{M1})$$

where ε_0 here denotes the vacuum permittivity. The full-area electrode is mandatory: a 50%-coverage design requires 30.5 V, impinging on the design-voltage margin.

3. Voltage budget

The voltage budget (Table S6) demonstrates that the system is *displacement-limited*, not voltage-limited.

TABLE S6. Voltage budget for the simply-supported membrane with full-area electrode and $\delta = 1\%$ asymmetry.

Component	Value	
Breakdown limit V_{bd}	35.0	V
DC tuning V_{DC}	21.6	V
Safety margin	3.0	V
AC headroom V_{AC}^{\max}	10.4	V
Required V_{AC} at $\Omega_m = 2.22$ MHz	~ 5	mV

4. NV center requirements

The simulations assume a single NV center at depth $d_{NV} = 20$ nm below the membrane surface, achievable with standard nitrogen ion implantation [41]. Coherence parameters: $T_1 = 1$ ms [42], $T_{1\rho} = 500$ μ s [43] (isotopically purified ^{12}C diamond with enrichment $>99.9\%$ [44, 46]), and $T_2^* \sim 10$ μ s.

Appendix N: Extended parametric studies

This section presents the full parametric sweeps not included in the main text. All simulations use the composite NGQC + SATD protocol with 200 surface-noise trajectories unless otherwise noted.

1. Fidelity vs. mechanical Rabi frequency (Sweep 1)

Sweep 1 evaluates fidelity versus mechanical Rabi frequency $\Omega_m = 0.1$ – 2.5 MHz under worst-case noise ($\tau_c = 10$ ns). With DRAG active, the fidelity is nearly flat: $F = 99.40\%$ – 99.49% , a variation of 0.09% [Fig. S5(a)], confirming that counter-diabatic correction decouples the fidelity from the adiabatic parameter.

2. Frequency detuning tolerance (Sweep 3)

Sweep 3 scans residual frequency detuning $\Delta f = 0$ – 500 kHz [Fig. S5(b)]: fidelity is flat to 0.03% , confirming that the DC tuning mechanism does not require extreme precision.

3. Boundary-condition sensitivity (Sweep 4)

Sweep 4 repeats Sweep 1 under clamped boundary conditions ($k_{\text{mech}}^{\text{clamp}} = 9530$ N m $^{-1}$, $\Omega_m^{\max} = 1.004$ MHz;

Fig. S5(d)): with DRAG active, the clamped sweep remains within 99.43% – 99.47% , about 0.02 – 0.06 percentage points below the simply-supported optimum. Sweep 4.1 confirms that without DRAG, the SS membrane shows oscillatory fidelity ($F = 8\%$ – 99%) while the clamped membrane suffers catastrophic monotonic decay from 96% to 28% ; counter-diabatic correction is therefore a non-negotiable prerequisite for clamped geometries [Fig. S5(e, f)].

4. GHz HBAR extension (Sweep 9)

Sweep 9 extends the gate-time analysis to GHz bulk acoustic resonator Rabi frequencies (Appendix H): conservative ($\Omega_m = 2.83$ kHz), moderate (28.3 kHz), and optimistic (141.5 kHz). SATD eliminates the adiabatic-speed constraint regardless of Ω_m : the process fidelity is $F_{\text{avg}} = 99.50$ – 99.85% across the three scenarios at $T_{\text{gate}} = 2$ μ s (Fig. S6).

5. Quadrature drive robustness (Sweep 10)

Sweep 10 scans amplitude ratio $r \in [0.90, 1.10]$ and phase error $\delta\varphi \in [-10^\circ, +10^\circ]$ at $T_{\text{gate}} = 1.833$ μ s (Fig. S7). The gate maintains $F_{\text{avg}} \geq 99.5\%$ over the central plateau ($|r - 1| \lesssim 4\%$, $|\delta\varphi| \lesssim 4^\circ$). Over the broader $|r - 1| \leq 6\%$, $|\delta\varphi| \leq 6^\circ$ box the minimum sampled value is 99.32% , and the full scan degrades gracefully to 98.0% at the worst corner.

6. Floquet multitone validation (Sweep 12)

To test the rotating-wave and multitone assumptions directly, we added a Floquet-corrected lab-frame validation beyond the ten core parametric sweeps. It is retained in the validation ledger as Sweep 12 rather than counted among Sweeps 1–10. The calculation propagates the Regime-A unitary using the same two Λ -leg envelopes, the resonant DQ SATD envelope, the off-resonant DQ Stark term, and the dynamic DC compensation waveform. The leading counter-rotating Bloch–Siegert/Floquet shifts from the single-quantum tones and the DQ SATD tone are retained. We also apply a first-order transducer bandwidth filter, colored phase noise, and arm-amplitude imbalance. The reference is the nominal rotating-frame unitary, so the values in Table S7 quantify the additional error from effects omitted in the RWA simulation.

The pure counter-rotating correction is therefore small ($1 - F_{\text{avg}} = 2.4 \times 10^{-5}$), and the high-strain benchmark remains within 1.0×10^{-4} of the RWA unitary when the control envelopes are delivered with 200 MHz bandwidth and modest phase/amplitude errors. The bandwidth scan gives $1 - F_{\text{avg}} = 4.2 \times 10^{-5}$, 1.7×10^{-4} , and 8.0×10^{-4} for ideal controls filtered at 200 , 100 ,

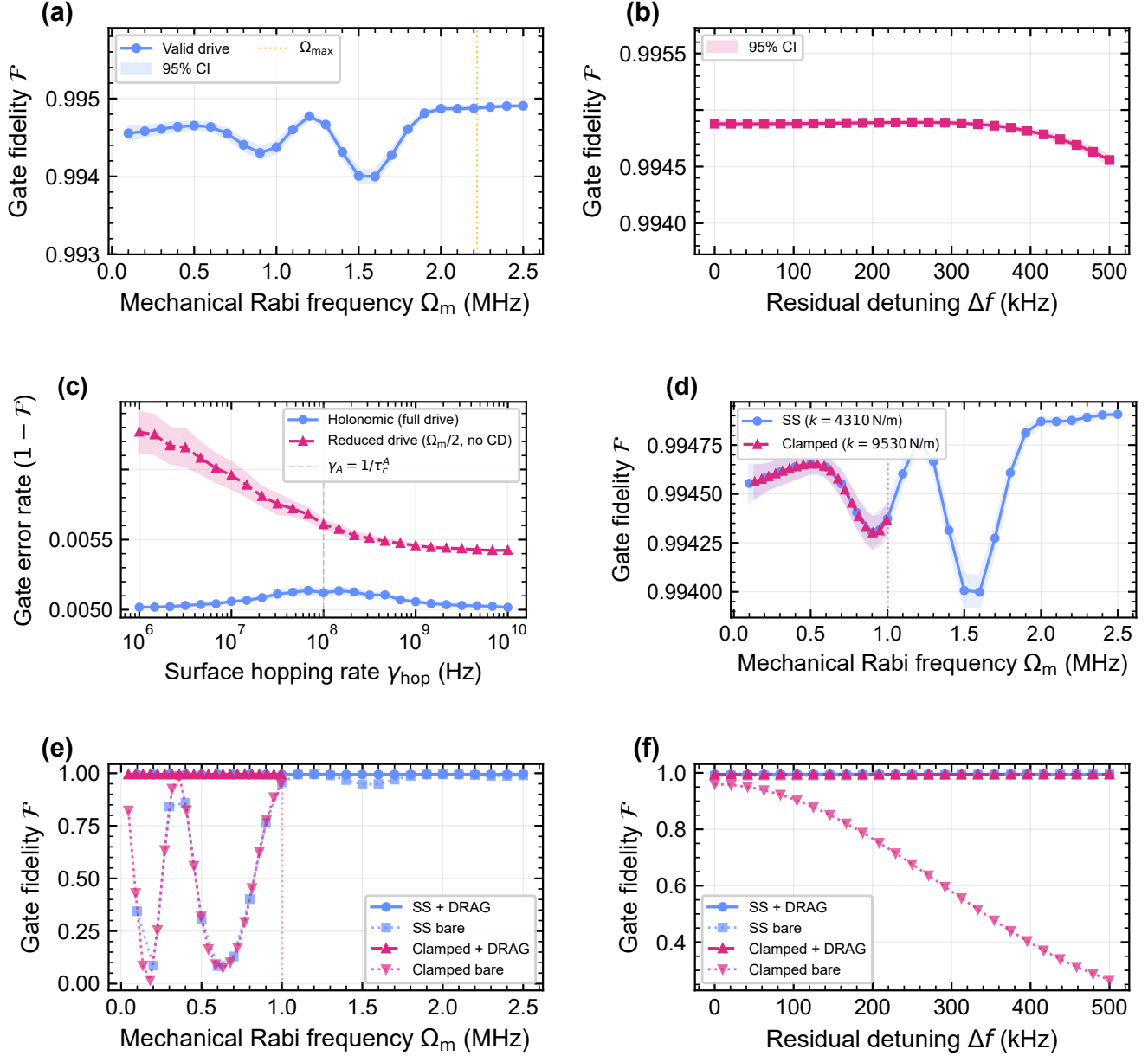


FIG. S5. Hardware and noise tolerance characterization. (a, b) Sweep 1, fidelity vs. Ω_m ; Sweep 3, fidelity vs. detuning Δf . (c) Sweep 2, holonomic (blue) vs. Rabi (pink) gate error vs. surface hopping rate; the holonomic gate forms a noise-immune plateau, $7\times$ more stable and consistently lower. (d) Sweep 4, SS vs. clamped boundary conditions under DRAG. (e, f) Sweep 4.1, DRAG vs. bare adiabatic for headroom and tuning tolerance; without DRAG both membranes show oscillatory or monotonic fidelity collapse.

and 50 MHz, respectively. Conversely, a bare $Q = 10^4$ GHz-HBAR linewidth cannot track the $1.833\ \mu\text{s}$ benchmark envelope without predistortion or a slower waveform. This is why the HBAR Regime-B projection is separated from the high-strain benchmark and why HBAR-specific envelope tracking is treated as an implementation requirement rather than a group-theoretic consequence. For the decoder-facing erasure analysis, this same residual is treated as an explicit contribution to the imposed

p_{XY} floor. Thus the HBAR check tests transferability of the control package; it does not replace the Regime-A open-system channel extraction.

7. Matched-environment 3C-SiC C3v benchmark

The 3C-SiC calculation is a controlled platform-design check, not a measured-device forecast. We keep

TABLE S7. Floquet/lab-frame multitone validation at $T_{\text{gate}} = 1.833 \mu\text{s}$ and $\Omega_m = 2.22 \text{ MHz}$. F_{avg} is computed relative to the nominal rotating-frame unitary on the computational subspace.

Case	F_{avg} vs. RWA	Added leakage
Counter-rotating terms only	0.999976	3.7×10^{-6}
200 MHz BW, 0.2° phase noise, 0.2% imbalance	0.999899	6.0×10^{-5}
50 MHz BW, 1° phase noise, 1% imbalance	0.998247	1.4×10^{-3}
Unpredistorted $Q = 10^4$ HBAR BW (0.287 MHz)	0.414075	4.2×10^{-1}

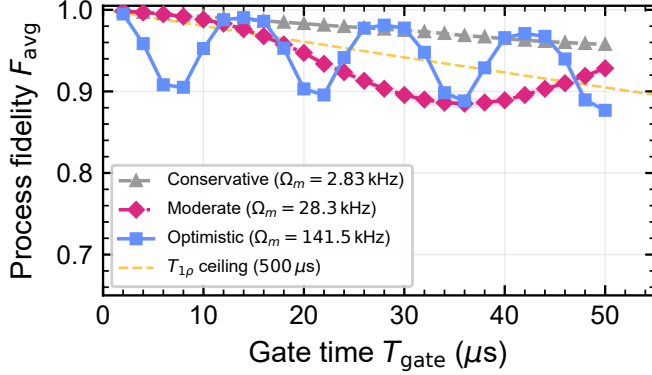


FIG. S6. GHz HBAR gate-time compression (Sweep 9): F_{avg} versus T_{gate} for three achievable strain amplitudes (Table S3); the dashed curve is the $T_{1\rho}$ ceiling. SATD eliminates the adiabatic-speed constraint at all Ω_m .

the Regime-A SATD echo-lune trajectory, surface-bath traces, T_1 , $T_{1\rho}$, erasure bookkeeping, and trajectory seeds fixed at the NV channel-benchmark values, and change only the C_{3v} spin-strain parameters entering the DQ Stark scale. This isolates the effect of smaller $|h_{16}/h_{26}|$. Figure S8 summarizes the matched-environment comparison.

The platform inputs are:

Platform	$ h_{16}/h_{26} $	ϵ_{SQ}	$\epsilon_{\text{DQ-CD}}$	δ_{AC}
NV reference	6.947	7.845×10^{-4}	8.718×10^{-5}	20.718 kHz
3C-SiC assumed	0.750	1.233×10^{-3}	1.270×10^{-3}	0.521 kHz

The full open-system rows use 96 matched stochastic traces and a 1600-step midpoint propagator:

The differential comparison makes the Stark effect explicit:

Comparison	ΔF_{cond}	Δp_Z
NV no-comp – NV comp	-8.258×10^{-3}	+1.2133 pp
3C no-comp – 3C comp	$+2.046 \times 10^{-5}$	-0.0024 pp
3C no-comp – NV no-comp	$+8.278 \times 10^{-3}$	-1.2158 pp

The coherent isolation rows, with surface bath and Lindblad collapse turned off, show the same pattern:

Scenario	F_{cond}	F_{eff}	Leakage
NV Stark	0.99151421	0.98752089	0.4027%
3C-SiC Stark	0.99997888	0.99615165	0.3827%
3C-SiC no Stark	0.99996251	0.99614006	0.3823%

The correct conclusion is a platform-design rule: C_{3v} hosts with small $|h_{16}/h_{26}|$ can preserve the same Λ -

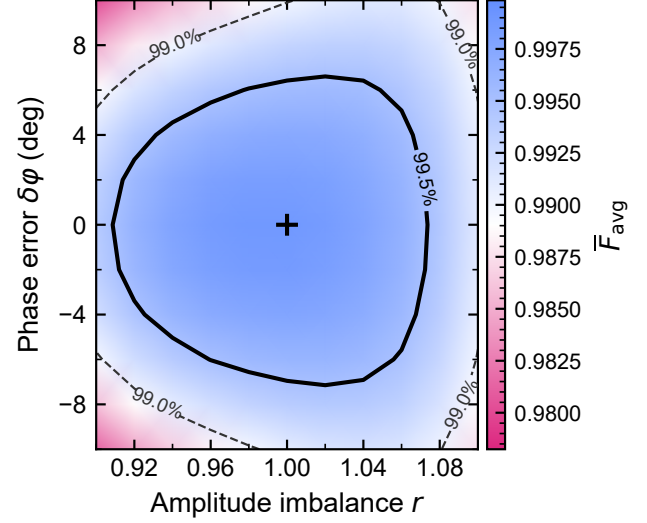


FIG. S7. Quadrature drive robustness (Sweep 10). Process-level average gate fidelity F_{avg} as a function of amplitude imbalance r and phase error $\delta\varphi$, 200 trajectories per point. The solid black contour marks $F_{\text{avg}} = 99.5\%$; dashed and dotted contours indicate 99.0% and 99.9%, respectively. The gate maintains $F_{\text{avg}} \geq 99.5\%$ over the central plateau ($|r-1| \lesssim 4\%$, $|\delta\varphi| \lesssim 4^\circ$); the broader 6° - 6° box has a minimum sampled value of 99.32%.

sector symmetry-to-channel mechanism while suppressing the parasitic DQ Stark channel before active compensation. The calculation does not prove a deployable 3C-SiC architecture; it still requires platform-specific surface noise, relaxation, strain limits, mechanical mode shapes, optomechanical coupling, and auxiliary-state detection. The p_Z and p_{XY} values in Table S8 are conditional Pauli-twirl diagnostics of this compact projected lossy superoperator and should not be substituted for the final Regime-A code-capacity channel rates used in Appendix O.

8. Error reduction summary

Figure S9 compares the baseline DRAG protocol with the composite NGQC + SATD protocol across the full gate-time range. The high-strain benchmark composite protocol achieves $F_{\text{avg}} = 99.88\%$ at $T_{\text{gate}} = 1.833 \mu\text{s}$, a substantial error reduction over the baseline ceiling, confirming that the three mechanisms (singularity neu-

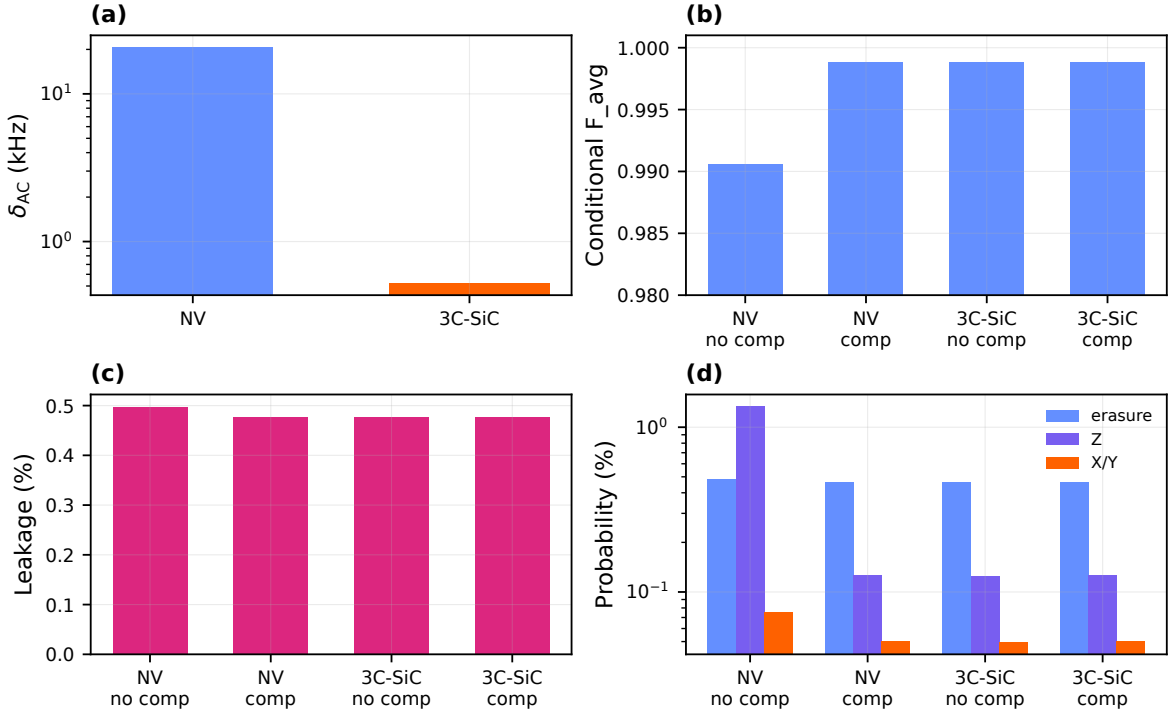


FIG. S8. Matched-environment 3C-SiC C_{3v} comparison. (a) At fixed $\Omega_m = 2.22$ MHz, the assumed 3C-SiC divacancy parameters reduce the parasitic DQ Stark scale by $39.76\times$. (b–d) Using matched surface-bath traces and relaxation settings, uncompensated 3C-SiC lies on the compensated baseline, whereas uncompensated NV shows a visible Stark penalty.

TABLE S8. Matched-environment 3C-SiC matched-environment benchmark. F_{cond} is conditioned on global survival; F_{eff} counts leakage as loss.

Scenario	F_{cond}	F_{eff}	Leakage	p_{era}	p_Z	p_{XY}
NV no comp	0.990568	0.985641	0.4974%	0.4850%	1.3394%	0.0753%
NV comp	0.998826	0.994063	0.4769%	0.4649%	0.1261%	0.0500%
3C-SiC no comp	0.998846	0.994079	0.4773%	0.4654%	0.1237%	0.0493%
3C-SiC comp	0.998826	0.994063	0.4769%	0.4649%	0.1261%	0.0500%

tralization, exact counter-diabatic driving, and gate-time compression) act in concert.

Appendix O: Monte Carlo QEC simulation methods and full data

This section details the Monte Carlo QEC simulations summarized in Sec. VI G of the main text. Each data qubit independently experiences four error channels per round, with physical error rates drawn from the Regime-A channel extraction in Sec. VI F and the error budget in Table VII of the main text. All simulations use 5000 independent trials per data point with minimum-weight perfect matching (MWPM) decoding via PyMatching 2 [79]. The microscopic sector-to-channel origin of the extracted noise model is verified independently in Appendix G by sector-injection diagnostics; this appendix uses the extracted Regime-A channel as input and does not recompute microscopic dynamics.

1. Noise model

The Regime-A/SATD noise model is:

Channel	Probability	Origin
Erasure	$p_{\text{era}} = 0.47\%$	Detected $ 0\rangle$ leakage: noise-mediated CD mismatch + T_1
Z dephasing	$p_Z = 0.168\%$	$T_{1\rho} + A_2$ -sector residual
Depolarizing	$p_{\text{dep}} = 0.012\%$	Undetected leakage
X/Y flip	numerical floor in the nominal extraction	Echo-suppressed E -sector

All rates are uniformly scaled by a common factor $s \in \{1, 2, 5, 10, 20, 50, 75, 100\}$ to probe behavior near and above threshold. Erasure events are injected by replacing the data qubit with a random Pauli (X , Y , or Z with equal probability) and setting the decoder edge weight to zero (effective error probability 0.5), corresponding to the known-location erasure model [78].

Scope and scheduled stress diagnostic.—The code-capacity simulations isolate the response of CSS and

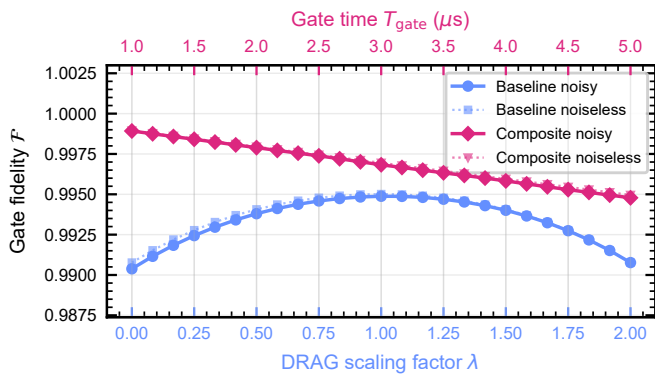


FIG. S9. Error reduction summary. Fidelity comparison of the baseline DRAG protocol (blue) and the composite NGQC + SATD protocol (pink) as a function of DRAG scaling factor λ (bottom axis) and gate time T_{gate} (top axis). The high-strain benchmark composite achieves $F_{\text{avg}} = 99.88\%$ at $T_{\text{gate}} = 1.833 \mu\text{s}$, a substantial error reduction over the baseline ceiling.

XZZX decoders to the extracted Regime-A biased-erasure channel. Because the nominal transverse component is a model-extracted numerical floor rather than a symmetry constant, we also promote finite p_{XY} floors to an explicit decoder stress axis. To test the first circuit layer without introducing a hardware-specific optical/mechanical layout, we run a scheduled two-sector detector-model diagnostic. This diagnostic includes repeated syndrome rounds, erasure-aware weights, measurement/reset faults, explicit transverse X/Y faults, finite erasure-detection efficiency, leakage persistence, delayed flags, and local crosstalk. The nominal code-capacity point gives the $d = 9 / 64\%$ model-channel proxy; finite transverse floors $p_{XY} = 10^{-6}$ – 10^{-4} move the estimate to the $d = 11 / 46.2\%$ envelope; $p_{XY} = 10^{-3}$ moves the code-capacity estimate to $d = 13 / 24.9\%$ and the scheduled detector-model proxy to $d = 11$; combined missed-erasure and finite- p_{XY} stress remains in the $d = 11/d = 13$ envelope; and $2\times$ local crosstalk remains above target even at $d = 15$. Thus the scheduled diagnostic supports the biased-erasure mechanism and identifies crosstalk as the primary hardware-specific target for a future calibrated detector-error model. MWPM is not the optimal decoder for biased noise; bias-tailored decoders (e.g. union-find weighted, tensor-network) would further improve the XZZX advantage, so the numerical distances reported here should be read as model-channel and stress-diagnostic estimates rather than full architecture-level thresholds.

2. Code constructions

a. CSS toric code. Standard $d \times d$ periodic lattice with X -stabilisers on faces and Z -stabilisers on vertices, encoding one logical qubit in $2d^2$ data qubits. Distances

tested: $d \in \{3, 5, 7, 9, 11\}$.

b. XZZX toric code. Same lattice with Hadamard rotations applied to vertical edges, converting each $XXXX$ face stabiliser to $XZZX$ and each $ZZZZ$ vertex stabiliser to $ZXXZ$ [72]. Distances tested: $d \in \{3, 5, 7, 9, 11\}$.

c. XZZX rectangular planar code. Open-boundary rotated planar code with column distance d_c (protecting the dominant Z -error direction) and row distance d_r (protecting the rare X -error direction). Tested configurations: $d_c \in \{7, 9, 11\}$, $d_r \in \{3, 5, 7, 9\}$, at scales $s \in \{1, 10, 50, 100\}$. Face-type-aware Hadamard assignments ensure every column of the check matrix has exactly 2 (boundary) or 4 (bulk) nonzero entries.

Logical error is detected by computing the parity of the recovery operator along a nontrivial homology cycle (toric) or logical representative (planar).

3. Full data: toric codes

Table S10 gives CSS toric code results. p_L increases with d for $s \geq 5$, confirming above-threshold operation.

Table S11 gives XZZX toric code results. p_L decreases monotonically with d at every tested scale including $s = 100$, confirming deeply sub-threshold operation.

The CSS-to-XZZX advantage ratio at $d = 11$ grows from a factor of ~ 200 at $s = 50$ ($p_L^{\text{CSS}}/p_L^{\text{XZZX}} = 0.671/0.0034 = 197$) to 9.0 at $s = 100$. The advantage increases with d at every fixed scale, confirming that the two codes lie on opposite sides of a threshold boundary.

4. Full data: rectangular XZZX planar codes

Table S12 gives rectangular XZZX planar code results. Every asymmetric code ($d_r < d_c$) achieves *zero* logical failures in 5000 trials at all tested scales including $s = 100$. Only the square codes (7×7 and 9×9) exhibit nonzero failures, and only at $s \geq 50$. The Wilson score 95% confidence-level upper bound for a zero-failure result is $p_L < 7.7 \times 10^{-4}$. Thus the rectangular-code data support only a finite-statistics code-capacity bound at the 10^{-4} level; they are not extrapolated to $p_L = 10^{-10}$ and are not used for the headline 64% square-code overhead estimate.

TABLE S9. Compact scheduled two-sector XZZX stress diagnostic for the extracted Regime-A biased-erasure channel. The table summarizes the first circuit-layer validation envelope used in the main text.

Diagnostic	Result	Interpretation
Code-capacity nominal XZZX	$d = 9$, 64% saving	Nominal model-channel estimate
Scheduled nominal, flags	$p_L(d = 9) = 1.00 \times 10^{-3}$	First circuit layer preserves nominal proxy
$p_{XY} = 10^{-3}$	Code-capacity $d = 13$; scheduled proxy $d = 11$	High transverse floor sets stress envelope
$\eta_{\text{det}} = 0.9$ plus finite p_{XY}	$d = 11/d = 13$ regime	Missed erasures reduce margin
$2\times$ crosstalk	$p_L(d = 15) = 2.6 \times 10^{-3}$	Unresolved hardware-specific risk

TABLE S10. CSS toric code logical error rate p_L (failures / 5000 trials) as a function of code distance d and noise scale factor s .

d	$s=1$	$s=2$	$s=5$	$s=10$	$s=20$	$s=50$	$s=75$	$s=100$
3	4.0×10^{-4}	8.0×10^{-4}	4.4×10^{-3}	1.42×10^{-2}	7.38×10^{-2}	0.370	0.617	0.778
5	0	8.0×10^{-4}	6.6×10^{-3}	1.48×10^{-2}	8.52×10^{-2}	0.476	0.699	0.836
7	0	6.0×10^{-4}	6.6×10^{-3}	2.62×10^{-2}	0.116	0.564	0.736	0.840
9	0	1.4×10^{-3}	5.6×10^{-3}	3.24×10^{-2}	0.143	0.624	0.747	0.843
11	6.0×10^{-4}	2.2×10^{-3}	1.06×10^{-2}	4.06×10^{-2}	0.177	0.671	0.739	0.841

TABLE S11. XZZX toric code logical error rate p_L (failures / 5000 trials) as a function of code distance d and noise scale factor s .

d	$s=1$	$s=2$	$s=5$	$s=10$	$s=20$	$s=50$	$s=75$	$s=100$
3	2.0×10^{-4}	0	2.8×10^{-3}	6.8×10^{-3}	2.62×10^{-2}	0.149	0.303	0.471
5	0	0	4.0×10^{-4}	2.0×10^{-4}	3.0×10^{-3}	4.98×10^{-2}	0.146	0.300
7	0	0	0	0	4.0×10^{-4}	2.42×10^{-2}	7.48×10^{-2}	0.194
9	0	0	0	0	0	7.0×10^{-3}	4.40×10^{-2}	0.137
11	0	0	0	0	0	3.4×10^{-3}	2.34×10^{-2}	9.32×10^{-2}

TABLE S12. Rectangular XZZX planar code logical error rate p_L (failures / 5000 trials). All asymmetric configurations ($d_r < d_c$) show zero failures at all scales; only the square codes ($d_r = d_c$, bold) have nonzero failures at high scale.

$d_r \times d_c$	Qubits	$s=1$	$s=10$	$s=50$	$s=100$
3×7	21	0	0	0	0
5×7	35	0	0	0	0
7×7	49	0	0	7.8×10^{-3}	8.84×10^{-2}
3×9	27	0	0	0	0
5×9	45	0	0	0	0
7×9	63	0	0	0	0
9×9	81	0	0	4.6×10^{-3}	6.70×10^{-2}
3×11	33	0	0	0	0
5×11	55	0	0	0	0
7×11	77	0	0	0	0
9×11	99	0	0	0	0

5. Conservative erasure-only baseline

As a conservative comparison, we also analyze the same leakage conversion mechanism without exploiting the strong Z bias of the Regime-A channel. All non-erasure faults are grouped into an isotropic depolarizing residual, so the only structured resource retained by the decoder is known-location erasure. The resulting erasure-only baseline is shown in Fig. S10.

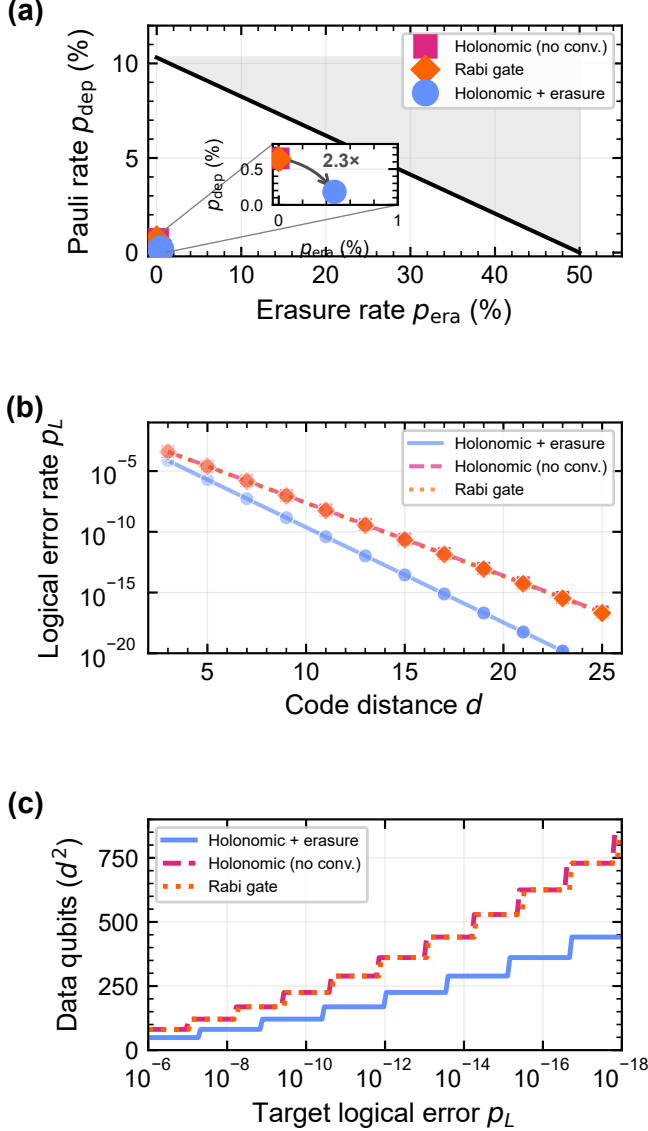


FIG. S10. Conservative erasure-only analysis (isotropic depolarizing non-erasure residual, no Z -bias exploitation). (a) Code-capacity threshold boundary in the $p_{\text{era}}-p_{\text{dep}}$ plane. Blue circle: holonomic gate with erasure conversion ($p_{\text{eff}} = 0.28\%$); pink square: without conversion; orange diamond: Rabi gate. (b) p_L versus code distance d for the conservative erasure-only model of Sec. VIF. (c) Physical qubit overhead versus target p_L . This baseline is superseded by the bias-aware analysis of Sec. VI G and Fig. 6 of the main text.

6. Transverse-floor validation envelope

The square-code overhead quoted in the main text is a nominal code-capacity estimate for the extracted Regime-A channel. Because the nominal p_{XY} component is a model-extracted numerical floor rather than a group-theoretic constant, we propagate explicit X/Y floors and reduced erasure-detection efficiency through the same fit-extrapolated distance model used for Table XI of the main text. This diagnostic is not a circuit-level simulation; it asks how the nominal $d = 9$ XZZX estimate moves when transverse floors or missed-erasure channels are added.

The extrapolation is calibrated to reproduce the two main-text code-capacity anchors: the nominal XZZX square-code point ($d = 9$ at $p_L = 10^{-10}$) and the conservative erasure-only CSS baseline ($d = 11$). A finite p_{XY} floor interpolates the effective scaling from the strongly biased XZZX limit toward the erasure-only baseline, while missed erasures are treated as unheralded residual faults, consistent with surface-code analyses of imperfect erasure checks [76]. Figure S11 shows the resulting required square-code distance and overhead saving relative to the Rabi CSS baseline ($d = 15$).

At the nominal detection efficiency $\eta_{\text{det}} = 97.5\%$, the fit-extrapolated XZZX distance is $d = 9$ for the nominal extracted floor. Adding floors of $p_{XY} = 10^{-6}-10^{-4}$ increases the estimate to $d = 11$, giving a 46.2% saving relative to the $d = 15$ Rabi/CSS baseline, while $p_{XY} = 10^{-3}$ gives $d = 13$ and a 24.9% saving. Reducing η_{det} from 97.5% to 95% similarly moves the nominal-floor point from $d = 9$ to $d = 11$. Thus the XZZX advantage degrades continuously under finite transverse floors; the headline 64% reduction should be read as a code-capacity result for the nominal extracted channel.

7. Perturbative physical-error-to- p_{XY} map

To connect the decoder stress axis to calibration knobs, we construct a compact perturbative transverse-floor map. Each physical imperfection is represented by a normalized small parameter ϵ and converted to an effective transverse probability $p_{XY} = p_{XY}^{\text{nom}} + c\epsilon^2$. This captures the expected “first-order transverse amplitude, second-order probability” scaling and defines calibration targets for the decoder envelope. It is a perturbative map, not a microscopic qutrit/open-system channel extraction.

The map includes residual E -sector strain noise, quadrature amplitude imbalance, quadrature phase error, transverse magnetic-field misalignment, transverse hyperfine components, SATD amplitude and phase errors, and HBAR envelope-filtering residuals. Figure S12 shows the resulting effective p_{XY} values. For example, a 3% quadrature amplitude imbalance, a 3° quadrature phase error, a 1% SATD amplitude error, or a normalized HBAR filtering residual of 10^{-2} reaches the 10^{-4} transverse-floor envelope; stronger residuals approach the

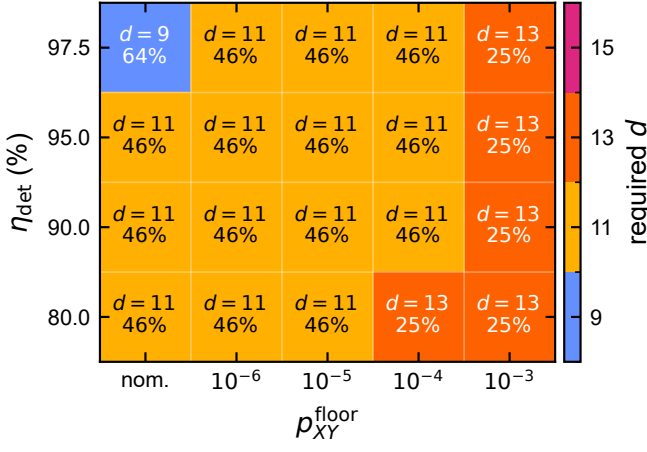


FIG. S11. Transverse-floor validation envelope for the square-code XZZX overhead estimate. Each cell gives the required fit-extrapolated XZZX distance for $p_L = 10^{-10}$ and, underneath, the corresponding data-qubit saving relative to the Rabi CSS baseline with $d = 15$. The axes scan the imposed transverse floor p_{XY}^{floor} and erasure-detection efficiency η_{det} . The plot uses the same code-capacity scaling model as the main-text QEC table and is intended as a model-channel sensitivity test, not a circuit-level threshold calculation.

10^{-3} high-floor stress regime.

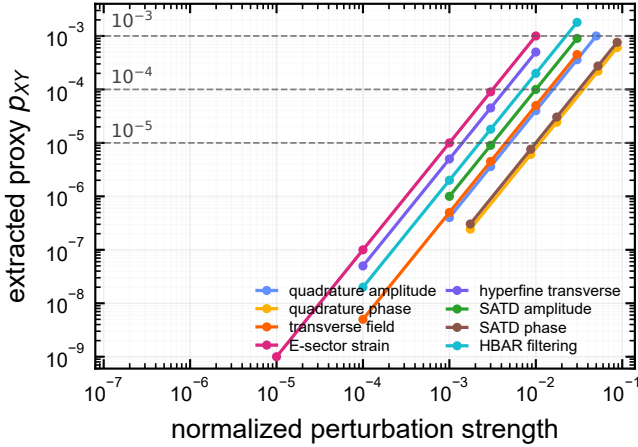


FIG. S12. Perturbative physical-error-to- p_{XY} map. Representative transverse-error mechanisms are converted into an effective decoder stress floor using $p_{XY} = p_{XY}^{\text{nom}} + c\epsilon^2$. Horizontal guide lines mark the 10^{-5} , 10^{-4} , and 10^{-3} transverse-floor envelopes used in the decoder analysis. The plot should be read as a calibration-target map rather than a microscopic channel extraction.

Appendix P: Single-shot bright-state compiler details

This appendix collects the details that are intentionally kept out of the main text. They support the Regime-D

universal-gate validation and are not used in the SATD Regime-A XZZX overhead estimate.

1. Holonomy derivation

Use the cycle-frequency Hamiltonian $K = H/h$ on $\mathcal{H}_\Lambda = \text{span}\{|0_L\rangle, |1_L\rangle, |a\rangle\}$:

$$K(t) = \Delta(t) |a\rangle \langle a| + \frac{1}{2} [\Omega_0(t) |a\rangle \langle 0_L| + \Omega_1(t) |a\rangle \langle 1_L| + \text{h.c.}]. \quad (\text{P1})$$

The proportional-control command is

$$\Omega_0(t) = \Omega(t) \cos \alpha \cos \frac{\vartheta}{2}, \quad (\text{P2})$$

$$\Omega_1(t) = \Omega(t) \cos \alpha e^{-i\phi} \sin \frac{\vartheta}{2}, \quad (\text{P3})$$

$$\Delta(t) = \Omega(t) \sin \alpha. \quad (\text{P4})$$

With

$$|b_{\mathbf{n}}\rangle = \cos \frac{\vartheta}{2} |0_L\rangle + e^{i\phi} \sin \frac{\vartheta}{2} |1_L\rangle, \quad (\text{P5})$$

$$|d_{\mathbf{n}}\rangle = \sin \frac{\vartheta}{2} |0_L\rangle - e^{i\phi} \cos \frac{\vartheta}{2} |1_L\rangle, \quad (\text{P6})$$

the Hamiltonian factorizes as

$$K(t) = \Omega(t) M_{\alpha, \mathbf{n}}, \quad (\text{P7})$$

where

$$M_{\alpha, \mathbf{n}} = \sin \alpha |a\rangle \langle a| + \frac{\cos \alpha}{2} (|a\rangle \langle b_{\mathbf{n}}| + |b_{\mathbf{n}}\rangle \langle a|). \quad (\text{P8})$$

In the ordered basis $(|b_{\mathbf{n}}\rangle, |a\rangle)$,

$$M_\alpha = \begin{pmatrix} 0 & \cos \alpha/2 \\ \cos \alpha/2 & \sin \alpha \end{pmatrix}, \quad \lambda_{\pm} = \frac{\sin \alpha \pm 1}{2}. \quad (\text{P9})$$

The dark state is exactly decoupled and $[K(t), K(t')] = 0$. When

$$\int_0^T \Omega(t) dt = 1, \quad (\text{P10})$$

the bright/auxiliary block evolves as $\exp[-i2\pi M_\alpha] = e^{-i\pi(1+\sin \alpha)} I$. The induced logical gate is therefore

$$U_L(\mathbf{n}, \gamma) = |d_{\mathbf{n}}\rangle \langle d_{\mathbf{n}}| + e^{-i\gamma} |b_{\mathbf{n}}\rangle \langle b_{\mathbf{n}}|, \quad \gamma = \pi(1+\sin \alpha), \quad (\text{P11})$$

or, up to a global phase, $U_L \doteq \exp[-i\gamma \mathbf{n} \cdot \boldsymbol{\sigma}/2]$.

2. Non-Abelian diagnostic

The commutator follows directly from the Pauli representation:

$$[U(\mathbf{n}_1, \gamma_1), U(\mathbf{n}_2, \gamma_2)] = -2i \sin \frac{\gamma_1}{2} \sin \frac{\gamma_2}{2} (\mathbf{n}_1 \times \mathbf{n}_2) \cdot \boldsymbol{\sigma}. \quad (\text{P12})$$

Thus nonparallel nontrivial pulses do not commute. The numerical diagnostic applies $X_{\pi/2}Z_{\pi/2}$ and $Z_{\pi/2}X_{\pi/2}$ to the same test states. Each ordered sequence has unit fidelity to its own target in the ideal compiler, while the two composed unitaries have average gate fidelity 0.5 relative to one another, Frobenius commutator norm $\sqrt{2}$, and operator commutator norm 1.

3. Transfer matrix and detuning channel

The exact theorem requires the physical controls to preserve a fixed direction in command space,

$$\mathbf{u}(t) = (\Omega_0, \Omega_1, \Delta)^T = \Omega(t)\mathbf{u}_0. \quad (\text{P13})$$

We model the acoustic and detuning actuator by a base-band transfer matrix,

$$\mathbf{u}_{\text{act}}(\omega) = G(\omega)\mathbf{u}_{\text{cmd}}(\omega). \quad (\text{P14})$$

Common-envelope filtering is harmless when

$$G(\omega)\mathbf{u}_0 \simeq g(\omega)\mathbf{u}_0 \quad (\text{P15})$$

over the pulse bandwidth. Relative delay, arm imbalance, phase skew, reflections, or detuning-channel mismatch rotate \mathbf{u}_0 and therefore produce gate errors. The compact design criterion used in the Regime-D validation is $BT_{\text{gate}} \gtrsim 10$, where B is the usable calibrated waveform bandwidth. The baseline detuning implementation is IQ-programmed rotating-frame detuning synchronized to the two Λ -leg envelopes; Stark or DC detuning can be substituted only after being included as the third measured waveform channel.

4. Scope relative to the SATD stack

The SATD echo-lune stack and the single-shot compiler answer different questions. SATD uses the composite lune, phase echo, and resonant lower-doublet counterdiabatic actuator to engineer the strongly biased-erasure Regime-A channel. Single-shot uses one cyclic bright-state pulse with two Λ legs plus scalar detuning to generate universal $\text{SU}(2)$ gates. Its residual channel is moderately biased and gate-dependent, so it is not used for architecture-level fault-tolerance claims.

5. SiV single-shot bright-state benchmark (Regime E)

Regime E applies the same bright-state compiler to the SiV orbital Λ manifold. The benchmark uses only the two orbit-strain Λ legs and a synchronized scalar detuning; no lower-doublet SATD actuator is assumed. The orbital T_1 model sends auxiliary-state population equally into the two logical states, producing in-subspace depolarization

rather than erasure-convertible leakage. Orbital dephasing, charge noise, and actuator transfer-function errors are not included. The results should therefore be read as orbital- T_1 -limited universal-control benchmarks, not as a SiV biased-erasure or XZZX channel claim.

Table S13 gives the full sensitivity table generated by `code/siv_single_shot.py`. The primary millikelvin point is the $\Omega_{\text{peak}} = 300$ MHz row used in the main text. The 100 MHz and 500 MHz rows test the expected speed dependence of the orbital- T_1 error, while the 4 K row uses the measured $T_{1,\text{orb}} = 40$ ns temperature-stress value.

Appendix Q: Bright-projector bus validation and phase-cycled biased-erasure closure

This appendix records the Regime-F architecture diagnostic. It tests whether the same symmetry-generated bright-state projector used in the single-qubit compilers can also define an effective phonon-bus entangler whose extracted channel remains phase-biased and compatible with heralded leakage. Regime F is an effective Λ -level validation of the projector-force model, not a microscopic hardware-level two-qubit theorem.

1. Projector-force identity

For two defects coupled to a shared mechanical mode, consider

$$K_I(t) = (f_1 P_{b1} + f_2 P_{b2}) (ae^{-i2\pi\delta t} + a^\dagger e^{i2\pi\delta t}), \quad (\text{Q1})$$

where $K = H/h$ and $P_{bi} = |b_i\rangle\langle b_i|$ is the logical bright-state projector. Since P_{b1} and P_{b2} commute, the Magnus expansion closes exactly. At $T = 1/\delta$ the displacement vanishes and

$$U(T) = \exp \left[i \frac{2\pi}{\delta^2} (f_1 P_{b1} + f_2 P_{b2})^2 \right]. \quad (\text{Q2})$$

After removing single-qubit phases, the nonlocal part is

$$U_{\text{ent}} \sim \exp \left[i \frac{4\pi f_1 f_2}{\delta^2} P_{b1} P_{b2} \right]. \quad (\text{Q3})$$

For $f_1 = f_2 = f$, the CZ-class condition is $f/\delta = 1/2$, giving $T_{\text{CZ}} = 1/(2f)$ in ordinary-frequency units. Choosing $P_b = (I + Z)/2$ gives

$$P_{b1} P_{b2} = \frac{1}{4} (I + Z_1 + Z_2 + Z_1 Z_2), \quad (\text{Q4})$$

so the nonlocal part is locally equivalent to CZ after single-qubit Z corrections.

2. Λ -level CZ extraction

The validation embeds the two logical qubits in a two-qutrit $\{|0\rangle, |1\rangle, |a\rangle\}^{\otimes 2}$ space and couples the logical bright

TABLE S13. Supplemental Regime E SiV single-shot sensitivity table. All rows use the bright-state compiler with two orbit-strain Λ legs plus synchronized scalar detuning and no lower-doublet SATD actuator.

Scenario	Gate	Ω_{peak}	T_{gate}	F_{eff}	F_{cond}	Leakage
mK, primary	Z_{π}	300 MHz	6.667 ns	99.5221%	99.7488%	2.275×10^{-3}
mK, primary	X_{π}	300 MHz	6.667 ns	99.5221%	99.7488%	2.275×10^{-3}
mK, primary	$X_{\pi/2}$	300 MHz	6.667 ns	99.6699%	99.7979%	1.283×10^{-3}
mK, primary	Generic 0.73π	300 MHz	6.667 ns	99.5671%	99.7621%	1.957×10^{-3}
mK, slow	Z_{π}	100 MHz	20.000 ns	98.5894%	99.2362%	6.540×10^{-3}
mK, slow	X_{π}	100 MHz	20.000 ns	98.5894%	99.2362%	6.540×10^{-3}
mK, slow	$X_{\pi/2}$	100 MHz	20.000 ns	99.0231%	99.3906%	3.707×10^{-3}
mK, slow	Generic 0.73π	100 MHz	20.000 ns	98.7214%	99.2788%	5.631×10^{-3}
mK, fast	Z_{π}	500 MHz	4.000 ns	99.7123%	99.8497%	1.377×10^{-3}
mK, fast	X_{π}	500 MHz	4.000 ns	99.7123%	99.8497%	1.377×10^{-3}
mK, fast	$X_{\pi/2}$	500 MHz	4.000 ns	99.8014%	99.8788%	7.757×10^{-4}
mK, fast	Generic 0.73π	500 MHz	4.000 ns	99.7395%	99.8576%	1.184×10^{-3}
4 K stress	Z_{π}	300 MHz	6.667 ns	98.3299%	99.0883%	7.685×10^{-3}
4 K stress	X_{π}	300 MHz	6.667 ns	98.3299%	99.0883%	7.685×10^{-3}
4 K stress	$X_{\pi/2}$	300 MHz	6.667 ns	98.8425%	99.2743%	4.363×10^{-3}
4 K stress	Generic 0.73π	300 MHz	6.667 ns	98.4859%	99.1397%	6.619×10^{-3}

TABLE S14. Regime-F Λ -level CZ-class channel extraction. The Pauli components are the target-frame conditional Pauli-twirl diagnostics after heralded auxiliary leakage is separated.

Quantity	Value	Percent
Conditional F_{avg}	0.9980961930	99.8096%
Mean logical survival	0.9995001250	99.9500%
p_{era}	4.873782×10^{-4}	0.04874%
p_Z	2.377468×10^{-3}	0.23775%
p_{ZZ}	2.290797×10^{-6}	0.000229%
p_{XY}	0	0
Missed leakage	1.249688×10^{-5}	0.00125%
Bus nonvacuum mean	9.458929×10^{-5}	0.00946%

TABLE S15. Regime-F cross-checks. The nearly lossless row checks oscillator truncation; the $Q = 10^6$ row is a bus-damping stress test.

Case	F_{avg}	p_{era}	p_Z	p_{ZZ}	p_{XY}
Lossless	0.99999784	1.89×10^{-16}	3.60×10^{-6}	0	3.47×10^{-17}
$Q = 10^6$	0.98501275	4.87×10^{-4}	1.85×10^{-2}	2.57×10^{-4}	2.78×10^{-17}

projectors to a truncated oscillator. The model includes bus damping, logical dephasing, auxiliary-state relaxation, and detected auxiliary leakage. The main Regime-F point uses $f = 2.0$ MHz, $\delta = 4.0$ MHz, $Q = 10^7$, $T = 0.25$ μ s, $n_{\text{Fock}} = 16$, $T_1 = 1$ ms, $T_{1\rho} = 0.5$ ms, and detection efficiency $\eta_{\text{det}} = 0.975$.

The extracted channel is strongly phase-biased: in the tested projector-force model the measurable non-erasure faults are Z and ZZ , while XY terms vanish within numerical precision. It is, however, not erasure-dominated at this operating point, since $p_Z/p_{\text{era}} = 4.88$.

TABLE S16. E-sector phase-cycle slopes. The E_{Sx} , $N = 4$ row is below the numerical fitting floor over the sampled perturbation range.

Sector	$N = 1$	$N = 2$	$N = 3$	$N = 4$
E_{Sx}	0.995	2.995	4.939	below floor
E_{Sy}	0.988	2.994	5.050	6.986

3. Phase-cycled E-sector diagnostic

The two-lune echo used for the SATD channel cancels the leading E -sector geometric term. Regime F also tests the roots-of-unity generalization

$$\phi_j = \phi_0 + \frac{2\pi j}{N}, \quad j = 0, \dots, N-1. \quad (\text{Q5})$$

Low azimuthal harmonics cancel according to $\sum_j e^{im\phi_j} = 0$ unless m is divisible by N . The numerical open-lune diagnostic gives the log-log slopes in Table S16.

Thus the two-lune result reproduces cubic suppression, while the three- and four-lune cycles suppress at least as strongly as the simple $N+1$ heuristic in this diagnostic. A general analytic law requires an explicit harmonic inventory for the chosen path family.

4. Repeated-syndrome XXXX proxy

Finally, we ran a scheduled repeated-syndrome XXXX proxy using the Regime-A single-qubit channel and the extracted Regime-F two-qubit channel. The proxy includes noisy repeated syndrome rounds, measurement faults, known-location erasure weights, and scheduled correlated ZZ pair faults. It is circuit-level only in this

TABLE S17. Zero-point-strain feasibility estimates for the dispersive projector-force route using the SiV strain susceptibility scale.

Geometry	V_{eff}	ϵ_{zpf}	Ω_{zpf}	F_{max}
HBAR disk	3.14×10^{-15}	9.36×10^{-11}	0.122 MHz	0.006 MHz
Ext. nanobeam	2.50×10^{-19}	1.05×10^{-8}	13.6 MHz	0.682 MHz
Conf. nanobeam	3.00×10^{-20}	3.03×10^{-8}	39.4 MHz	1.97 MHz
Aggr. nanobeam	3.00×10^{-21}	9.58×10^{-8}	125 MHz	6.23 MHz

limited sense; it is not a full Stim gate-by-gate detector-error-model circuit.

At scale one the physical rates used by the proxy are $p_Z^{\text{data}} = 2.908734 \times 10^{-3}$, $p_X^{\text{data}} = 4.0 \times 10^{-5}$, $p_{\text{era}}^{\text{data}} = 4.943689 \times 10^{-3}$, $p_{ZZ}^{\text{pair}} = 2.290797 \times 10^{-6}$, and $p_{\text{meas}} = 5.0 \times 10^{-4}$. With 400 trials per point, the base-scale runs show no logical failures for distances 3, 5, and 7; the Wilson upper bound is 9.5×10^{-3} for each zero-count row. Stress points at scale 30 give $p_L = 0.2725$, 0.2125, and 0.1750 for distances 3, 5, and 7, respectively. At scale 50 the proxy is near the high-noise failure regime ($p_L \simeq 0.5$).

5. Force-budget reminder

A simple off-resonant Λ elimination gives the desired force but also exposes the main feasibility constraint. With

$$\frac{H}{\hbar} = \Delta|a\rangle\langle a| + \left[\frac{\Omega_c}{2} + g_0 a e^{-i\delta t} \right] |a\rangle\langle b| + \text{h.c.}, \quad (\text{Q6})$$

adiabatic elimination of $|a\rangle$ gives

$$\frac{H_{\text{eff}}}{\hbar} = -\frac{|\Omega_c|^2}{4\Delta} P_b - \frac{|g_0|^2}{\Delta} a^\dagger a P_b - \left[\frac{\Omega_c^* g_0}{2\Delta} a e^{-i\delta t} + \text{h.c.} \right] P_b. \quad (\text{Q7})$$

Thus $f = \Omega_c g_0 / (2\Delta)$. In the Rabi-rate convention used in the main text, $g_0 = \Omega_{\text{zpf}} / 2$, so

$$f = \frac{\Omega_c \Omega_{\text{zpf}}}{4\Delta} = \sqrt{p_a} \frac{\Omega_{\text{zpf}}}{2}, \quad p_a \simeq \left(\frac{\Omega_c}{2\Delta} \right)^2. \quad (\text{Q8})$$

Here F_{max} assumes $p_a = 1\%$ and V_{eff} is in m^3 . Thus the fast $F = 10$ MHz effective-model point is an aspirational limit for extremely confined SiV nanophononics, larger tolerated auxiliary admixture, or a different coupling mechanism. HBAR-scale zero-point strain is too weak for this dispersive projector-force route.

6. Scope and future work

Regime F closes the architecture at the effective projector-force level and defines the next validation targets. The immediate future work is to derive the projector force from a microscopic actuator and then validate auxiliary leakage, off-resonant carrier excitation,

actuator-transfer distortion, bus damping, thermal occupation, crosstalk, and regenerated transverse error channels. The scheduled two-sector diagnostic in Sec. O tests the first detector-model layer for the Regime-A biased-erasure channel; a calibrated architecture-level detector-error model with microscopic actuator timing remains the next step before making a device-level threshold claim.

CODE AND REPRODUCIBILITY STATEMENT

The public reproduction package for this work is available at <https://github.com/E-zClap/PhononQ>. The repository contains the curated manuscript source, figure PDFs, Python simulation modules, control-pulse CSV, saved JSON sweep data in `m5/data/`, and compact validation outputs in `code/build/`. These files cover the data products used for the main-text figures, supplemental tables, biased-erasure channel extraction, QEC Monte Carlo diagnostics, sector-injection tests, single-shot checks, SiC comparison, lab-frame multitone validation, and the prospective two-qubit bus model.

The recommended lightweight reproduction path is to regenerate figures from the saved data. From the repository's `code/` directory, the relevant commands are `python replot_figures.py`, `python qec_full_simulation.py -plot-only`, and `python qec_channel_sensitivity.py`. Full simulation re-execution is also supported through commands such as `python main.py -quick`, selected `python main.py -sweep 1 jobs`, and `python qec_full_simulation.py -toric`; these jobs are slower and small Monte Carlo differences may occur across library versions, hardware, or random seeds. The repository file `REPRODUCIBILITY.md` lists the principal replotting and re-execution commands.

- [1] H. P. Bartling, J. Yun, K. N. Schymik, M. van Riggelen, L. A. Enthoven, H. B. van Ommen, M. Babaie, F. Sebastiano, M. Markham, D. J. Twitchen, and T. H. Taminiau, “Universal high-fidelity quantum gates for spin-qubits in diamond,” *Phys. Rev. Applied* **23**, 034052 (2025).
- [2] T. P. Harty, D. T. C. Allcock, C. J. Ballance, L. Guidoni, H. A. Janacek, N. M. Linke, D. N. Stacey, and D. M. Lucas, “High-fidelity preparation, gates, memory, and readout of a trapped-ion quantum bit,” *Phys. Rev. Lett.* **113**, 220501 (2014).
- [3] E. Hyppä, S. Kundu, C. F. Chan, A. Gunyhó, J. Hotari, D. Janzso, K. Juliusson, O. Kiuru, J. Kotilahti, A. Landra, *et al.*, “Unimon qubit,” *Nat. Commun.* **13**, 6895 (2022).
- [4] Z. Li, P. Liu, P. Zhao, Z. Mi, H. Xu, X. Liang, T. Su, W. Sun, G. Xue, J.-N. Zhang, W. Liu, Y. Jin, and H. Yu, “Error per single-qubit gate below 10^{-4} in a superconducting qubit,” *npj Quantum Inf.* **9**, 111 (2023).
- [5] C. L. Degen, F. Reinhard, and P. Cappellaro, “Quantum sensing,” *Rev. Mod. Phys.* **89**, 035002 (2017).
- [6] L. Childress and R. Hanson, “Diamond NV centers for quantum computing and quantum networks,” *MRS Bull.* **38**, 134 (2013).
- [7] M. W. Doherty, N. B. Manson, P. Delaney, F. Jelezko, J. Wrachtrup, and L. C. L. Hollenberg, “The nitrogen-vacancy colour centre in diamond,” *Phys. Rep.* **528**, 1–45 (2013).
- [8] J. M. Hornibrook, J. I. Colless, I. D. Conway Lamb, S. J. Pauka, H. Lu, A. C. Gossard, J. D. Watson, G. C. Gardner, S. Fallahi, M. J. Manfra, and D. J. Reilly, “Cryogenic control architecture for large-scale quantum computing,” *Phys. Rev. Applied* **3**, 024010 (2015).
- [9] S. Krinner, S. Storz, P. Kurpiers, P. Magnard, J. Heinsoo, R. Keller, J. Lütolf, C. Eichler, and A. Wallraff, “Engineering cryogenic setups for 100-qubit scale superconducting circuit systems,” *EPJ Quantum Technol.* **6**, 2 (2019).
- [10] F. Lecocq, F. Quinlan, K. Cicak, J. Aumentado, S. A. Diddams, and J. D. Teufel, “Control and readout of a superconducting qubit using a photonic link,” *Nature* **591**, 575–579 (2021).
- [11] M. Küne *et al.*, “The SpinBus architecture for scaling spin qubits with electron shuttling,” *Nat. Commun.* **15**, 4977 (2024).
- [12] G. Mariani, S. Nomoto, S. Kashiwaya, and S. Nomura, “System for the remote control and imaging of MW fields for spin manipulation in NV centers in diamond,” *Sci. Rep.* **10**, 4813 (2020).
- [13] A. Barfuss, J. Teissier, E. Neu, A. Nünkenkamp, and P. Maletinsky, “Strong mechanical driving of a single electron spin,” *Nat. Phys.* **11**, 820–824 (2015).
- [14] E. R. MacQuarrie, T. A. Gosavi, N. R. Jungwirth, S. A. Bhave, and G. D. Fuchs, “Mechanical spin control of nitrogen-vacancy centers in diamond,” *Phys. Rev. Lett.* **111**, 227602 (2013).
- [15] E. R. MacQuarrie, T. A. Gosavi, A. M. Moehle, N. R. Jungwirth, S. A. Bhave, and G. D. Fuchs, “Coherent control of a nitrogen-vacancy center spin ensemble with a diamond mechanical resonator,” *Optica* **2**, 233–238 (2015).
- [16] H. Y. Chen, S. A. Bhave, and G. D. Fuchs, “Acoustically driving the single-quantum spin transition of diamond nitrogen-vacancy centers,” *Phys. Rev. Applied* **13**, 054068 (2020).
- [17] H. Y. Chen, E. R. MacQuarrie, and G. D. Fuchs, “Orbital state manipulation of a diamond nitrogen-vacancy center using a mechanical resonator,” *Phys. Rev. Lett.* **120**, 167401 (2018).
- [18] H. Y. Chen *et al.*, “Engineering electron–phonon coupling of quantum defects to a semiconfocal acoustic resonator,” *Nano Lett.* **19**, 7021–7027 (2019).
- [19] D. Lee *et al.*, “Tuning strain coupling between diamond oscillators and NV centers via interference of two mechanical modes,” *APL Quantum* **2**, 046107 (2025).
- [20] E. Cornell *et al.*, “All-mechanical coherence protection and fast control of a spin qubit,” arXiv:2508.13356 [quant-ph] (2025).
- [21] M. S. Dresselhaus, G. Dresselhaus, and A. Jorio, *Group Theory: Application to the Physics of Condensed Matter* (Springer, Berlin, 2008).
- [22] F. Wilczek and A. Zee, “Appearance of gauge structure in simple dynamical systems,” *Phys. Rev. Lett.* **52**, 2111–2114 (1984).
- [23] P. Zanardi and M. Rasetti, “Holonomic quantum computation,” *Phys. Lett. A* **264**, 94–99 (1999).
- [24] E. Sjöqvist, D. M. Tong, L. M. Andersson, B. Hessmo, M. Johansson, and K. Singh, “Non-adiabatic holonomic quantum computation,” *New J. Phys.* **14**, 103035 (2012).
- [25] S.-L. Zhu and Z. D. Wang, “Implementation of universal quantum gates based on nonadiabatic geometric phases,” *Phys. Rev. Lett.* **89**, 097902 (2002); Erratum *Phys. Rev. Lett.* **89**, 289901 (2002).
- [26] M. V. Berry, “Transitionless quantum driving,” *J. Phys. A* **42**, 365303 (2009).
- [27] A. Baksic, H. Ribeiro, and A. A. Clerk, “Speeding up adiabatic quantum state transfer by using dressed states,” *Phys. Rev. Lett.* **116**, 230503 (2016).
- [28] B. B. Zhou, A. Baksic, H. Ribeiro, C. G. Yale, F. J. Heremans, P. C. Jerger, A. Auer, G. Burkard, A. A. Clerk, and D. D. Awschalom, “Accelerated quantum control using superadiabatic dynamics in a solid-state lambda system,” *Nat. Phys.* **13**, 330–334 (2017).
- [29] A. L. Falk, P. V. Klimov, B. B. Buckley, V. Ivády, I. A. Abrikosov, G. Calusine, W. F. Koehl, Á. Gali, and D. D. Awschalom, “Electrically and mechanically tunable electron spins in silicon carbide color centers,” *Phys. Rev. Lett.* **112**, 187601 (2014).
- [30] P. Udvarhelyi and Á. Gali, “Ab initio spin-strain coupling parameters of divacancy qubits in silicon carbide,” *Phys. Rev. Applied* **10**, 054010 (2018).
- [31] N. H. Wan, T.-J. Lu, K. C. Chen, M. P. Walsh, M. E. Trusheim, L. De Santis, E. A. Bersin, I. B. Harris, S. L. Mouradian, I. R. Christen, E. S. Bielejec, and D. Englund, “Large-scale integration of artificial atoms in hybrid photonic circuits,” *Nature* **583**, 226–231 (2020).
- [32] C. Bradac, W. Gao, J. Forneris, M. E. Trusheim, and I. Aharonovich, “Quantum nanophotonics with group IV defects in diamond,” *Nat. Commun.* **10**, 5625 (2019).
- [33] G. Thiering and A. Gali, “Ab initio magneto-optical spectrum of group-IV vacancy color centers in diamond,” *Phys. Rev. X* **8**, 021063 (2018).
- [34] M. E. Trusheim, B. Pingault, N. H. Wan, M. Gündo-

- gan, L. De Santis, R. Debroux, D. Gangloff, C. Purser, K. C. Chen, M. Walsh, J. J. Rose, J. N. Becker, B. Lienhard, E. Bersin, I. Paradeisanos, G. Wang, D. Lyzwa, A. R.-P. Montblanch, G. Malladi, H. Bakhrü, A. C. Ferrari, I. A. Walmsley, M. Atatüre, and D. Englund, “Transform-limited photons from a coherent tin-vacancy spin in diamond,” *Phys. Rev. Lett.* **124**, 023602 (2020).
- [35] W. Dong, F. Zhuang, S. E. Economou, and E. Barnes, “Doubly geometric quantum control,” *PRX Quantum* **2**, 030333 (2021).
- [36] P. Udvarhelyi, V. O. Shkolnikov, A. Gali, G. Burkard, and A. Pályi, “Spin-strain interaction in nitrogen-vacancy centers in diamond,” *Phys. Rev. B* **98**, 075201 (2018).
- [37] M. J. Burek, N. P. de Leon, B. J. Shields, B. J. M. Hausmann, Y. Chu, Q. Quan, A. S. Zibrov, H. Park, M. D. Lukin, and M. Lončar, “Free-standing mechanical and photonic nanostructures in single-crystal diamond,” *Nano Lett.* **12**, 6084 (2012).
- [38] C. Cohen-Tannoudji, J. Dupont-Roc, and G. Grynberg, *Atom-Photon Interactions: Basic Processes and Applications* (Wiley-VCH, Weinheim, 1998).
- [39] A. Blais, R.-S. Huang, A. Wallraff, S. M. Girvin, and R. J. Schoelkopf, “Cavity quantum electrodynamics for superconducting electrical circuits: An architecture for quantum computation,” *Phys. Rev. A* **69**, 062320 (2004).
- [40] R. Grimm, M. Weidemüller, and Y. B. Ovchinnikov, “Optical dipole traps for neutral atoms,” *Adv. At. Mol. Opt. Phys.* **42**, 95–170 (2000).
- [41] S. Pezzagna, B. Naydenov, F. Jelezko, J. Wrachtrup, and J. Meijer, “Creation efficiency of nitrogen-vacancy centres in diamond,” *New J. Phys.* **12**, 065017 (2010).
- [42] A. Jarmola, V. M. Acosta, K. Jensen, S. Chemerisov, and D. Budker, “Temperature- and magnetic-field-dependent longitudinal spin relaxation in nitrogen-vacancy ensembles in diamond,” *Phys. Rev. Lett.* **108**, 197601 (2012).
- [43] N. Bar-Gill, L. M. Pham, A. Jarmola, D. Budker, and R. L. Walsworth, “Solid-state electronic spin coherence time approaching one second,” *Nat. Commun.* **4**, 1743 (2013).
- [44] G. Balasubramanian, P. Neumann, D. Twitchen, M. Markham, R. Kolesov, N. Mizuochi, J. Isoya, J. Achard, J. Beck, J. Tissler, *et al.*, “Ultralong spin coherence time in isotopically engineered diamond,” *Nat. Mater.* **8**, 383–387 (2009).
- [45] L. Robledo, L. Childress, H. Bernien, B. Hensen, P. F. A. Alkemade, and R. Hanson, “High-fidelity projective readout of a solid-state spin quantum register,” *Nature* **477**, 574–578 (2011).
- [46] T. Ishikawa, K.-M. C. Fu, C. Santori, V. M. Acosta, R. G. Beusoleil, H. Watanabe, S. Shikata, and K. M. Itoh, “Optical and spin coherence properties of nitrogen-vacancy centers placed in a 100 nm thick isotopically purified diamond layer,” *Nano Lett.* **12**, 2083–2087 (2012).
- [47] J. Nagura, M. Onizhuk, and G. Galli, “Understanding surface-induced decoherence of NV centers in diamond,” *Phys. Rev. Materials* **10**, 024603 (2026); arXiv:2512.10726.
- [48] B. A. Myers, A. Das, M. C. Dartiailh, K. Ohno, D. D. Awschalom, and A. C. Bleszynski Jayich, “Probing surface noise with depth-calibrated spins in diamond,” *Phys. Rev. Lett.* **113**, 027602 (2014).
- [49] M. Onizhuk, Y.-X. Wang, J. Nagura, A. A. Clerk, and G. Galli, “Understanding central spin decoherence due to interacting dissipative spin baths,” *Phys. Rev. Lett.* **132**, 250401 (2024).
- [50] E. Bauch, S. Singh, J. Lee, C. A. Hart, J. M. Schloss, M. J. Turner, J. F. Barry, L. M. Pham, N. Bar-Gill, S. F. Yelin, and R. L. Walsworth, “Decoherence of ensembles of nitrogen-vacancy centers in diamond,” *Phys. Rev. B* **102**, 134210 (2020).
- [51] J. R. Johansson, P. D. Nation, and F. Nori, “QuTiP 2: A Python framework for the dynamics of open quantum systems,” *Comp. Phys. Comm.* **184**, 1234 (2013).
- [52] N. Lambert, E. Giguère, P. Menczel, B. Li, P. Hopf, G. Suárez, M. Gali, J. Lishman, R. Gadhvi, R. Agarwal, A. Galicia, N. Shammah, P. Nation, J. R. Johansson, S. Ahmed, S. Cross, A. Pitchford, and F. Nori, “QuTiP 5: The Quantum Toolbox in Python,” *Phys. Rep.* **1153**, 1–62 (2026).
- [53] M. Horodecki, P. Horodecki, and R. Horodecki, “General teleportation channel, singlet fraction, and quasidistillation,” *Phys. Rev. A* **60**, 1888–1898 (1999).
- [54] M. A. Nielsen, “A simple formula for the average gate fidelity of a quantum dynamical operation,” *Phys. Lett. A* **303**, 249–252 (2002).
- [55] S. Meesala, Y.-I. Sohn, B. Pingault, L. Shao, H. A. Atikian, J. Holzgrafe, M. Gündogan, C. Stavrakas, A. Sipahigil, C. Chia, R. Evans, M. J. Burek, M. Zhang, L. Wu, J. L. Pacheco, J. Abraham, E. Bielejec, M. D. Lukin, M. Atatüre, and M. Lončar, “Strain engineering of the silicon-vacancy center in diamond,” *Phys. Rev. B* **97**, 205444 (2018).
- [56] C. Hepp, T. Müller, V. Waselowski, J. N. Becker, B. Pingault, H. Sternschulte, D. Steinmüller-Nethl, A. Gali, J. R. Maze, M. Atatüre, and C. Becher, “Electronic structure of the silicon vacancy color center in diamond,” *Phys. Rev. Lett.* **112**, 036405 (2014).
- [57] K. D. Jahnke, A. Sipahigil, J. M. Binder, M. W. Doherty, M. Metsch, L. J. Rogers, N. B. Manson, M. D. Lukin, and F. Jelezko, “Electron-phonon processes of the silicon-vacancy centre in diamond,” *New J. Phys.* **17**, 043011 (2015).
- [58] T. M. Stace, S. D. Barrett, and A. C. Doherty, “Thresholds for topological codes in the presence of loss,” *Phys. Rev. Lett.* **102**, 200501 (2009).
- [59] E. Dennis, A. Kitaev, A. Landahl, and J. Preskill, “Topological quantum memory,” *J. Math. Phys.* **43**, 4452–4505 (2002).
- [60] Y. Wu, S. Kolkowitz, S. Puri, and J. D. Thompson, “Erasure conversion for fault-tolerant quantum computing in alkaline earth Rydberg atom arrays,” *Nat. Commun.* **13**, 4657 (2022).
- [61] Y. Sekiguchi, N. Niikura, R. Kuroiwa, H. Kano, and H. Kosaka, “Optical holonomic single quantum gates with a geometric spin under a zero field,” *Nat. Photon.* **11**, 309–314 (2017).
- [62] C. Zu *et al.*, “Experimental realization of universal geometric quantum gates with solid-state spins,” *Nature* **514**, 72–75 (2014).
- [63] A. Barfuss, J. Teissier, E. Neu, A. Nünnenkamp, and P. Maletinsky, “Spin-stress and spin-strain coupling in diamond-based hybrid spin oscillator systems,” *Phys. Rev. B* **99**, 174102 (2019).
- [64] H. J. McSkimin and P. Andreatch, Jr., “Elastic moduli of diamond as a function of pressure and temperature,” *J. Appl. Phys.* **43**, 2944–2948 (1972).

- [65] B. P. Sorokin, G. M. Kvashnin, A. P. Volkov, V. S. Bormashov, V. V. Aksenkov, M. S. Kuznetsov, G. I. Gordeev, and A. V. Telichko, “AlN/single crystalline diamond piezoelectric structure as a high overtone bulk acoustic resonator,” *Appl. Phys. Lett.* **102**, 113507 (2013).
- [66] H. Oh *et al.*, “A spin-embedded diamond optomechanical resonator with mechanical quality factor exceeding one million,” arXiv:2508.05906 (2025).
- [67] V. J. Gokhale *et al.*, “Epitaxial bulk acoustic wave resonators as highly coherent multi-phonon sources for quantum acoustodynamics,” *Nat. Commun.* **11**, 2314 (2020).
- [68] G. S. MacCabe *et al.*, “Nano-acoustic resonator with ultralong phonon lifetime,” *Science* **370**, 840–843 (2020).
- [69] K. M. Lakin, “Thin film resonator technology,” *IEEE Trans. Ultrason. Ferroelectr. Freq. Control* **52**, 707–716 (2005).
- [70] H. Wang, A. M. Loveless, A. Darr, and A. L. Garner, “Transitions between field emission and vacuum breakdown in nanoscale gaps,” *J. Vac. Sci. Technol. B* **40**, 062805 (2022).
- [71] L. Michalas *et al.*, “A study of field emission process in electrostatically actuated MEMS switches,” *Microelectron. Reliab.* **52**, 2267–2271 (2012).
- [72] J. P. Bonilla Ataides, D. K. Tuckett, S. D. Bartlett, S. T. Flammia, and B. J. Brown, “The XZZX surface code,” *Nat. Commun.* **12**, 2172 (2021).
- [73] D. K. Tuckett, S. D. Bartlett, and S. T. Flammia, “Ultra-high error threshold for surface codes with biased noise,” *Phys. Rev. Lett.* **120**, 050505 (2018).
- [74] D. K. Tuckett, A. S. Darmawan, C. T. Chubb, S. Bravyi, S. D. Bartlett, and S. T. Flammia, “Tailoring surface codes for highly biased noise,” *Phys. Rev. X* **9**, 041031 (2019).
- [75] K. Sahay, J. Jin, J. Claes, J. D. Thompson, and S. Puri, “High-threshold codes for neutral-atom qubits with biased erasure errors,” *Phys. Rev. X* **13**, 041013 (2023).
- [76] K. Chang, S. Singh, J. Claes, K. Sahay, J. Teoh, and S. Puri, “Surface Code with Imperfect Erasure Checks,” *PRX Quantum* **6**, 040355 (2025).
- [77] S. Gu *et al.*, “Fault-tolerant quantum architectures based on erasure qubits,” *Phys. Rev. Research* **7**, 013249 (2025).
- [78] T. M. Stace and S. D. Barrett, “Error correction and degeneracy in surface codes suffering loss,” *Phys. Rev. A* **81**, 022317 (2010).
- [79] O. Higgott and C. Gidney, “Sparse Blossom: correcting a million errors per core second with minimum-weight matching,” *Quantum* **9**, 1600 (2025).